Seismic Interpretation, Distribution, and Basin Modelling of Natural Gas Leakage in Block 2 of the Orange Basin, Offshore South Africa

Donna Louise Boyd

Supervisors:

Maarten de Wit (AEON and University of Cape Town)

Zahie Anka (GFZ German Research Centre for Geosciences, Potsdam)

Rolando di Primio (GFZ German Research Centre for Geosciences, Potsdam)

Thesis presented for the degree of Masters of Science in the
Department of Geological Sciences and the Africa Earth Observatory Network
(AEON) Research Group at the University of Cape Town, South Africa

August 2010

A collaborative initiative between:

Declaration

I declare that this thesis is my own original work, submitted to the University of Cape Town, for a Masters of Science degree in Geology, and that I have not submitted it to another university for a degree.

Significant contributions, quotes and extracts from research of others are duly acknowledged through appropriate citations and references.

As far as possible I did not allow anyone to copy this work or to present it as his or her own, and endeavoured to complete this thesis without plagiarism.

....

Donna Boyd **Date**

Abstract

300 2D seismic profiles and 10 wells were analysed from the study area of 18750 km^2 in exploration Block 2 of the Orange Basin located offshore the South African continental margin. The aims of this study are to: (1) characterize different natural gas leakage features present throughout the basin, and (2) understand the relationship of natural gas leakage with structural and stratigraphic elements, and (3) quantify liquid/gas hydrocarbon generation, migration and seepage dynamics through the post-rift history of the basin.

The seismic data reveals 2 mega-sequences: Cretaceous and Cenozoic that are subdivided by major stratigraphic unconformities into 5 and 2 sub-units, respectively. The basin is also divided into 2 structural domains: (1) an extensional domain characterized by basinward dipping listric normal faults rooted at Cenomanian/Turonian level identified between 500 to 1500 m of present-day bathymetry, (2) a compressional domain that accommodates the up-dip extension on the lower slope, and which is characterized by landward dipping thrust faults.

113 observed gas chimneys were identified and classified, into 2 main categories: stratigraphically-controlled (sa-c) and structurally-controlled (s-c). The ratio of s-c versus s-ac chimneys is estimated as 2:5, which suggest a strong stratigraphic control on natural gas leakage. The chimneys either terminate at the seafloor where active leaking gas is manifested by pockmarks, or are sealed within the Miocene (14 Ma) sequence as paleo-pockmarks. The s-c chimneys are located along the normal faults in the extensional domain, and terminate as seafloor mounds up to 1500 m in diameter and with heights from 10-50 m. The sa-c pockmarks are between 100-400 m in diameter, and are linked to stratigraphic onlaps and pinch-outs within the Aptian sequence. Several "giant" chimneys, with diameters of more than 7 km, were also identified. One "giant" chimney displays apparent internal gravitational collapse structures. Bright spots indicative of gas presence within the chimneys were identified, but there is no evidence of acoustic turbidity or seismic pull-downs within these "giant" chimneys. This suggests they are paleo-gas-escape structures with no present-day active gas leakage from them.

2D basin modelling was performed on a 220 km transect created from a composite seismic line across the basin. One syn-rift and three post-rift source-rock sequences were included in the model: Hauterivian, Barremian, lower Aptian and Cenomanian/Turonian units. Palaeo-heat flow was modelled as exponentially decreasing from 100 mW/m^2 at the time of rifting (125 Ma) to present-day values of 60 mW/m^2.

Results from migration modelling show that gas from the lower Aptian and the Barremian source rocks migrates laterally-updip to the proximal parts of the basin and then ends up accumulated below the Cenomanian/Turonian sequence that acts as a regional seal. Across the shelf-break and the upper slope, the chimneys and pockmarks are fed from younger Cenomanian/Turonian source rocks. The migration model also indicates that fluids are about 24 times more likely to flow out of the Orange Basin than to be preserved within it.

Methane gas escaping across the sea floor into the exosphere may contribute to Earth's climate fluctuations. Since a significant volume of escaping gas was cut off when at least half of identified s-c chimneys were sealed within the Miocene sequence, retention of gas along this continental margin may have to be factored into global cooling models.

Acknowledgements

I would like to acknowledge several people before the start of the thesis. This study was done with the *Inkaba yeAfrica* collaboration and has been supported by AEON, University of Cape Town, and GFZ German Research Centre for Geosciences, Potsdam. I thank NRF for funding and PetroSA for providing the data and for permission to publish the results.

I am grateful to Gesa Kuhlmann and Katja Hirsch for leading the way through project and to Markus Lögering and Robert Ondrak for help with troubleshooting of the softwares. From the bottom of my heart, I would like to give special thanks to my supervisors, Maarten de Wit, Zahie Anka and Rolando di Primio for their undivided time and assistance to my thesis. Without them, this project would have not been possible.

Thank you.

TABLE OF CONTENTS

List of Figures

domain, identified in the present-day continental shelf break/upper slope, characterised by shallow-dipping normal listric faults and (ii) a compression domain on the continental lower slope, dominated by landward dipping listric thrust faults. (Location of this composite-line is shown in Figure 9: see text for further information.)

Figure 12 a-e: Cretaceous 3D depth surface maps (a,c,e) and corresponding thickness maps (d,b) of exploration Block 2. The arrows point to the North.

Figure 12 f-j: Cretaceous 3D depth surface maps (i,g) and corresponding thickness maps (j,h,f) of exploration Block 2. The erosional unconformities (red surface) are the responses to waves, winds, storms and relative sea level rise. The unconformities in the seismic profile indicate erosion of underlying seismic units. The arrows point to the North.

Figure 12 k-o: Tertiary 3D depth surface maps (o,m,k) and corresponding thickness maps (n,l) of exploration Block 2. The horizon, 'Inner Tertiary' (Cenozoic) (Weigelt and Ünzelmann-Neben., 2004) is a 14 Ma horizon (Neogene) that separates T1 from T2.The arrows point to the North.

Figure 13- Regional seismic transect across the Orange Basin offshore southern Namibia showing the main depositional mega-sequences and the late Cretaceous gravity-driven slide system. This example shows both the extensional domain and compression domain with a toe thrust system. U/c stands for unconformity (from De Vera et al., 2010).

Figure 14: Classification chart used to identify the gas chimneys in this study.

Figure 15a: The bathymetry of the study area, showing the distribution of three classes of major gas chimneys identified in this study: (purple) stratigraphic controlled chimneys, (red) structural controlled chimneys and (grey) paleo chimneys. Note that the structurally-controlled chimneys are confined to the deep basin and steepest slopes, while the stratigraphically-controlled chimneys dominate the middle and upper shelf. The location of a giant collapsed chimney is marked by a black square. (The composite regional seismic section depicted in Figure 11 is shown as a bold black line).

Figure 15b: 3D view showing the progradation of the continental margin since Albian (14At1). Note that the structurally-controlled chimneys (red) are confined to the extensional domain of the slope, whilst the stratigraphically-controlled chimneys (purple) are confined to the middle and upper shelf (from Petrel software). The arrow points to the North.

Figure 16: Active structurally-controlled chimney mapped in the outer margin of the Orange Basin. The chimney is sealed at about 0.1 sec (TWT) below the sea surface, below a flat seismic anomaly indicative of free gas (For location, see Figure 9).

Figure 17: Close up view of a structurally-controlled chimney that terminates as a seafloor mound with anticline-crestal faulting. The gases migrate up the faults to the exposed mound. The two NE dipping conjugate faults converge at depth within a major SW dipping normal fault (black bold lines). The faults are indicated with arrows. Note that the chimney is contracted by antithetic faults and the roll-over structures that merge in the decollement zone (For location, see Figure 9).

Figure 18: Active stratigraphically-controlled chimneys along the middle margin of the Orange Basin. Note how free gases migrate through the sedimentary column from the Aptian layer (13At1) and the lack of faulting. The bright spots indicate the presence of hydrocarbons trapped close to the surface. The pockmarks are about 300 m wide (For location, see Figure 9).

Figure 19: Giant chimney terminating in a collapse crater of more than 7 km in diameter. Note the lateral bright spots in the lower sections of the chimney and the absence of internal seismic "pull-downs". The red square represents the detailed view of near-surface collapsed crater shown in Figure 20. For location, see Figure 9.

Figure 20: a) Detailed view of a near-surface collapsed crater. b) Schematic interpretation of collapse (i) The cluster of pockmarks are created by the gases leaking to the surfaces. (ii) Gas migration and onset of chimney formation during collapse. (iii) The crater is buried by overlying sediments (T1). The thickness variations of T1 indicate that the sediments were deposited during the chimney collapse. (iv) Deposition of sediments (T2) overlying T1, starting at 14 Ma, marks the end of the collapse. T2 has uniform thickness.

Figure 21: Depth converted model produced by the composite seismic line (see Figure 11) with facies definition (e.g. Kuhlmann et al., 2010) for each unit. Source rocks are shown in grey (see legend). In addition, a SE trending fault (bold black zigzag line) is displayed and the three depth extractions from wells (yellow vertical lines) are shown at the proximal (A), middle (B) and distal locations (C) of the basin at 9,320m, 182,230m, and 198,662 m distances, respectively. Legend names cannot be corrected because the software is not available.

Figure 22: Simulation of erosion events by identifying the initial thickness of horizons before they were eroded, using Petromod (see text). The blue zigzag line marks the unconformity 18At1 (77.5 Ma) and the red zigzag line marks the Inner Tertiary Horizon (ITH-14Ma horizon, see Figure 2).

Figure 23: Simplified graph showing calculated variations of sea floor temperatures (Wygrala 1989) between 0 and 360 Ma.

Figure 24: Heat flow model showing rifting at 125 Ma, followed by thermal decay (thermal subsidence) to present (based on McKenzie 1978).

Figure 25: Linear temporal interpolation between rift initiation (sea level=0 ma) to present day. The graph shows the present day water depth vs. the length of the model in meters (side-axis and top-axis respectively).

Figure 26 a-b: Predicted and observed (a) temperature and (b) vitrinite reflectance plotted for wells A-I1 and K-H1. The best fit lines for vitrinite reflectance derived from kinetic modelling are shown. Note the mismatch in temperatures for well A-I1 and in vitrinite reflectance for well K-H1 between the best fit line and observed data at depths 3000m to 4500m. The graphs were constructed at location B shown on Figure 21.

Figure 27: (a-b) Predicted and observed variations of vitrinite reflectance (a, c) and temperature (b, d) plotted for wells A-I1 and well K-H1 after improvement of the model by adding several boundaries and fitting the facies according to the chronostratigraphic chart. The graphs were constructed at location B shown on Figure 21.

Figure 28: 2D model of the degree of kerogen conversion (Transformation Ratio) in the present day cross-section. The horizontal axis is the length of profile (220 km), the left axis shows the depth of profile (11 km), and the right axis delineates the names of stratigraphic horizons.

Figure 29: 2D model of the vitrinite values for the present day of study area cross section. The horizontal axis is the length of profile (220 km), the left axis shows the depth of profile (11 km), and the right axis delineates the names of stratigraphic horizons.

Figure 30: Model of the vitrinite variation over time in all four source rock is at locations A (proximal), B (middle) and C (distal). All four source rocks start to mature in the early Cretaceous, reaching a maximum maturity at the late Cretaceous, after which there is no further maturation. The Cenomanian/Turonian source rocks is the least mature and the Hauterivian source rocks is the most mature.

Figure 31: Model of maturation of all four source rocks at locations A, B and C (Figure 21). Note the major step in the Hauterivian source rock (black line), which has the highest transformation ratio (see Figure 28).

Figure 32: Model of burial histories at location A, B and C (Figure 2) with temperature overlays (see legend, blue=cold, red=warm). The burial history is a simple depth versus time plot in that deposition (and related burial) as well as times of non-deposition, and uplift are regenerated.

Figure 33 a-e: Graphs showing reconstructed evolution of the basin. a) From synrift to Cretaceous horizon 6At1. b) Deposition of Cretaceous unit 1. c) Deposition of Cretaceous unit 2. d) Deposition of Cretaceous unit 3. e) Deposition of Cenozoic units. Legend names cannot be corrected because the software is not available.

Figure 34 (a): A migration model showing gas migration at the present day. Hydrocarbon migration is shown as maroon dotted lines and can reproduce the associations observed in the TWT seismic data (b) showing identified gas chimneys. The red block on the migration model (a) represents a section of the composite seismic line (b) chosen for basin modelling. The vertical lines represent the identified gas chimneys.

Figure 35: Migration paths and degree of kerogen conversion (Transformation Ratio) for Model 2. The dotted lines show the migration paths (gases=red and liquids=green). The colour ranges in the source rock intervals represent the Transformation Ratios (see legend).

Figure 36: Graphs comparing the expulsion rates of hydrocarbons between Models 1 and 2. Note the more focused outflow of Model 2 centred about 80 Ma.

List of Tables

Glossary

Biogenic gas	Natural gas produced by living organisms or biological processes. E.g. anaerobic bacterial decomposition of sedimentary organic matter.
BSR	Bottom Simulating Reflector representing the base of the gas hydrate stability field.
Cap rock	A seal of impermeable rock found on top of oil or gas reservoir.
Darcy Flow	Such flow assumes fluid-flow velocities that are mainly a function of sediment permeability, fluid viscosity and a pressure gradient.
Depth Conversion	Transformation of seismic reflections from a scale of time defined by seismic velocities (Two Way Time travel) to a scale of depth in meters.
Dry gas	Gas without liquid hydrocarbons or water (vapour).
Exosphere	The combined hydrosphere and atmosphere.
Gas Chimney	A pseudo-vertical subsurface seismic anomaly characterised by decrease in seismic amplitude and wipe-outs due to migrating gas.
Gas hydrate	A solid form of water that contains a large amount of methane within its crystal structure. Low temperature and/or relative high pressure are required for it's formation, as found in deep sea sediments (in water depths greater than ~300 m) and below surface in permafrost regions.
Hydrogen Index	The Hydrogen Index represents the kerogens hydrocarbon potential. It is measured using the Rock Eval (open-system bulk pyrolysis). Amounts of hydrocarbons generated between 300 and 600°C at a heating rate of 25°/min are monitored and expressed as mg HC/g Total Organic Carbon.
Invasion Percolation	Migration is viewed as the invasion of a non-wetting hydrocarbon phase through a network of opposing capillary pressures. Hydrocarbons need to exceed breakthrough pressure to migrate in stringers.
Kerogen	Solid, insoluble sedimentary organic matter.
Kerogen Type I	Mainly algal and amorphous kerogen and highly likely to generate oil, under favourable conditions.
Kerogen Type II	Mixed terrestrial and marine source material that can generate oil and gas, under favourable conditions.
Kerogen Type III	Woody terrestrial source material that typically generates gas, under favourable conditions.
Kinetics	Study of rates of (chemical) processes.

Migration	Movement (of hydrocarbons) from source to sink (reservoir rocks).
Mud volcano	Surface structures formed during the expulsion of liquids and gases from the subsurface.
Pockmarks	Circular- to oval-shaped depressions in sea bed caused by the release of subsurface fluids or gas from sea floor sediments.
Paleo-pockmark	Fossilized pockmark. E.g. Ancient (buried) pockmark that is no longer active.
Pinch-out	Termination by thinning of a sequence against another unit. Pinch-outs often create a favorable geometry to trap hydrocarbons.
Seepage	Percolation of subsurface fluid or gas to the surface.
Source kitchen	A subsurface region where the source rock has reached appropriate conditions of pressure and temperature to generate hydrocarbons.
Source rock	A sedimentary rock rich in organic matter that can generate petroleum.
Thermogenic Gas	Gas formed through natural thermal cracking of organic material to oil and gas.
Transformation Ratio	Ratio of generated petroleum to potential petroleum in a source rock.
Total Organic Carbon	The amount of organic carbon in a sediment sample.
Vitrinite Reflectance	It is a measurement of the percentage of light reflected off the vitrinite maceral at high magnification in oil immersion. Desribed as a reflectivity percentage (%Ro).
Well Top	Point of contact between a well and a surface (a horizon, a fault, or fluid contact surface).
Wet Gas	Gas that contains a large amount of associated liquid hydrocarbons and water.

Acronym list

BSR	Bottom Simulating Reflector
C1-5	Cretaceous seismo-stratigraphic units
GEM	Geologic emissions of methane
HC	Hydrocarbon
HF	Heat Flow
HI	Hydrogen Index (mg HC/g TOC)
ITH	Inner Tertiary Horizon
PETM	Paleocene-Eocene Thermal Maximum
PWD	Paleo Water Depth
Ro	Vitrinite reflectance
S-c	Structurally-controlled
Sa-c	Stratigraphically-controlled
SDR	Seaward Dipping Reflectors
SWIT	Sediment-Water Interface Temperature
T1-2	Tertiary (Cenozoic) seismo-stratigraphic units
TOC	Total Organic Carbon
TST	True Stratigraphic Thickness
TWT	Two-Way Travel Time

1. INTRODUCTION

1.1. Scientific questions: problems and objectives

Sedimentary basins off-shore passive continental margins are potential hydrocarbon storehouses where liquid and gaseous hydrocarbons accumulate in reservoirs buried across these margins. One gaseous hydrocarbon commonly found in most sedimentary basins, is methane (CH_4). In many places, hydrocarbons leak from such accumulations or migration pathways lead directly to the basin surface. Migrating hydrocarbons separate into oil and gas phases upon decreasing temperature and pressure, and gas phases containing mostly methane dominate at the shallowest levels. In many cases, such as well described along the continental shelf of Norway (Brendt, 2005; Svensen et al., 2003; Bunz et al., 2005; Mazinni et al., 2006), in the Black Sea (Dimitrov, 2002) and the Sea of Okhotsk (Cranston et al., 1994), methane escapes across the sea floor via carbonated gas seeps and mud volcanoes, into the exosphere (i.e. the combined hydrosphere and atmosphere) where it eventually oxidizes to form CO_2 (e.g. Kennett et al., 2002; Etiope and Klusman 2002 and Judd et al., 2002 : Figure 1). If large rates of methane leakage occur, the volumes released may then contribute significantly to

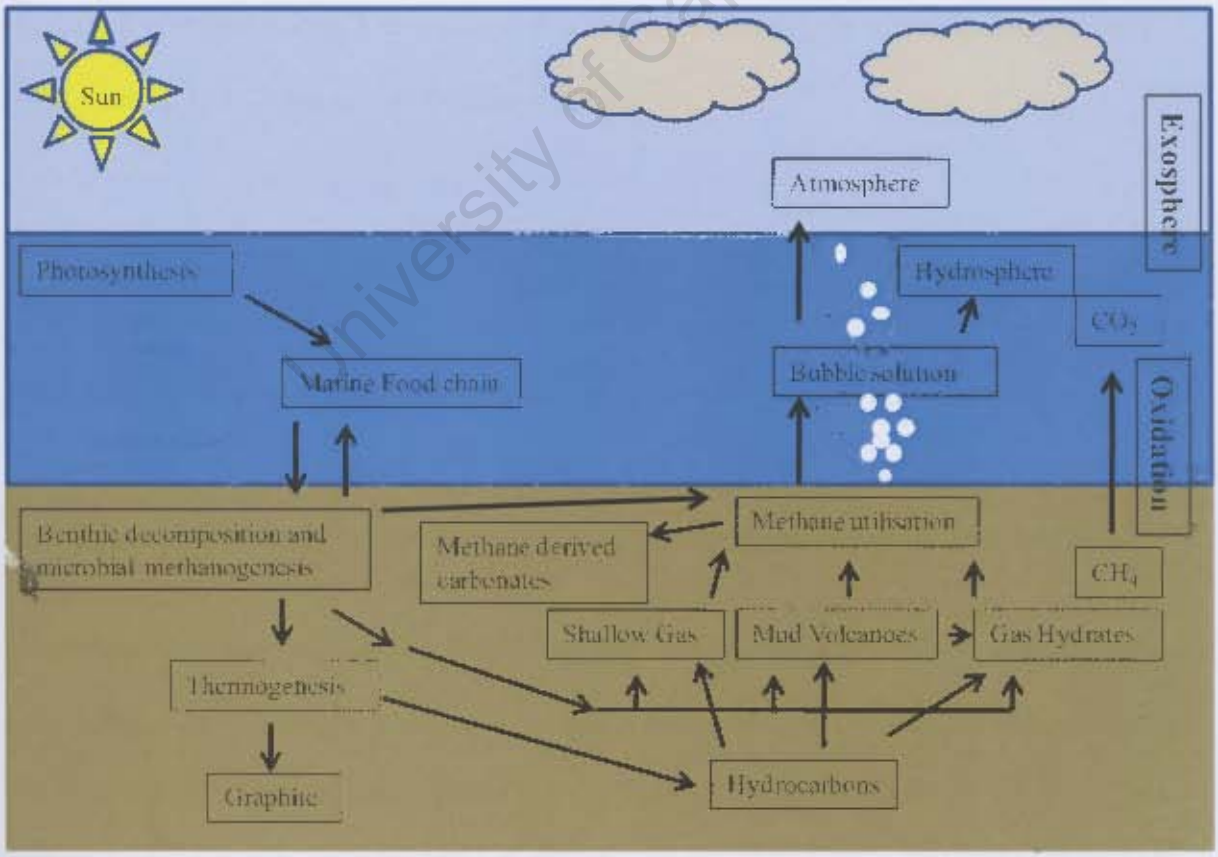

Figure 1: Sources and pathways of geological methane (Modified after Judd et al., 2002).

Earth's climate. Methane is the most abundant hydrocarbon in the sedimentary basins (e.g. Etiope et al., 2008) and its storage and/or escape can greatly affect exosphere temperatures because CH_4 is at least twenty times more potent than CO_2 as a greenhouse gas (Wuebbles et al., 2002; Svensen et al., 2004).

The sources and sinks of the global methane budget are dynamic and appear at times imbalanced (Crutzen 1991 and Etiope 2004). For example, Crutzen (1991) proposes a methane imbalance of 50 Tg yr^{-1} whose source is "missing". This imbalance appears to be related to geologic emissions of methane (GEM) where significant amounts of methane are released naturally into the atmosphere through faults and fractures (Etiope and Klusman, 2002). Recently, Etiope (2004) suggests that these values of GEM are in the range of 40-60 Tg yr^{-1} and proposes that these GEM should play a major role on the balance of the global budget of greenhouse gas. The sources of these gases also remain controversial (Crutzen 1991; Etiope and Klusman., 2002; Etiope 2004).

Recent analyses of Earth's geohistory (van de Schootbrugge et al., 2008; McElwain et al., 2009), based on the past episodes of global warming, provide insights into the coupling of climate and the carbon cycle which, in turn, help to predict the future consequences of anthropogenic carbon emissions. For example, sudden releases of geologically stored methane in the past are believed to have been responsible for rapid rises in global temperatures

and changes in climate (Whiticar 1989; Dickens 2003; Svensen et al., 2004; Zachos et al., 2008). It has been suggested that rapid (catastrophic) release of methane probably happened 55 million years ago, catalyzing the Paleocene-Eocene Thermal Maximum (PETM), when global temperature increased by 5 °C in less than 10,000 years (Svensen et al., 2004; Zachos et al, 2008). The tell-tale signs are increased acidification of the ocean and a sudden carbon

isotopic excursion likely due to the injection of a very large mass of ^{13}C- depleted carbon into the atmosphere (Svensen et al., 2004). The source of the carbon is likely from clathrates (methane hydrates) or methane gas leakage from gas reservoirs along continental margins. The consequences of such abrupt leakage can lead to an increase in mean global temperature, as recorded in the stratigraphic records, but it can also affect atmospheric and ocean circulation, precipitation patterns and intensity, as well as, the coverage and thickness of sea ice and continental ice-sheet stability (Zachos et al., 2008). Among the mechanisms resulting in hydrate dissociation changes in sea surface temperatures are paramount as they can trigger the dissociation of methane hydrates, releasing methane and in turn creating additional warming through this positive feedback (Dickens 2003).

It is not known with any degree of certainty if methane release from deeper gas reservoirs within sedimentary basins also contributes to such events (e.g. Svensen et al., 2004; Brendt 2005). The characterisation and quantification of thermally-driven methane emissions from rich oil-bearing sedimentary basins may therefore provide key insights to better differentiation between anthropogenic related CO_2-increase in the exosphere and that derived from natural causes.

This study aims at identifying, characterizing and modelling, through geologic time, the leakage of liquid/gas hydrocarbons in a major sedimentary basin, the Orange Basin, offshore the western South African margin. These results may help to understand the relationship between methane migration and seepage with structural and stratigraphic elements in this basin, and will contribute to a better quantification of the fluxes of greenhouse gases from sedimentary basins to the exosphere.

1.2 The Study Area and the Orange Basin

1.2.1 Geographic characterisation of the study area

The Orange Basin is located offshore the south-west facing continental margin of South Africa. It has an area of approximately 130 000 km ^{2} (Paton et al., 2007). It is bounded to the north and south by the Walvis Ridge and by the Agulhas-Falkland Fracture Zone, respectively (Figure 2). The basin has been filled by sediments transported by the Olifants and Orange River drainage systems (Figure 2). The sediments range in age from the Mesozoic to Recent (Gerrard & Smith., 1982; Dingle et al., 1983; Muntingh 1993; Brown et al., 1995).

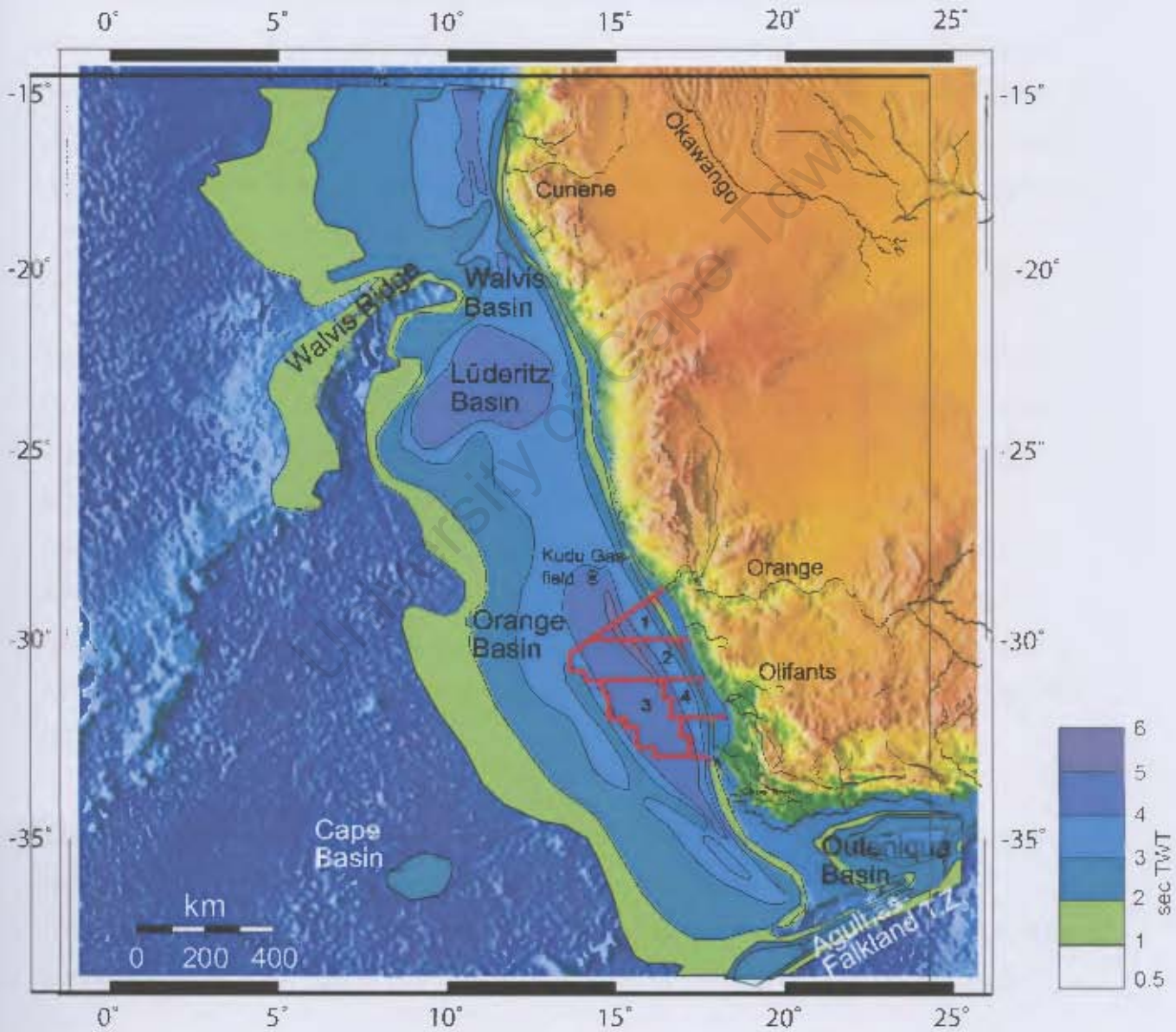

Figure 2: A physiographic map with the superimposed isopach maps (TWT of bed thickness) showing the Orange Basin. It is located offshore southern Africa between the Walvis ridge in the north and the Agulhas-Falkland Transform Zone in the south [modified from Kuhlmann et al., (2010)]. Exploration blocks 1-4 (red lines) are shown. The study area covers exploration Block 2 of the Orange Basin.

The Orange Basin is divided into several exploration blocks. Previous studies were conducted by Kuhlmann et al (2010) on Block 3 and 4, and by Paton et al. (2007 and 2008) in the southern part of the basin (Figure 2). Exploration Block 2, the focus of this study, is located in the northern part of the basin and covers an area of approximately 18750 km ^{2}.The length of the block extends over a distance of about 250 km from the margin in the shallow marine domain at 200 m water depth to the deep marine domain at 3000 m water depth.

1.2.2 Regional geological context of the study area

The Orange Basin records the development of South Africa's volcanic-rifted passive continental margin from the Late Jurassic through the Cretaceous until the Present (Gerrard & Smith, 1982; Muntingh 1993; Brown et al., 1995 : Figure 3). The basin contains a thickness of about 7 km of sedimentary sequences in the northern area and about 3 km-thick sedimentary sequences to the south that formed in response to the Gondwana break-up and during opening of the South Atlantic Ocean (Figure 4a). These sediments are sourced from onshore weathering and erosion (Gerrard & Smith, 1982; Brown et al., 1995; Tinker et al., 2008).

The margin formed during the break-up of Gondwana and the opening of the South Atlantic Ocean during the Late Jurassic to Early Cretaceous (Gerrard and Smith., 1982; Brown et al., 1995; Nurnberg & Muller., 1991; MacDonald et al., 2003; Moulin et al., 2010). Recently, Moulin et al. (2010) have tried to refine the pre-opening fit between Africa and South America and to evaluate the age of the break-up and onset of sea floor spreading, based on new interpretations of magnetic anomalies, seafloor isochrones and radiometric dating of igneous rocks. From those data, they propose that the first oceanic crust between southern Africa and America in the lower Cretaceous formed between magnetic anomalies M9 and M7 (134-132 Ma).

The early formation of the continental margin shows features of volcanic activities, such as continental flood basalts (Etendeka) and volcanic seaward dipping reflectors (SDRs) (Trumbull et al., 2007; Hirsch et al., 2009). SDR are extrusive basalt flows found offshore the continental margin that rapidly extruded across the surface when the plates moved apart.

The break-up of Gondwana resulted in the development of a series of grabens and half-grabens orientated parallel to the present-day margin. The complex of grabens and half-grabens is separated by a medial hinge from a more distal western wedge of seaward dipping

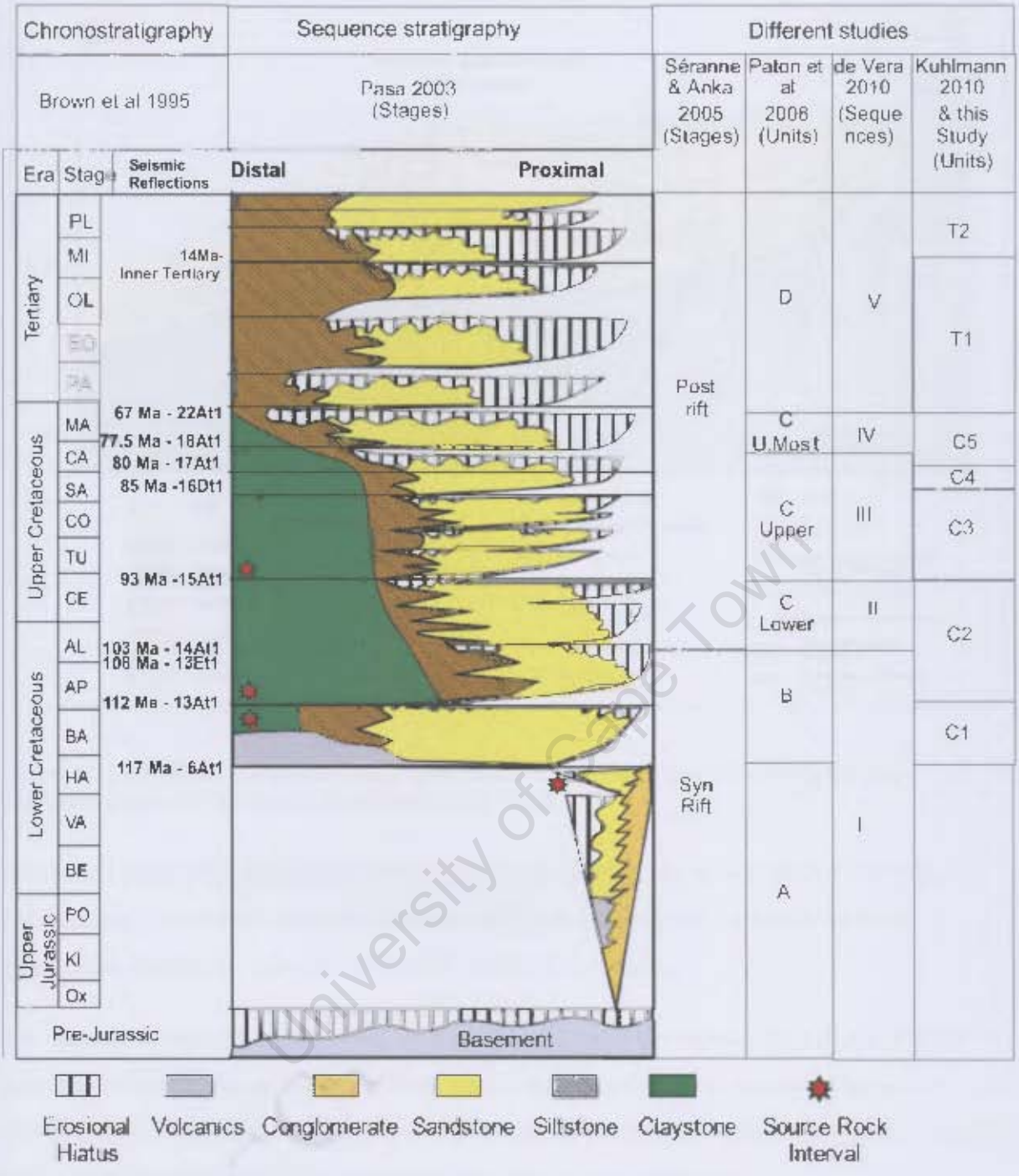

Figure 3: Chronostratigraphic and sequence chart for the Orange Basin showing the major seismo-stratigraphic units and their bounding unconformities according to different authors (i.e. Brown et al., 1995; Séranne and Anka., 2005; de Vera at al., 2010; Paton et al., 2007; Kuhlmann et al., 2010).

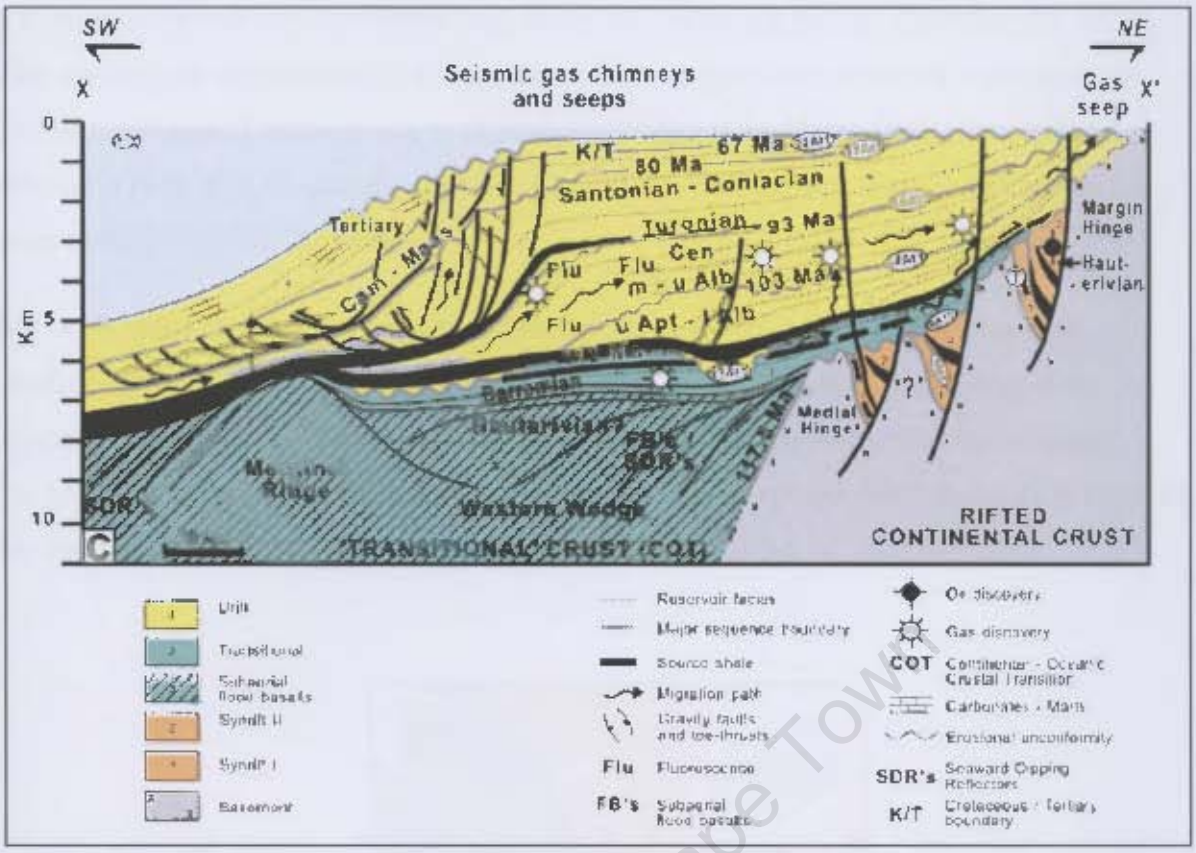

Figure 4a: Generalised composite stratigraphic cross section the Orange Basin with the main petroleum elements highlighted (from Broad et al., 2006).

reflectors (Figure 4a : Jungslager 1999; Broad et al., 2006). The immediately overlying sedimentary successions consist of deposits of Upper Jurassic and Lower Cretaceous siliciclastic, lacustrine sediment infills with volcanic intrusions.

The lacustrine deposits are followed by transitional Lower Cretaceous siliciclastic deposits that show a deepening-up sequence from fluvial red beds to deltaic deposits (Gerrard & Smith, 1982). Full marine conditions set in during the Barremian-Aptian (BA-AP) in response to the initiation of the main drift phase of the South Atlantic opening.

The oldest proven and highest quality source rock interval comprises the syn-rift Upper Hauterivian lacustrine deposits (HA), found within the grabens and half grabens (Jungslager 1999 : Figures 3 and 4a). This source rock is oil-prone, with a TOC of more than 10% and HI of more than 600 mg HC/g TOC (Barton et al., 1993; Muntingh, 1993). Another source rock interval comprises the highest quality of source rocks of Barremian (BA) to Aptian (AP) ages (Figure 3) that appear to be regionally developed within the basin. This sequence was penetrated by DSDP 361 (Deep Sea Drilling project drilling hole 361 ; Figure 4b) and shows

that this source rock is up to 300 m thick with TOC values up to 25% (Herbin et al., 1987). This source rock corresponds to a major lithofacies change from restricted marine to open marine conditions. This sequence is overlain by 1500m thick Upper Cretaceous post-rift sediments (103 My), consisting of clay or claystone lithology, deposited basinward on the outer margin (Paton et al., 2008).

Within the post rift Late Cretaceous succession another source rock interval has been identified (Muntingh 1993; Van der Spuy et al., 2003). This interval corresponds to an uppermost Cenomanian-Turonian (CE-TU) maximum flooding event that was identified in the AK1 well (Figure 4b). This interval is expected to be oil prone down dip to the west (Van der Spuy et al., 2003).

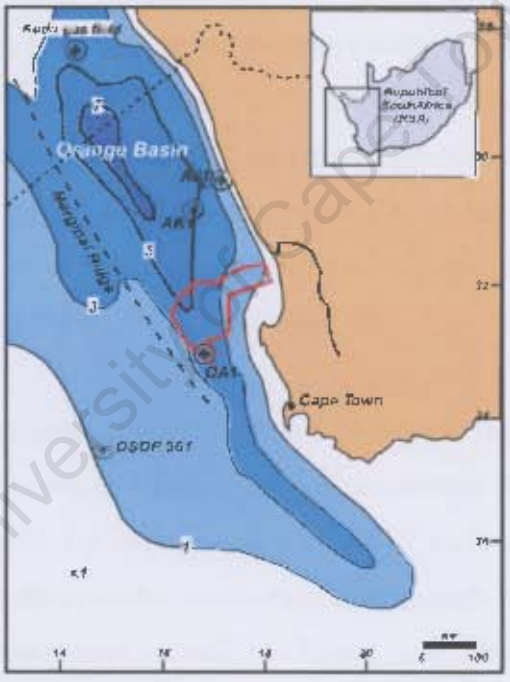

Figure 4b: Orange Basin location map showing some of the locations of wells used in this (after Paton et al., 2007).

1.2.3 Previous work in the Orange Basin

Many other studies have been completed on the continental margin of southwestern Africa, and the Orange Basin in particular. These studies focus primarily on the sequence stratigraphy, biostratigraphy and oceanography. For example, Gerrard & Smith. (1982) distinguished four main seismic horizons T, R, P and L, which form major sequence boundaries that range in age from Mesozoic to Cenozoic. Subsequently, Muntingh & Brown (1993) and Brown et al. (1995) established at least twenty-two stratigraphic sequences bounded by unconformities. Ten of these sequences form the basis for the present interpretation for the Orange Basin (Figure 3).

More recently, Hirsch et al. (2009) developed a tectonic model using a combined approach of lithospheric modelling, subsidence analysis, and basin history inversion in the Orange Basin. Their findings reveal that it is necessary to involve sub-crustal thinning rather than the classical uniform stretching model (McKenzie 1978) in order to explain the post-break up subsidence and maturation of organic matter. Their model predicts a syn-break up setting characterised by shallow water depth and high heat flow due to differential thinning and associated underplating, followed by subsequent thermal cooling, affected by two additional phases of sub-crustal thinning about 70 Ma after break up.

It has been suggested that the onset of the Benguela Current was responsible for major depositional changes along the western part of the African margin (i.e. Séranne and Abeigne, 1999; Séranne and Anka, 2005). For example, Weigelt and Ünzelmann-Neben (2004) proposed that sedimentary features on the continental margin such as slump scarps are triggered by bottom currents and slope instabilities linked to increased sedimentation rate and upwelling under the action of the Benguela Current in the middle Miocene. On the other hand, Viola et al. (2005) show some of these instabilities to be at least partially associated with onland neotectonic structures in southwestern Africa.

Based on the presence of gravitational slump structures, Dingle and Robson (1992) and Brown et al. (1995) described west-dipping growth faults in the outer margin of the Orange Basin. Recently, De Vera at al (2010) studied the thin-skin structures of the basin and proposed that the margin's tectonic instability is recorded as a series of short-lived gravitational-collapse episodes from Middle Aptian to Santonian. Gravitational collapse

probably resulted from episodic continental uplift (e.g. the Kalahari epeirogeny de Wit 2007) combined with differential subsidence and sliding along an efficient detachment layer in Turonian source rocks.

The existence of active petroleum systems within the Orange Basin has been documented by various authors such as Jungslager (1999), Van der Spuy (2003), Paton et al. (2007 and 2008), and Kuhlmann et al. (2010). Paton et al. (2008) carried out a 2D petroleum system model within the southern part of the basin (Figure 3). Kuhlmann et al. (2010) interpreted the seismic units of exploratory Blocks 3 and 4, to the south of Block 2 (Figure 2 and 3) and constructed a 3D basin model for this area. Their results suggest that the early Aptian source rock is the most likely source for thermogenic gas in the outermost part of the basin. They also suggested that this gas would have subsequently migrated laterally to the proximal areas, because the source rocks located on the inner shelf are not mature enough to explain these gaseous hydrocarbon accumulations (Kuhlmann et al., 2010).

In the northern part of the Orange Basin, a series of mud volcanoes have been identified in the outer margin of Block 2 at water depths of about 420 m (Ben-Avraham et al., 2002). This work does not explore the origin of these mud volcanoes within the regional tectonic framework. However, Viola et al. (2005) suggest that these mud volcanoes are associated with deep-seated active faulting linked to neotectonic activity in the submerged continental shelf and on land. Tinker et al. (2008) have also evaluated the balance between onshore erosion and offshore sediment accumulation in southern Africa, based on new apatite fission track thermochronology results. They concluded that the increase in sediment accumulation matches increased onshore uplift and denudation. The tectonic uplift was greatest in the mid-late Cretaceous which is consistent with the onshore uplift and major topographic development of the Kalahari Plateau (e.g. de Wit., 2007).

The occurrence of gas hydrates in sedimentary sequences can be detected in seismic profiles as a Bottom Simulating Reflector (BSR). A BSR is a sub-seafloor phenomenon that marks the boundary between sediments containing gas hydrates from free gas with higher and lower seismic velocities, respectively (Haacke et al., 2007). A BSR recorded in seismic reflection data, a few hundred meters below the sea bed, runs parallel to the sea floor reflector, has inverse polarity to the seafloor reflector and it also cross-cuts the stratigraphic reflectors (Rodrigo et al., 2009). Even though the controls on gas hydrate formation are not fully

understood yet, gas hydrates can occur without the presence of a BSR. Although Ben-Avraham et al. (2002) mapped a BSR, indicative of gas hydrate presence near the series of mud volcanoes in Block 2, no BSR was detected in this area during this study, or farther to the south (Kuhlmann et al., 2010).

1.3. Overview of Gas Escape Features

Occurrence of gas seepages in sedimentary basins can be recognised through many seafloor features including mud volcanoes (Dimitrov 2002; Milkov 2000), mounds (Hovland & Thomsen., 1997; Naeth et al., 2005), and pockmarks (i.e. Hovland & Judd., 1998; King & MacLean., 1970; Pilcher 2007).

There are two types of seepage structures whose end-members are "active" and "passive" (Abrams 1996). Seepage activity is defined as "active" where there is ongoing leakage of hydrocarbons in large concentrations within and above the surface sediments. Seepage is defined as "passive" when the leakage of hydrocarbons from subsurface to near-surface sediments is low or absent. Research on mud volcanoes is important for petroleum exploration because they indicate evidence of high petroleum potential in the deep sub-surface.

The origin of present-day free gas at the sediment-water interface is commonly attributed to either deep thermogenic hydrocarbon sources (i.e. Limonov 1997; Heggland 1997; MacDonald et al., 2000), shallow biogenic processes (Judd et al., 1997) or the dissociation of gas hydrates (Cole et al., 2000; Van Rensbergen et al., 2002; Wood et al., 2002).

1.3.1 Seafloor mounds

Natural gas leakage associated with seafloor mounds can be identified by topographically well-defined build-up of organic mounds or mounds formed by inorganic accumulation of mud (Riding 2002). Free gas can be easily recognised on the seismic data as free gas reduces the acoustic impedance, thereby creating acoustic turbidity and blanking, pull-down of seismic reflections and enhanced reflections such as bright and flat spots (Ben-Avraham et al., 2002; He at al., 2007).

Seafloor mounds have been described along many continental margins of all continents in a variety of tectonic settings (Figure 5a). For example, mud volcanoes in the east Mediterranean Ridge (an active accretionary complex) occur in a subduction environment, whilst the mud volcanoes in the Black Sea occur in a back-arc basin environment (Dimitrov 2002). Examples along passive margins are carbonate mounds formed by organisms that ingest methane and produce carbonate and by precipitation of authigenic carbonates. at water depths from 100 to 350m off Norway (Hovland & Thomsen, 1997) and the Porcupine Basin offshore Ireland (Naeth et al., 2005).

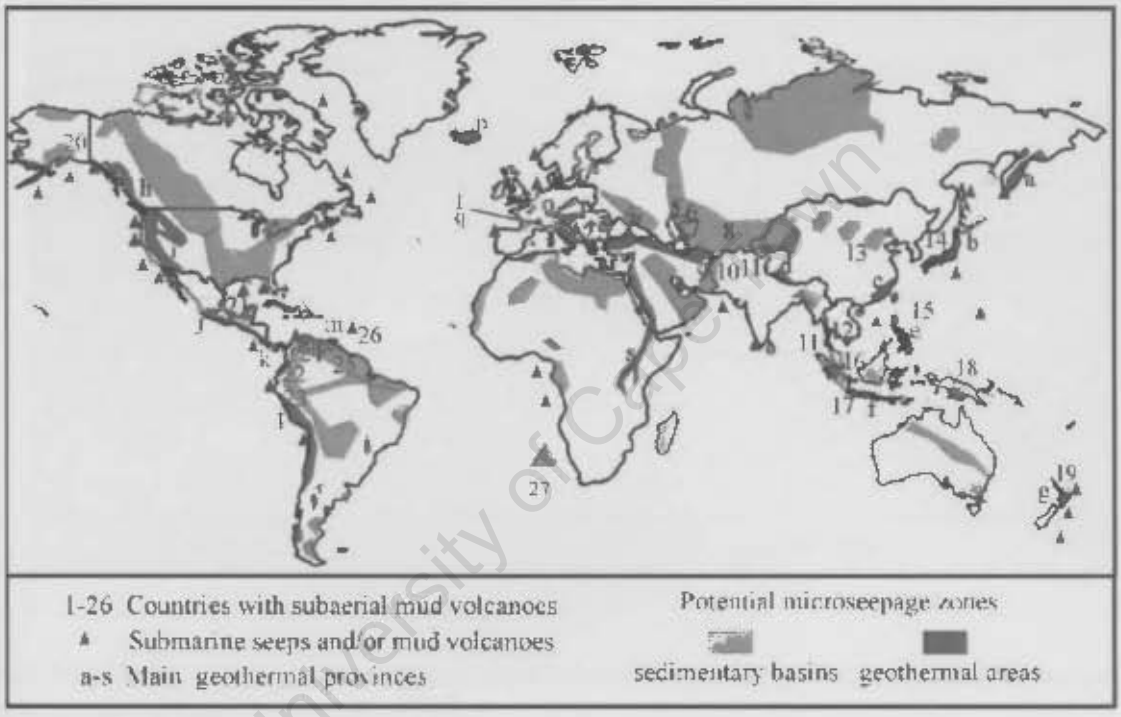

Figure 5a: Global geographical distribution of potential geologic methane emission sites. *Mud volcanoes*: 1—Italy, 2—Albania, 3—Romania, 4—Ukraine, 5—Russia (Caspian, Sakhalin), 6—Georgia, 7 Azerbaijan, 8 Turkmenistan, 9— Iran, 10— Pakistan, 11—India (Punjab, Assam, Andaman and Nicobar Islands), 12—Burma, 13—China, 14—Japan (Hokkaido), 15—Taiwan, 16—Malaysia, 17—Indonesia (Sumatra, Giava, Kalimantan, Sulawesi, Timor), 18—New Guinea, 19—New Zealand, 20—USA (Alaska), 21 Mexico,22 Peru, 23 Ecuador, 24 Colombia, 25 Venezuela, 26—Trinidad. *Main geothermal areas* (includes the high-CO_2 areas from Irwin and Barnes, 1980): a—Russia, b- Japan, c Eastern China, d Himalaya, e The Philippines, f - Indonesia, g—New Zealand, h—Canada, i—United States, j—Mexico, k—Central America volcanic belt, l Andean volcanic belt, m—The Caribbean, n—Iceland, o—Northern Europe, p—Eastern Europe, q—Italy, r—Southern Mediterranean, s—East Africa rift (after Etiope and Kulsman., 2002).

It is frequently difficult to distinguish, based on only seismic reflection data, whether the seafloor mounds represent hard-carbonate accumulations, soft free-venting gassy mud mounds, dormant vents or hydrate mounds (Kaluza & Doyle., 1996). The shapes of the mounds may vary from flat topped, round, to smooth and irregular (Hovland & Thomsen.,

1997; Milkov 2000). Faults may be seen rooted below these mounds (e.g. Figure 5b : Viola et al., 2005). Studies of submarine mud volcanoes over the last decade have increased due to the wide use of side-scan sonar and the increased accuracy of the positioning of bottom samplers (Milkov 2000).

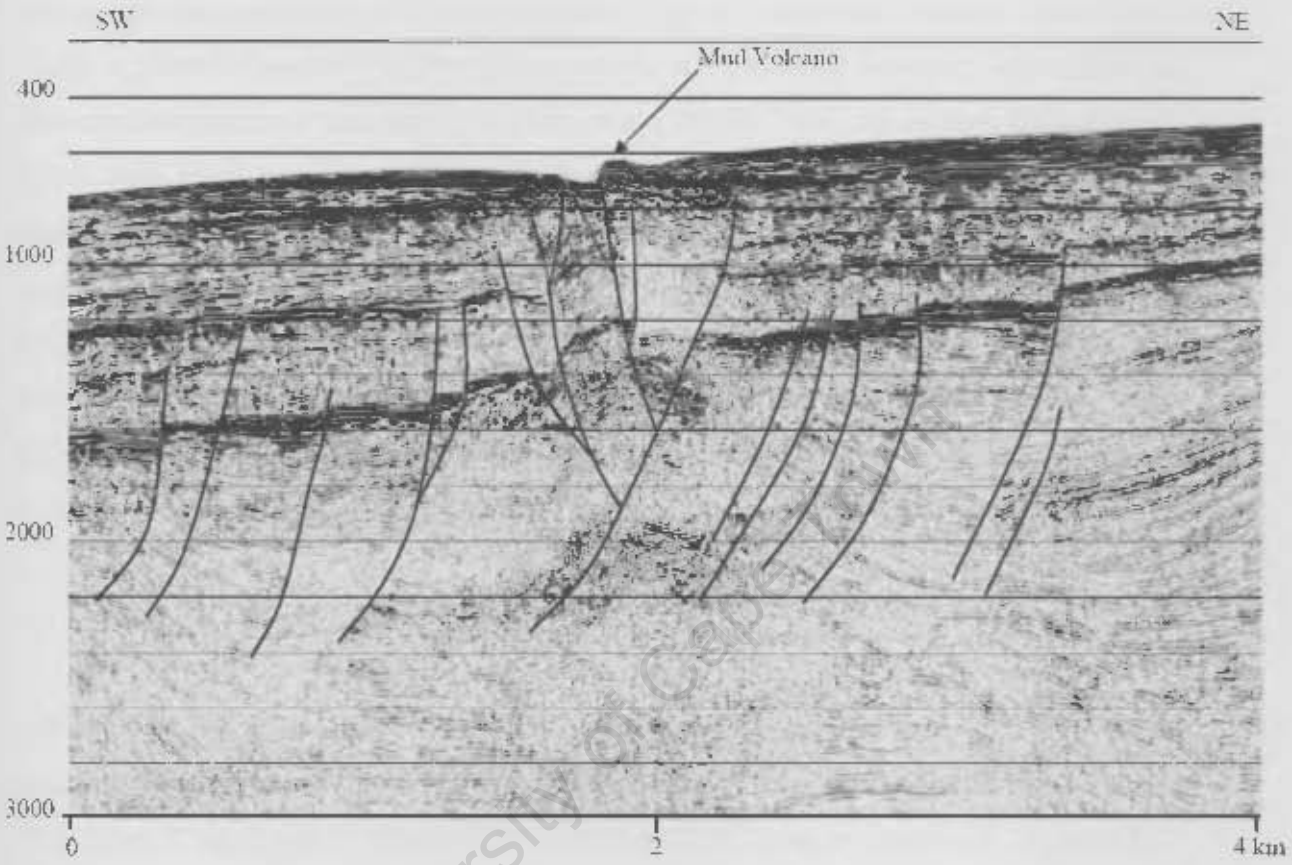

Figure 5b: Seismic section of an interpreted mud volcano in the Orange Basin, showing faults rooted below the mound (from Viola et al., 2005).

Mud volcanoes are topographical features with sub-circular structures up to several kilometres in diameter, elevated above the surrounding seafloor, formed from emission of argillaceous material (Figure 5b: Ben-Avraham et al., 2002; Viola et al., 2005). They are also of interest to bio-geological studies as they represent localized anomalous biological activity (Kaluza & Doyle., 1996; Riding 2002; He at al., 2007).

The overflowing mass of mud in mud volcanoes on the surface comprises a fluid mixture of methane-enriched mud and mud-breccia (Dimitrov 2002). Mud volcanoes most probably originate in areas with high sedimentation rates of fine-grained sediments (e.g. muds), rise of fluidized mud along faults and fractures (more common), or as a result of rapid overloading mass of mud on the surface due to rapid sedimentation, accreting or overthrusting (Milkov

2000; Dimitrov 2002). The driving force that makes fluid rise up to the surfaces is associated with high pore-fluid pressures that exceed the internal forces or lithostatic pressure (Dimitrov 2002).

Many carbonate mounds have been discovered along the continental margins. These occur as single or groups of mounds (e.g. the giant mounds in the Rockall Trough off-shore Ireland, off-shore Morocco and Mauritania ; Kenyon et al., 2003). Carbonate mounds have conical shapes often rising some hundred meters above floor. Other types of mounds are similar in shape but have different internal composition compared to their surrounding, containing usually bedded sediments (Kaluza & Doyle., 1996). The origin of carbonate mounds has been debated over the last decade. They are thought to form as a result of light hydrocarbon seepage, through microbial anaerobic oxidation of methane, or due to breakdown of coral build-ups by the trapping of sediments transported as both suspended and bed load (e.g. Kenyon et al., 2003; Foubert et al., 2008).

1.3.2 Seafloor depressions

Active gas escape does not always form positive topographic features. Large depressions observed on the seafloor surface have also been linked to this gas escape (Hovland & Judd., 1998; King & MacLean., 1970; Gay 2006; Pilcher 2007). They are known as "pockmarks" (Figure 6) and they were first reported on the Scotian Shelf by King and MacLean (1970). Pockmarks are concave crater-like depressions that commonly range between 10m to 200m in diameter and can be up to 35m deep. Pockmarks may be circular, elliptical, or composite when individual pockmarks merge into each other.

Using 3D seismic reflection surveys, Pilcher (2007) showed that the distributions of the pockmarks are controlled by fluid migration pathways in shallow sediments. He classified pockmarks into "random" and "non random" pockmarks. The random ones occur singly or appear to have an irregular distribution on the seabed without discernable relationship to each other or to a resolvable surface or subsurface-feature. The "non random" pockmarks have a particular spatial relationship such as linear arrangements (Figure 7). There are also aligned pockmarks where, for example, the pockmarks follow the strike of a (subsurface) fault.

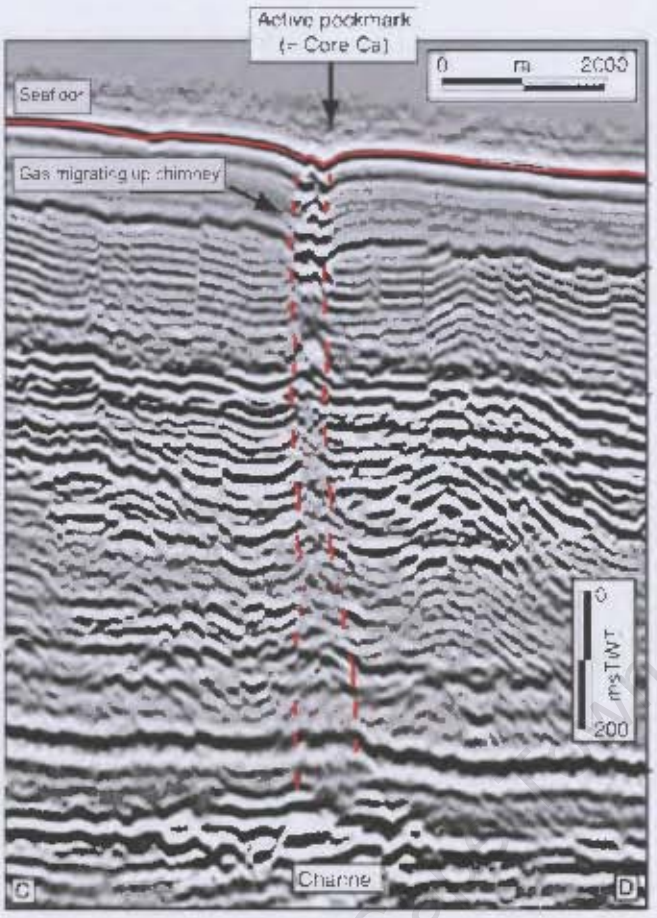

Figure 6: A seismic profile across an upper Miocene turbiditic channel in Angola Basin. This profile illustrates the close relationship between an active "pockmark" as depression on the seafloor and an underlying seismic chimney. The broken red lines mark the shape of the chimney (Gay 2006).

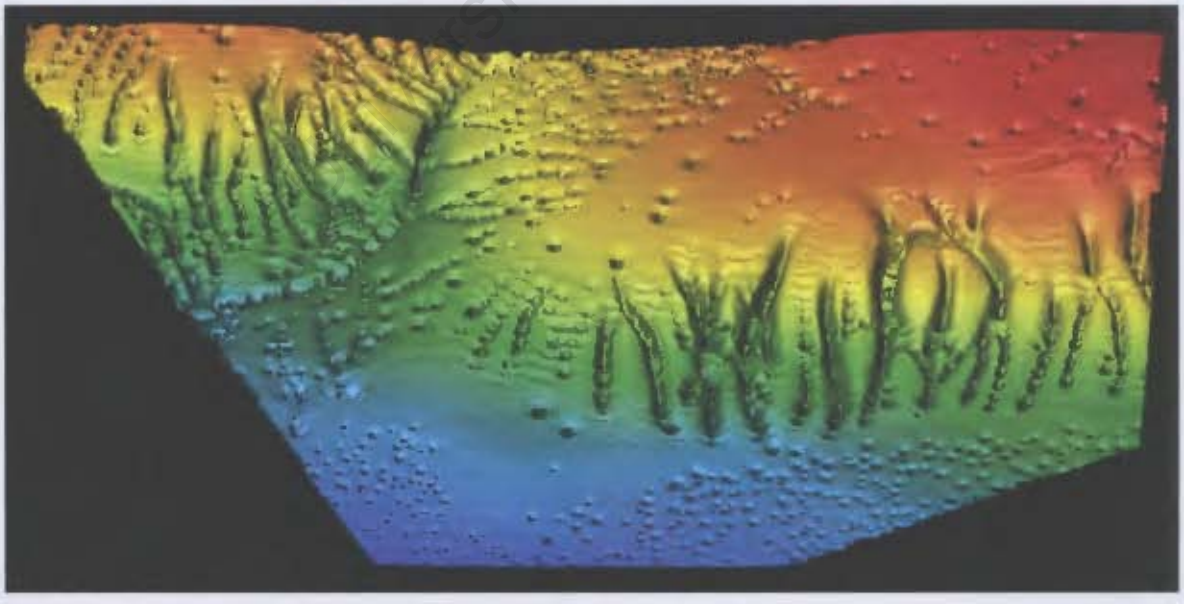

Figure 7: Random and aligned (non-random) pockmarks on the seafloor (viewing direction is from the west), offshore Gabon in water depths ranging from 540 m to 1860 m (blue colours indicate deep water, red colours indicate shallower) (from Pilcher 2007). Note that the random pockmarks are found in the deepest part of the water and the aligned pockmarks are associated with slump faulting along the steep slopes at the continental edge.

1.3.3 Buried gas-leakage features

Gas venting may not always reach the seafloor. Gas migration can be halted by impermeable stratigraphic sequences ("seals") or buried by mass movement deposits as gravity slides (Kaluza & Doyle., 1996). Subsea mounds may also form a bulge in the overlying topography if the fluids continue to accumulate under the seal (e.g. Figure 8).

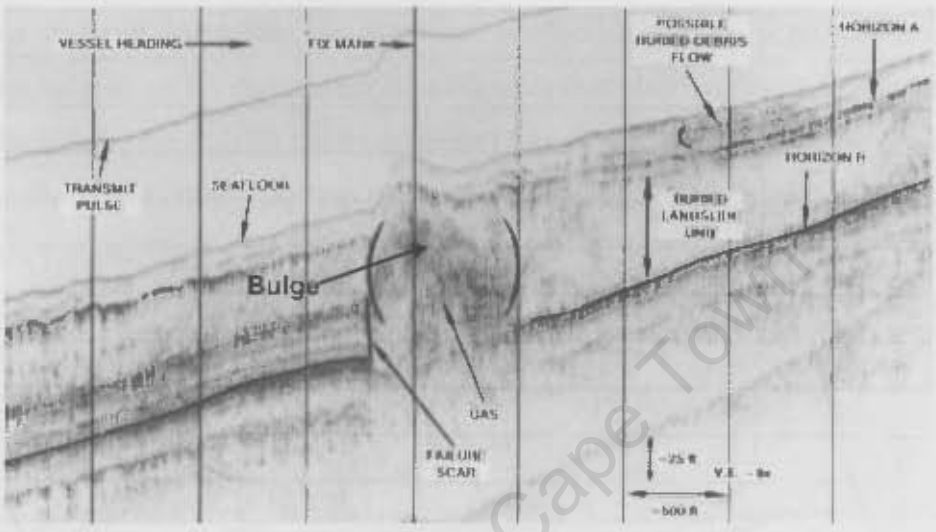

Figure 8: Deep-tow sub-bottom profile showing possible gas entrapped ('bulge') in a buried landslide unit on the continental slope of the Gulf of Mexico (after Kaluza & Doyle, 1996).

2. DATABASE AND METHODOLOGY

This study involves the analysis of a large 2D time-migrated seismic-reflection dataset covering from the shelf to the abyssal plain of the exploration Block 2 in the Orange Basin. Based on seismic identification and seismic stratigraphy techniques, the main seismic sequences, tectonic structures and gas escape features have been identified, mapped, and classified. The observations form the basis for basin models of hydrocarbon generation and migration in the basin. More than 300 2D seismic-reflection profiles, together with data from 10 boreholes located on the exploration Block 2 were provided by PetroSA (Figure 9). The length of the seismic profiles ranges from about 12 km to around 125 km. They run parallel ("strike") and perpendicular ("dip") to the continental margin. The spacing between the seismic lines varies from 0.8 km to 16 km.

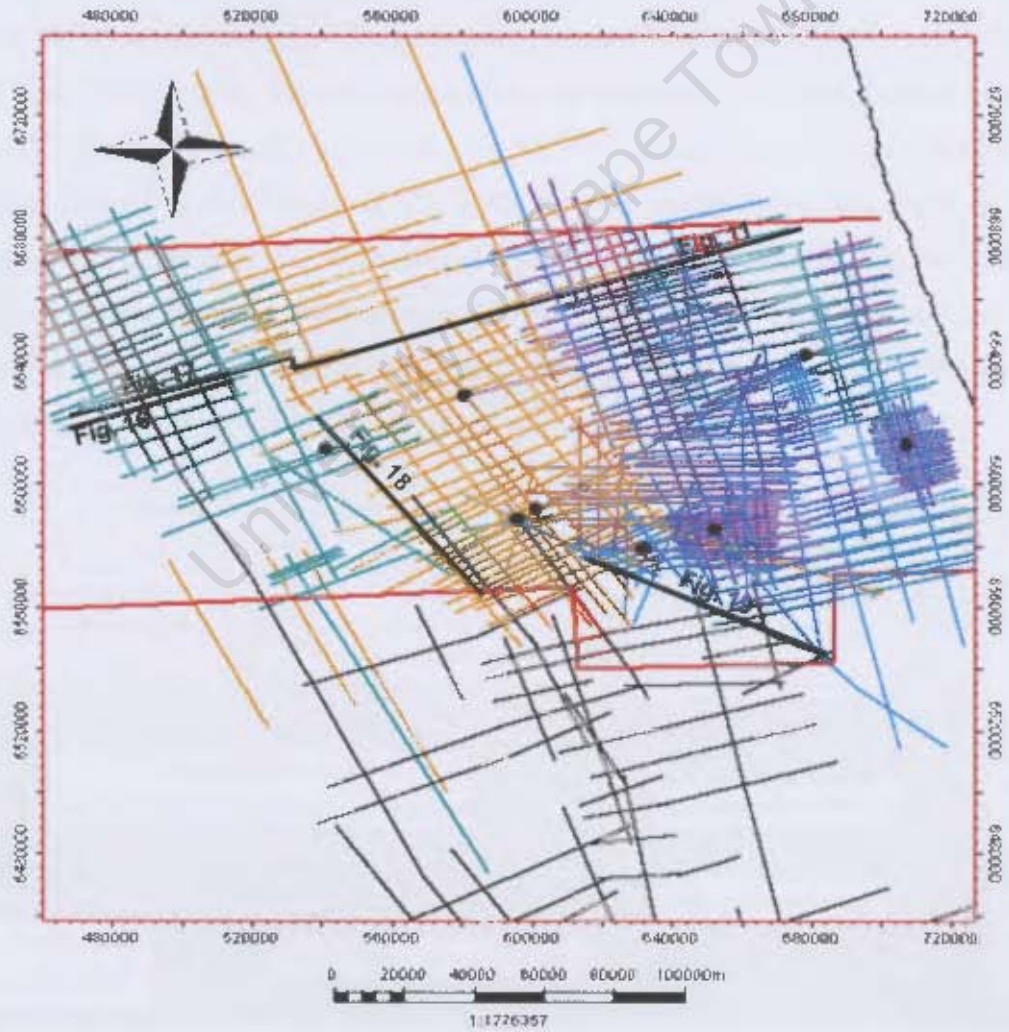

Figure 9: The exploration Block 2 (red block) with the 2D seismic grid (coloured lines) analysed in this study. Also shown are wells (block dots). The black bold lines mark the figures referred to in this study. For location of Block 2, see Figure 2.

Figure 10 depicts a flow diagram with the main methodological steps followed in this work. The seismic reflection data was analysed with Petrel® Interpretation software (Version 2009.1) of Schlumberger. As a first step, the 2D seismic data and the borehole data, which include the logs and check shots, were loaded into the program. The main tectonic structures and seismic reflectors were then identified and mapped. Two-way travel time (TWT) and isopach maps of the horizons mapped were also generated. Any gas leakage features identified on the seismic were classified according to their association to structural or stratigraphic elements and their general distribution across the basin. Finally, the interpreted TWT horizons were converted to depth using the checkshots (time-depth pairs) from the boreholes.

Once the geometry of the basin was constrained, a second phase, including the basin modelling of basin evolution, was performed using the commercial software Petromod ® (Version 10) from Schlumberger. This software simulates the burial and thermal evolution of a given basin, including hydrocarbon generation and migration processes through time. To accomplish this, a representative 220 km-long NE-SW regional transect across the basin was selected and imported into Petromod. The wells provide constraints on sequences age, lithology, paleo-water depths, temperature and maturity (vitrinite reflectance) for model calibration. Once a thermally calibrated model was obtained, final fluid flow and gas migration models were constructed. The results were then compared to and calibrated with the leakage features observed on the seismic section.

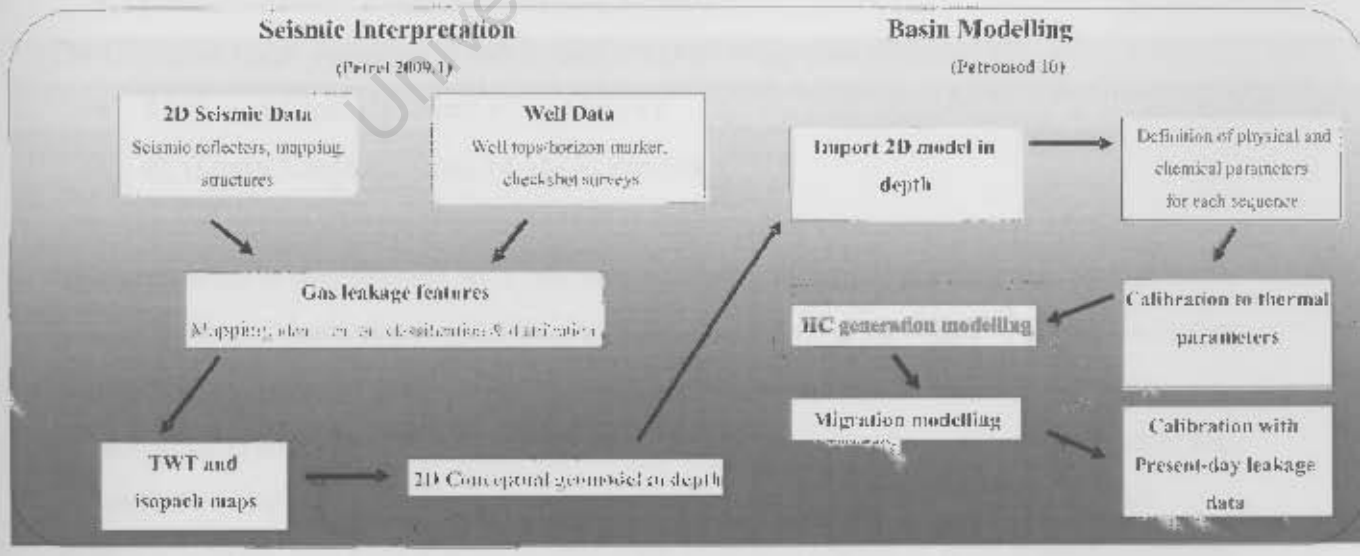

Figure 10: Flow chart displaying procedures applied in this study.

3. RESULTS

3.1. Seismic Interpretation

3.1.1. Seismo-stratigraphic units

Analysis of the seismic data reveals the existence of seven major seismo-stratigraphic units which can be correlated to their age equivalents in the southern area (e.g. Kuhlmann et al., 2010). They form part of two mega-sequences that result from the major stratigraphic changes during the basin evolution: (i) the Cretaceous mega-sequence and (ii) Cenozoic mega-sequence bound by conspicuous stratigraphic unconformities (Figures 3 and 11) (Muntingh & Brown., 1993; Brown et al., 1995; Weigelt and Ünzelmann-Neben., 2004). Note that throughout the text, the name Tertiary (often used in previous studies of the Orange Basin) has been replaced by Cenozoic in order to comply with recent modifications established by the International Commission on Stratigraphy (Gradstein et al., 2004).

The Cretaceous mega-sequence is composed of five seismo-stratigraphic units (Figure 11):

- C1 (Barremian- Aptian) (BA-AP)
- C2 (Early Aptian- Cenomanian) (AP-CE)
- C3 (Turonian- Coniacian) (TU-CO)
- C4 (Santonian) (SA)
- C5 (Campanian- Maastrichtain) (CA to MA)

The Cenozoic mega-sequence is subdivided into two sequences (Figure 11):

- T1 (Lower Cenozoic from 67 to 14 MA),
- T2 (Upper Cenozoic from 14 Ma to Present).

This interpretation is consistent with previous interpretations carried out in the Orange Basin (Figure 3). Ten of the horizons identified by Brown et al., (1995) in the Cretaceous period are used in this study. For example, horizon 6At1, at the base of unit C1 is the drift-onset unconformity (Gerrard and Smith 1982 : Figure 3) and the base of unit C2 is the onset of the drift sequence that is the 13At1 unconformity (Kuhlmann at al., 2010: Figure 3) which corresponds to the major lithofacies change from restricted marine to open marine conditions and 22At1 marks the erosional termination and the base of the Cenozoic wedge which has well-developed prograding clinoforms (Hirsch at al., 2009).

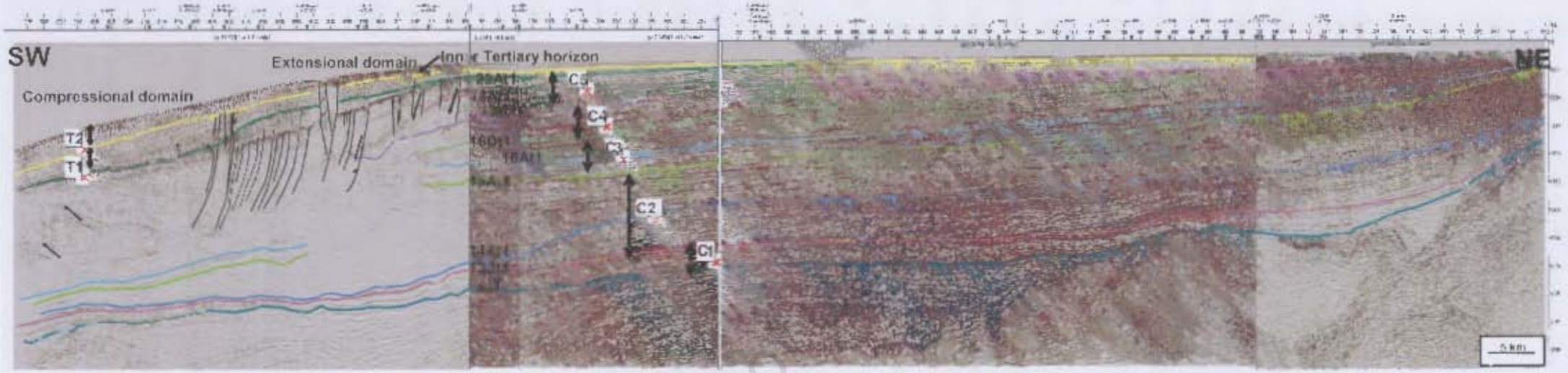

Figure 11: Composite seismic line showing the main identified seismic units (C1-C5, T1-T2) and their bounding surfaces (seismic horizons). The main structural elements of the basin are: (i) an extensional domain, identified in the present-day continental shelf break/upper slope, characterised by shallow-dipping normal listric faults and (ii) a compressional domain on the continental lower slope, dominated by landward dipping listric thrust faults. (Location of this composite-line is shown in Figure 9 : see text for further information.)

3.1.2 Surface and thickness maps

In order to create surface maps I used Petrel® Interpretation software (Version 2009.1) to convert TWT surfaces into depth using a velocity modelling. First, a velocity model is generated using the interval velocity from each well and calibrated to the stratigraphic tops from the available wells. The depth surfaces are tested to fit the well-tops or otherwise corrected. From these surface maps, thickness or isopach maps are then generated using an operation tool called True Stratigraphic Thickness (TST). The latter calculates from differences between the units base and top to yield thickness maps.

The thickness variations of each unit depend on interactive variables such as the sediment supply, sea level changes and the available accommodation. Comparisons between the thickness maps for each seismic unit illustrate the migration of depocentres and the evolution of the sedimentary basin infill through time. One peculiar feature within most units is the north and south trending ridge, which has been related to coarser sandy sediments in lithological descriptions in well reports (Kuhlmann et al., 2010)

The surface 6At1 (117.5 Ma : Figure 12a) represents the base of the first Cretaceous unit, C1 (6At1 to 13At1, 117 Ma-112 Ma). Its depth varies from 1000 m to 6500 m in several areas near the outer margin. The thickness map of C1 (Figure 12b) presents the main depocentre (1500 m thick) in the middle margin. C1 presents particularly high sedimentation rates up to 58.9 m/Ma in the middle margin (Table 1), which may result from a high runoff rate from the hinterland increasing sediment input into the basin (Dingle at al., 1983).

The surface 13At1 (112 Ma) marks the base of the overlying seismic unit C2 (13At1 to 15At1, 112-93 Ma ; Figures 12c & 12d). This depth surface deepens from 900 m to 6000 m in the outer margin. Up to 1750 m thick sediments of C2 were deposited in the central area, thinning out to the east and west. This depocentre is shifted northwards compared to underlying seismic units C1.

The present-day geometry of surface 15At1 (93 Ma) is different to the previous ones because it depicts an enhanced shelf- shelf break- slope configuration (Figure 12e). The margin has prograded about 17 km basinwards, becoming wider and shallower, with a deep slope toe at 900 m that deepens to maximum depths of 5000 m. As the basin opens up into the abyssal plain more accommodation space in the deeper outer margin is available. This configuration allows sediments of C3 (15At1 to 16Dt1, 93-85 Ma : Figure 12f) to fill the space with a

sequence of up to 1250 m thick. There is a clear basinwards shift of depocentres from seismic unit C2 to unit C3. As an increase in sedimentation supply has been registered during C3 deposition (Table 1), most of the sediments must have by-passed the shelf and upper-slope and ended up deposited onto the lower slope and abyssal plain. Tinker et al. (2008) document a similar increase in sediment accumulation during this period of time, which matches increased onshore denudation during the Upper Cretaceous. The latter is consistent with the uplift and major topographic development of the Kalahari plateau (Tinker at al., 2008).

The surface 16Dt1 (85 Ma) marks the base of C4 (16Dt1 to 17At1, 85-80 Ma : Figure 12g). Seismic unit C4 (Figure 12h) is clearly the thinnest sedimentary unit of the basin with maximum thickness of about 500 m in the central region of the study area. Nevertheless, it presents similar sedimentation rate as C3 (Table 1). It may have been subjected to sea levels changes (Séranne and Anka *2005*; Kuhlmann et al., *2010*).

The shape of surface 17At1 (80 Ma : Figure 12i) represents the base of the last Cretaceous unit: C5 (17At1 to 22At1, 80-67 Ma : Figure 12j). The remaining accommodation space is filled with sediments up to 1250 m thick and its main depocentre is in the northwest. Growth faults and toe thrusts dominate this area and could be linked to an increase in thickness which develops during on-going sedimentation and the start on the hanging wall is thicker than the footwall. In contrast, C5 is very thin (up to 300m thick) on the middle and inner-shelf. This is likely to be due to both decrease in sedimentation rate and erosion (Table 1).

Cenozoic units T1 (Lower Tertiary from 67 to 14 Ma : Figure 12l) and T2 (Upper Cenozoic from 14 Ma to Present : Figure 12n) both display similar thickness of sediments (up to 500 m) in the deeper basin). The Inner Tertiary (ITH : Figure 12m) unconformity (14 Ma) eroded most parts of Unit T1 on the upper shelf linked to uplift (Figure 12l : Kuhlmann et al., 2010). The Cenozoic depocentre in both units has shifted from the northern end of the outer margin to at least three isolated areas in the outer margin. The base of T1 indicates the regressional phase and a hiatus from the Maastrichtian to late Palaeocene which causes the depocentres to shift to the deeper parts of the basin (Dingle et al., 1983).

There is a 10-fold decrease in sedimentation rate from the Cretaceous to Cenozoic (Table 1). There are many reasons for this. Dingle and Hendey (1984) proposed that the location of the Orange River Mouth during the Cretaceous –Palaeogene transition moved further south and

then shifted back Palaeogene - Neogene. Not only the shifts in the location of the river mouth can lead to the drop in sedimentation. De Wit et al., (2000) proposed that spatial changes in the drainage net of southern Africa is also controlled by landscape denudation and continental uplift. This is consistent with work by Dingle et al., (1983), Tinker et al., (2008) and Kuhlmann et al., (2010) that imply there was a rapid decrease in siliciclastic deposits linked to a decrease in terrigenous input and the cessation of differential crustal subsidence during the Cenozoic. This is also coincident with when the climate at the end of the Cretaceous experienced onset of cooling on a global scale (de Wit et al., 2000; Ruddiman 2010) and increased desiccation since Eocene (Tankard and Rogers 1989). Furthermore, thermal modelling based on new apatite fission-track analysis across the Great Escarpment of the west coast of southern Africa passive margin confirms that greater tectonic activity occurred when high elevation topography formed during the Cretaceous than in the Cenozoic (Kounov et al., 2009). Thus there is general agreement based on a variety of data that Cenozoic denudation and erosion rates were considerably lower than in the Cretaceous. In summary, the Cretaceous mega-sequence took place during periods of high sedimentation linked to high discharge rates of the Orange River and rapid crustal subsidence (Dingle et al., 1983; Tinker et al., 2008; Kuhlmann et al., 2010). The Cenozoic mega-sequence took place at periods of low sedimentation rates (Dingle et al., 1983; Dingle and Hendey., 1984; de Wit et al., 2000; Kuhlmann et al., 2010), although sedimentation rates have increased again slightly since the Miocene (Table 1).

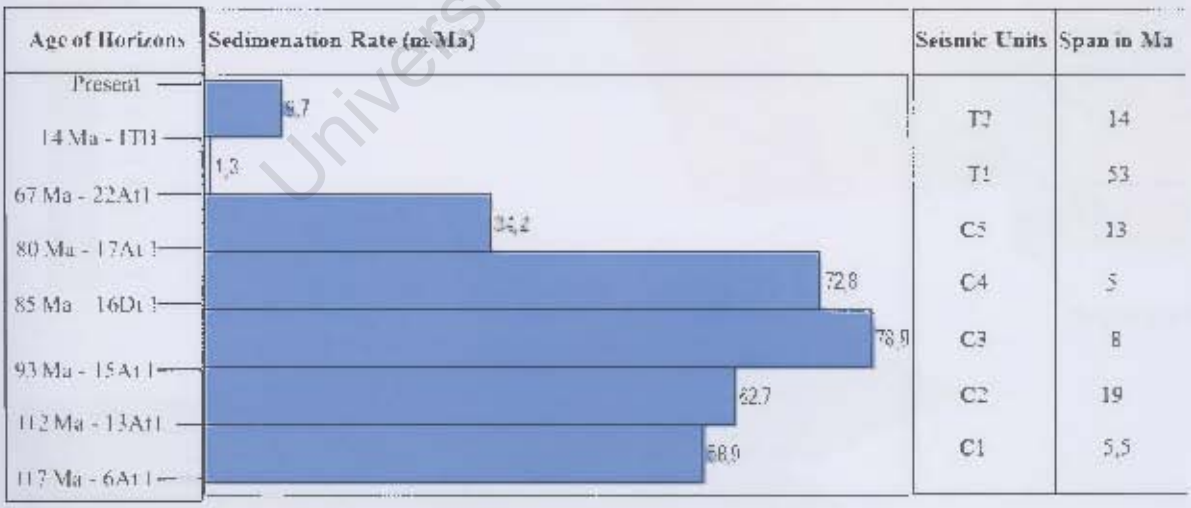

Table 1: Calculated sedimentation rates (in meters per million year m/Ma) at specific times on the different seismic units. ITH = Inner Tertiary Horizon. The table shows a near 10-fold decrease in sedimentation rate between Cretaceous to Cenozoic, followed by an increase from 1.3 m/Ma to 9.7 m/Ma around 14 Ma.

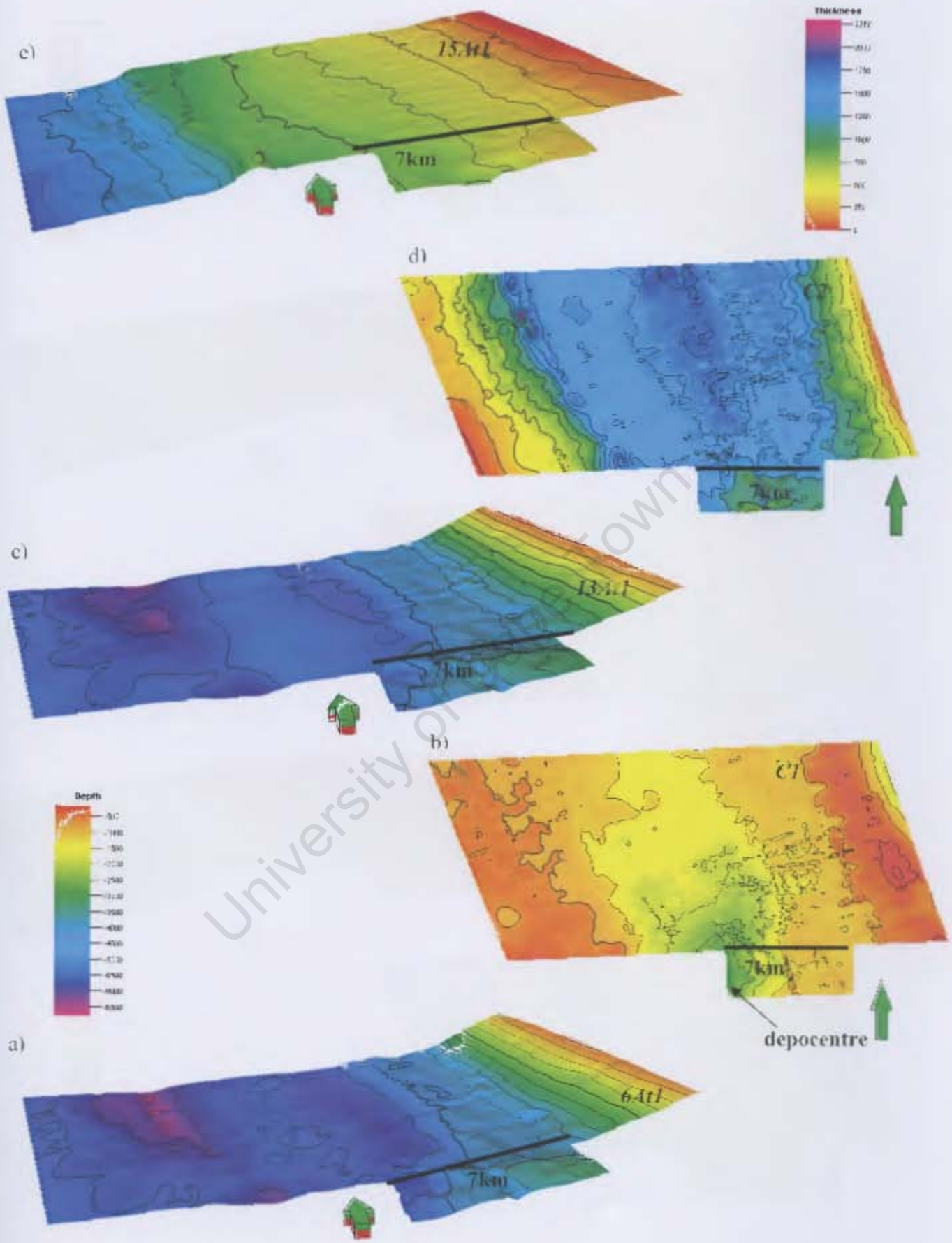

Figure 12 a-e: Cretaceous 3D depth surface maps (a,c,e) and corresponding thickness maps (d,b) of exploration Block 2. The arrows point to the North.

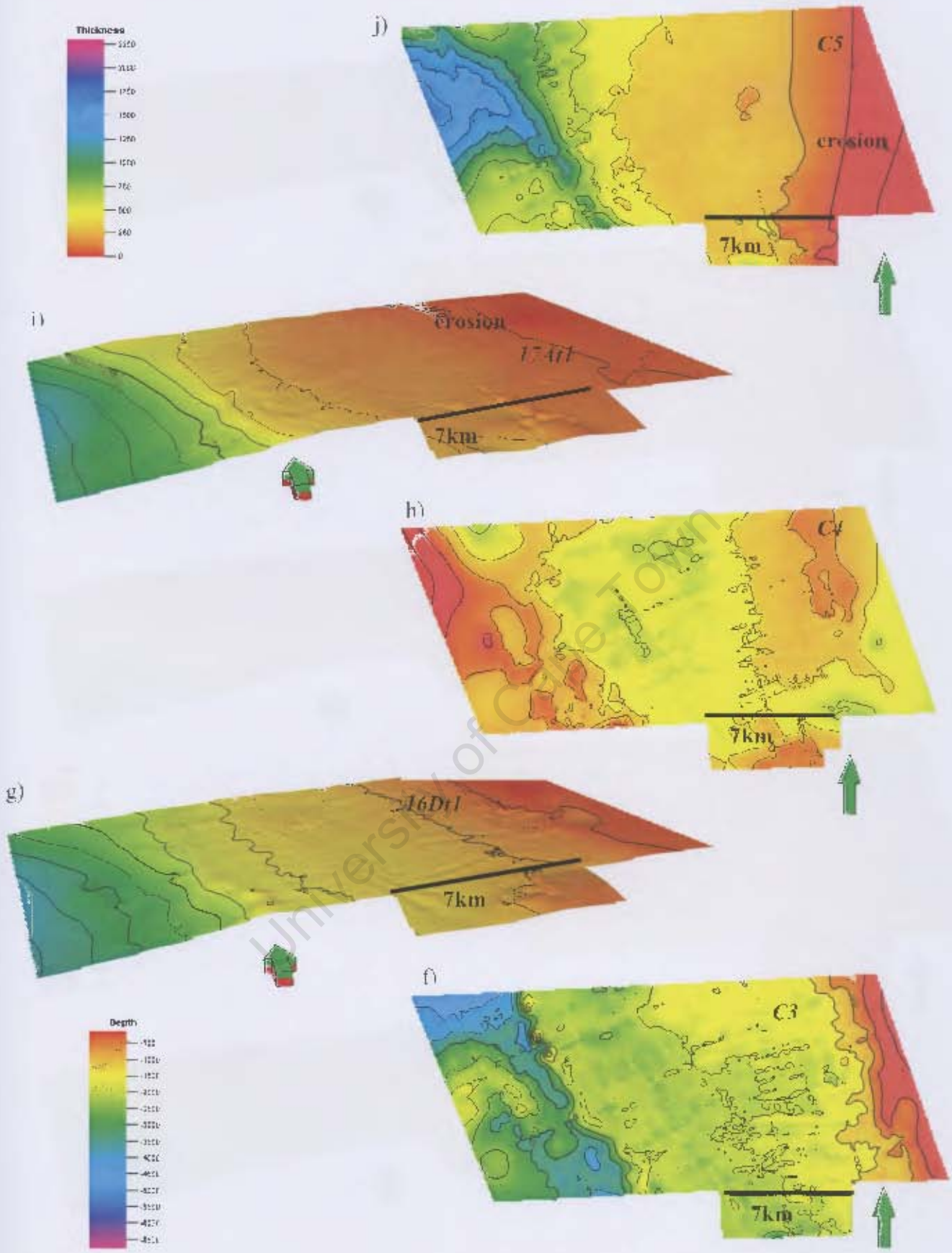

Figure 12 f-j: Cretaceous 3D depth surface maps (i,g) and corresponding thickness maps (j,h,f) of exploration Block 2. The erosional unconformities (red surface) are the responses to waves, winds, storms and relative sea level rise. The unconformities in the seismic profile indicate erosion of underlying seismic units. The arrows point to the North.

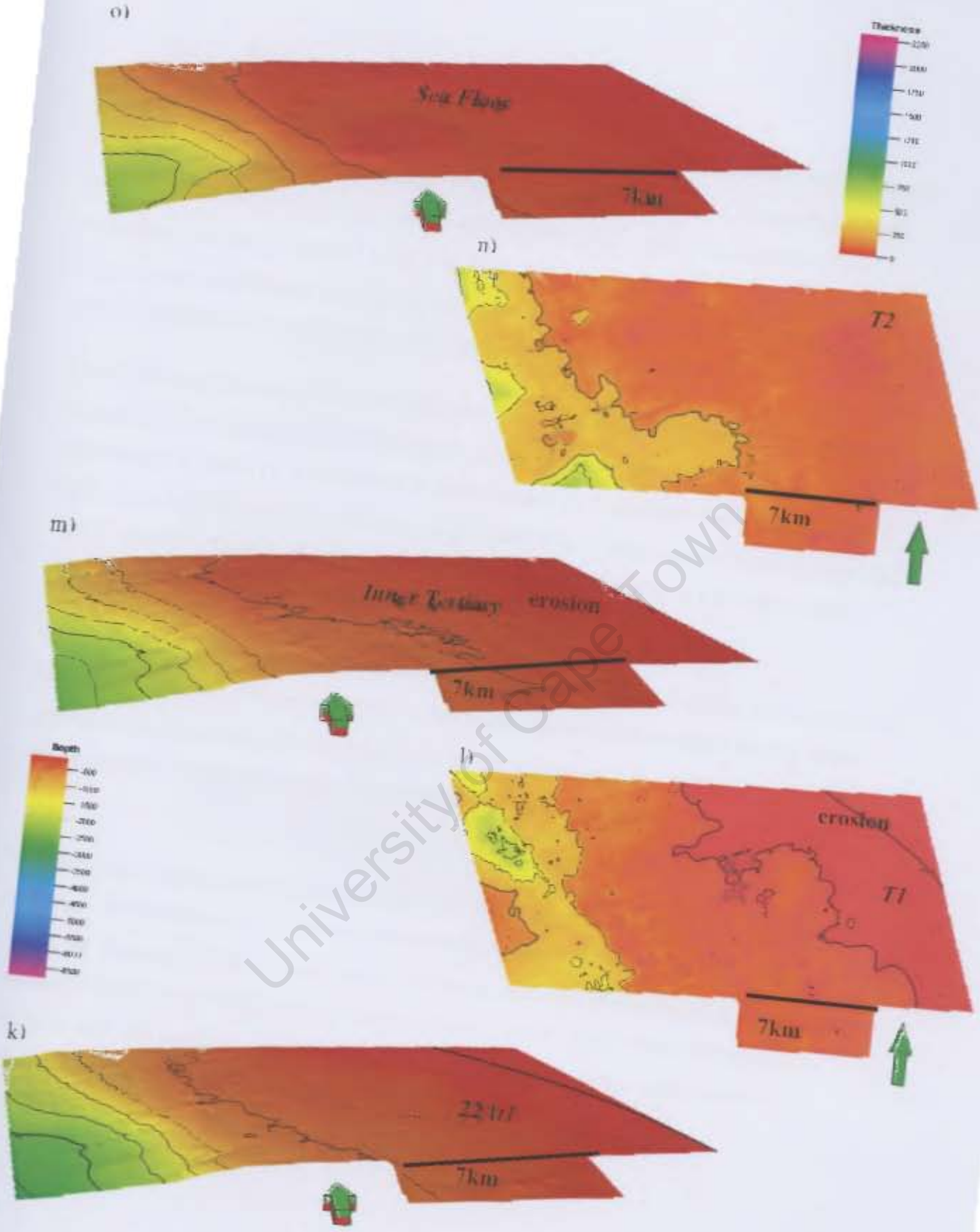

Figure 12 k-o: Tertiary 3D depth surface maps (o,m,k) and corresponding thickness maps (n,l) of exploration Block 2. The horizon, 'Inner Tertiary' (Cenozoic) (Weigelt and Unzelmann-Neben., 2004) s a 14 Ma horizon (Neogene) that separates T1 from T2. The arrows point to the North.

3.1.3 Main structural elements of the Orange Basin

The main tectonic regimes observed across the Atlantic in the continental margin of South Africa are (1) an extensional domain flanking the inner margin and (2) a compressional domain on the outer margin and deeper parts of the basin, each other separated by a transitional domain (Figures 11 and 13). Most of the major faults that were traced along the outer margin cut through the upper Cretaceous (C3-5) and Cenozoic (T1-2) units, and result from gravitational tectonics along the slope area region (e.g. Brown 1993).

The extensional domain, which strongly affects most of the Late Cretaceous onwards, is located in the present-day shelf-break/upper slope between 500 to 1500 m of present-day bathymetry (Figure 11). This domain is characterised by basinward dipping listric normal faults rooted at the base of the Cretaceous C3 unit, in the Cenomanian–Turonian layer (the 15At1 reflector; 93 Ma), which acted as a décollement layer (Séranne & Anka., 2005; Kuhlmann et al., 2010).

The compressional domain is located on the lower slope, downdip from the above described extensional domain. It is characterized by landward dipping asymmetrical thrusts, which apparently accommodate the deformation in up-dip extension domain (Figure 11 and 13). The thrusts are also rooted in the same Cenomanian –Turonian layer at the 15At1 reflector (Figure 13).

Determining factors for the occurrence and style of the gravitational tectonics along the margin may be linked to an increase in sedimentation rates and margin tilting (Tinker et al., 2008, de Vera et al., 2010). It also appears that three episodes of gravitational slumping are related to episodes of sea-level fall (Kuhlmann et al., 2010). In the following section, I analyse how this partition of structural styles may play a role on the distribution of hydrocarbon seepage features in the basin.

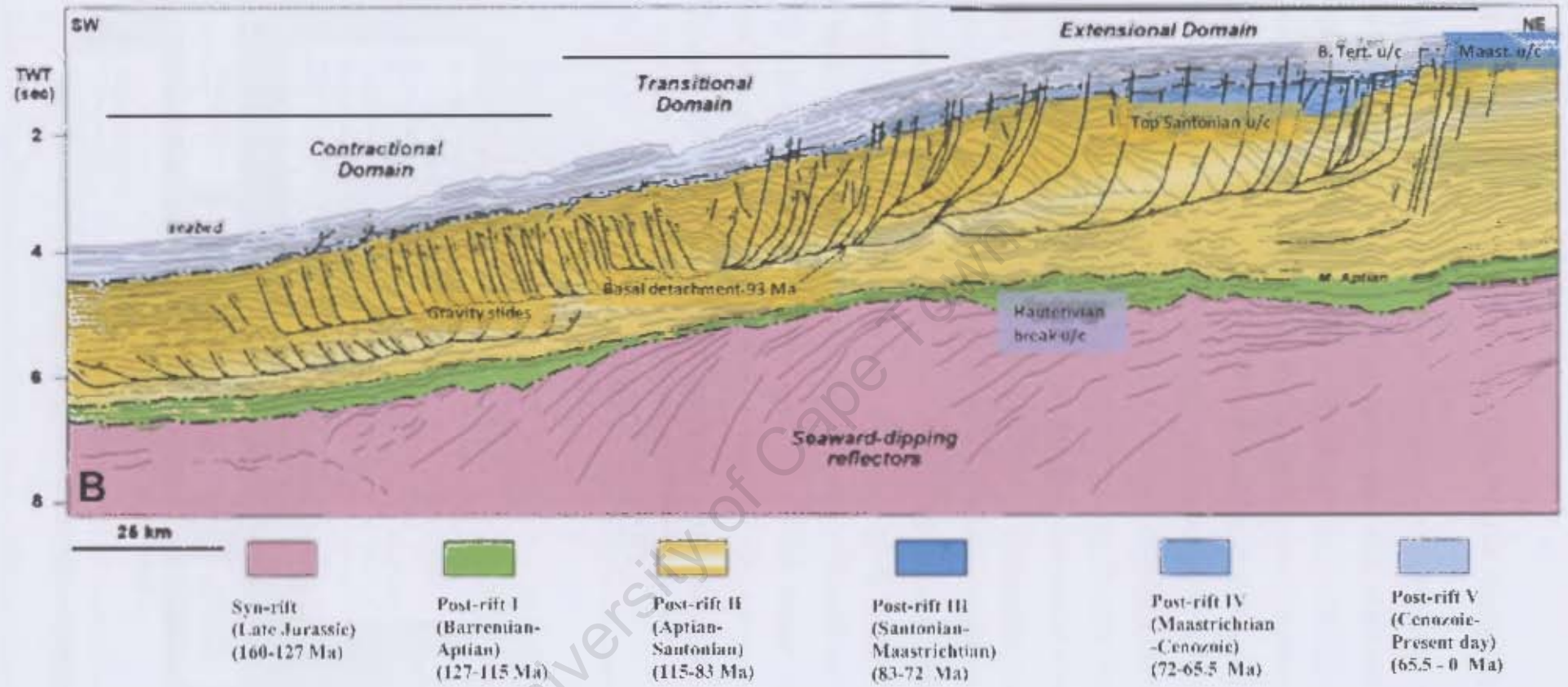

Figure 13- Regional seismic transect across the Orange Basin offshore southern Namibia showing the main depositional mega-sequences and the late Cretaceous gravity-driven slide system. This example shows both the extensional domain and compression domain with a toe thrust system. U/c stands for unconformity (from De Vera et al., 2010).

3.2 Identification, classification and distribution of chimneys

A great deal of features associated with past or active natural hydrocarbon leakage were identified within the study area. These features are both on the seafloor, as pockmarks or mounds, and within the stratigraphic column, as seismic chimneys or buried pockmarks. Additionally, several seismic anomalies characteristic of gas presence (i.e. bright and flat spots, seismic blanking) were identified. Depending on their controlling factors, the chimneys are classified into two main categories: (1) stratigraphically-controlled (sa-c) and (2) structurally-controlled (s-c) (Figure 14). The most prominent gas chimneys were mapped (113 : Figure 15a-b) and Appendix 1 summarises their classification, location (bathymetry), and dimensions. The ratio of s-c versus s-ac chimneys is estimated close to 2:5 (70% of anomalies from Appendix 1 are sa-c), which suggest a strong stratigraphic control on natural gas leakage in the basin. The chimneys either leak up to the seafloor terminating as pockmarks ("active leakage") or are sealed within the Miocene (14 Ma) sequence, where they terminate in paleo-pockmarks. Burial of the gas chimneys was due to burial during slumping caused by the onset of the Benguela Current around the Middle Miocene (Weigelt and Ünzelmann-Neben., 2004) .This current was responsible for the major depositional changes such as slumping, submarine erosions, and contourite deposits along the western part of the African margin (Séranne and Abeigne, 1999; Weigelt and Ünzelmann-Neben., 2004; Séranne and Anka., 2005).

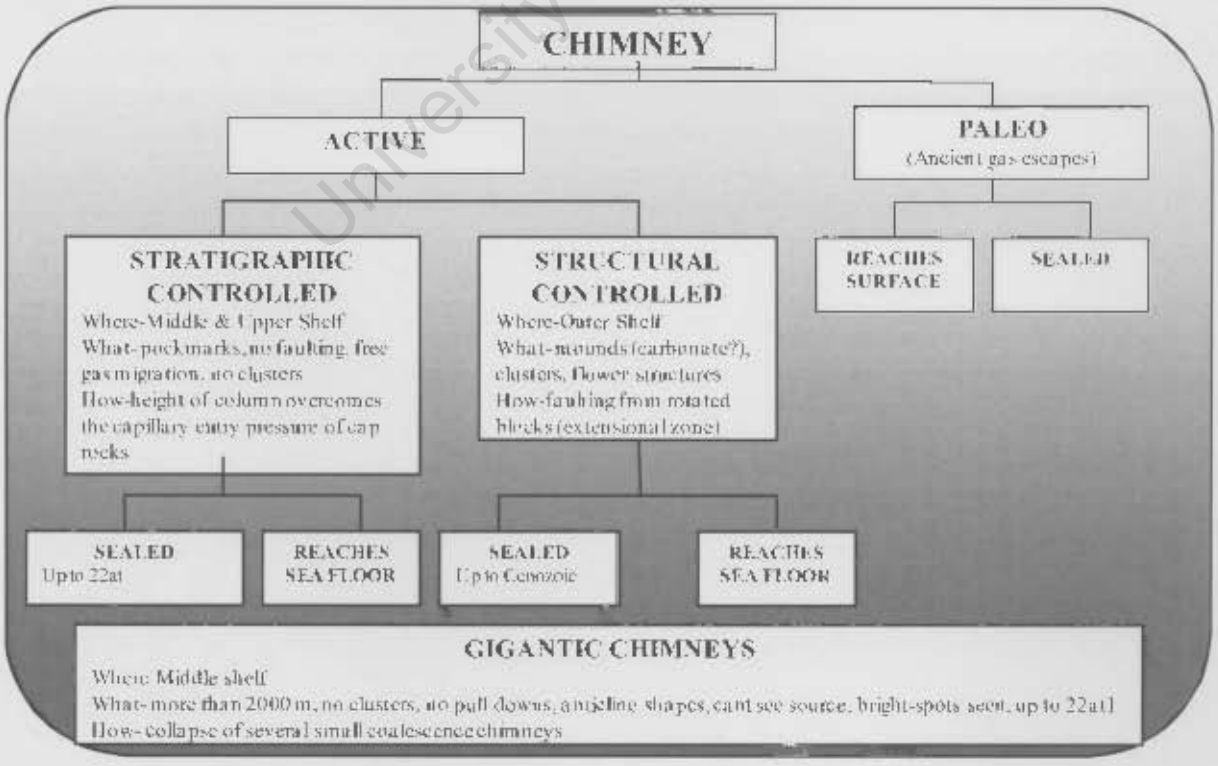

Figure 14: Classification chart used to identify the gas chimneys in this study.

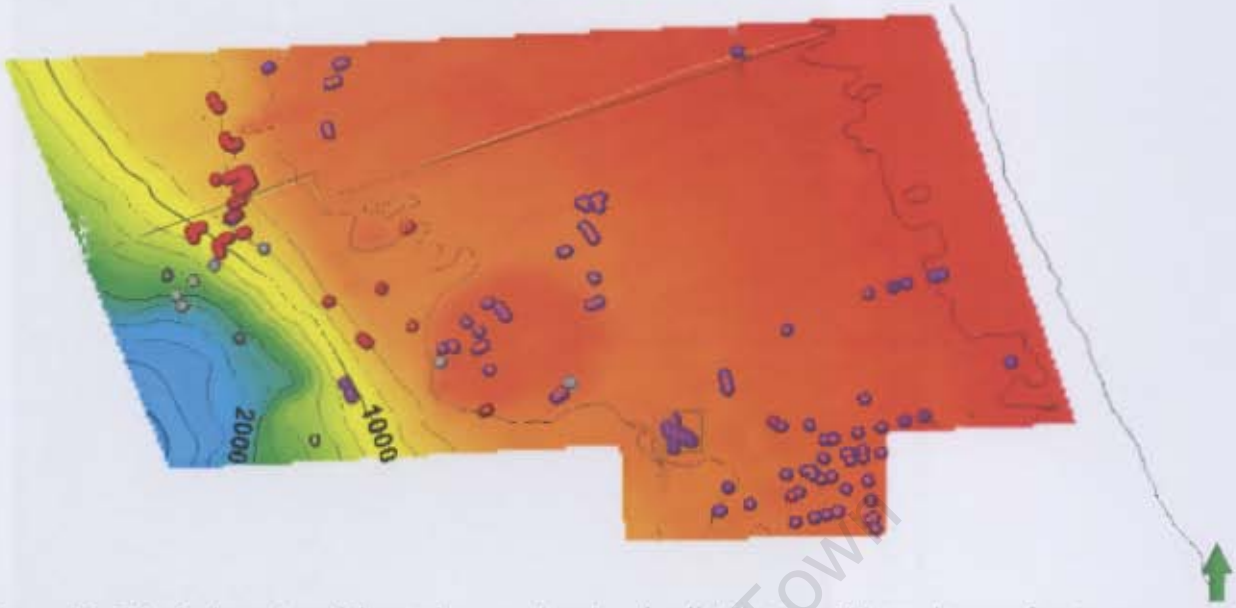

Figure 15a: The bathymetry of the study area, showing the distribution of three classes of major gas chimneys identified in this study: (purple) stratigraphic controlled chimneys, (red) structural controlled chimneys and (grey) paleo chimneys. Note that the structurally-controlled chimneys are confined to the deep basin and steepest slopes, while the stratigraphically-controlled chimneys dominate the middle and upper shelf. The location of a giant collapsed chimney is marked by a black square. (The composite regional seismic section depicted in Figure 11 is shown as a bold black line).

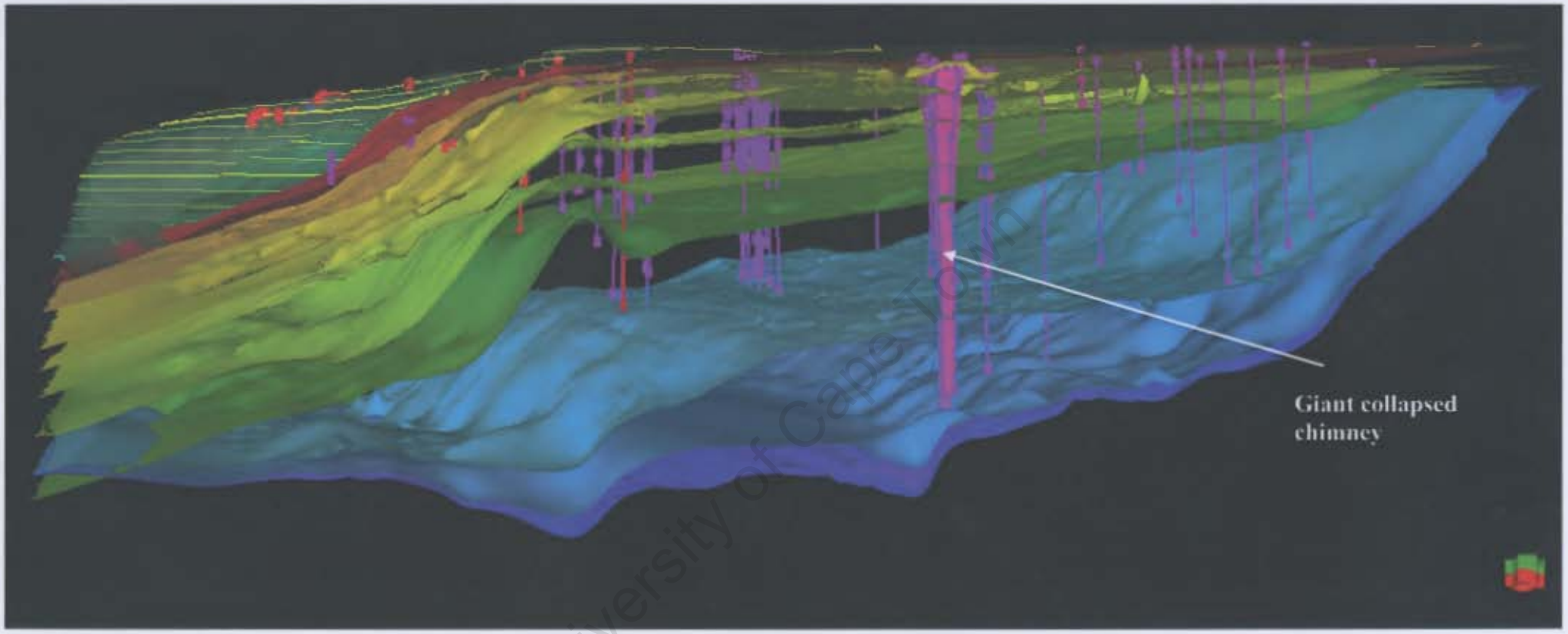

Figure 15b: 3D view showing the progradation of the continental margin since Albian (14At1). Note that the structurally-controlled chimneys (red) are confined to the extensional domain of the slope, whilst the stratigraphically-controlled chimneys (purple) are confined to the middle and upper shelf (from Petrel software). The arrow points to the North.

3.2.1. Structurally-controlled gas chimneys

The structurally-controlled (s-c) chimneys are all located on the extensional domain and appear to originate upwards of the listric normal faults (Figure 15a-b and 16). To the best of my knowledge, the existence of these s-c gas leakage features in the deeper parts of the basin, where present-day active hydrocarbon generation may be present, has not been reported before.

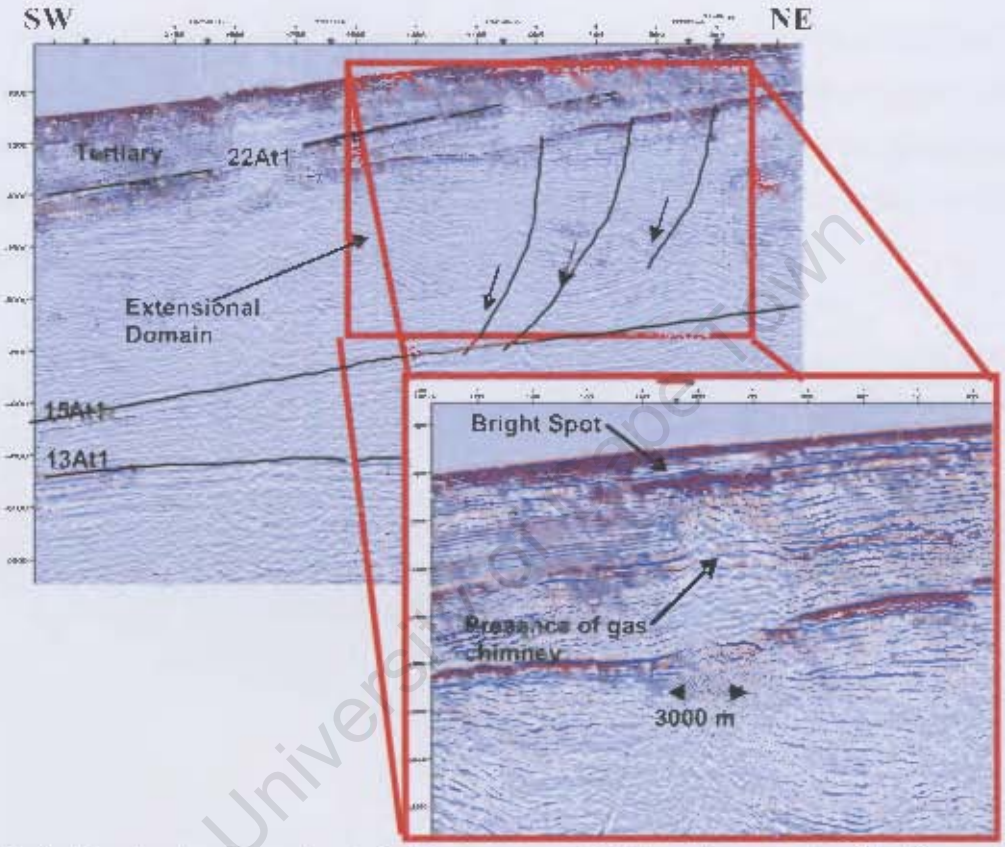

Figure 16: Active structurally-controlled chimney mapped in the outer margin of the Orange Basin. The chimney is sealed at about 0.1 sec (TWT) below the sea surface, below a flat seismic anomaly indicative of free gas (For location, see Figure 9).

S-c chimneys are found within anticline-crests in the hanging wall of normal faults (Figure 16), as mounds and extensional-fault clusters. The faults commonly converge at depth within a major SW dipping normal fault (Viola et al., 2005; see Figure 17).

About half of the s-c chimneys are sealed within the Miocene sequence, below the Inner Tertiary horizon (Figure 17). When the chimneys were buried, this has shut off the gas leaking to the atmosphere. This means a decrease in rates of methane leakage at that time, which in turn then contributes less to the Earth's greenhouse gas budget in the atmosphere.

This may even may have contributed to the Neogene global cooling, if this event integrated over the entire South African continental margin. but better quantification is needed to verify this (e.g. Ruddiman 2010).

Those chimneys that reach the sea floor terminate either in pockmarks or in seafloor mounds. These latter have up to 1500 m in diameter and heights between 10-50 m (Figure 17). Ben-Avraham et al., (2002) have also mapped these seafloor mounds and reported evidence of BSR. During this study, no BSR was detected. This study indicates that s-c chimneys are linked to extensional faults and roll over anticlines within the extensional zone (Figure 17), which suggests that these chimneys have been triggered by gravitational collapse. This observation also allows the identification of the source rock from which the gases migrated as the gases that migrate up-dip the faults are fed by source rocks of Cenomanian/Turonian age. This aspect will be discussed in more detail the following chapter.

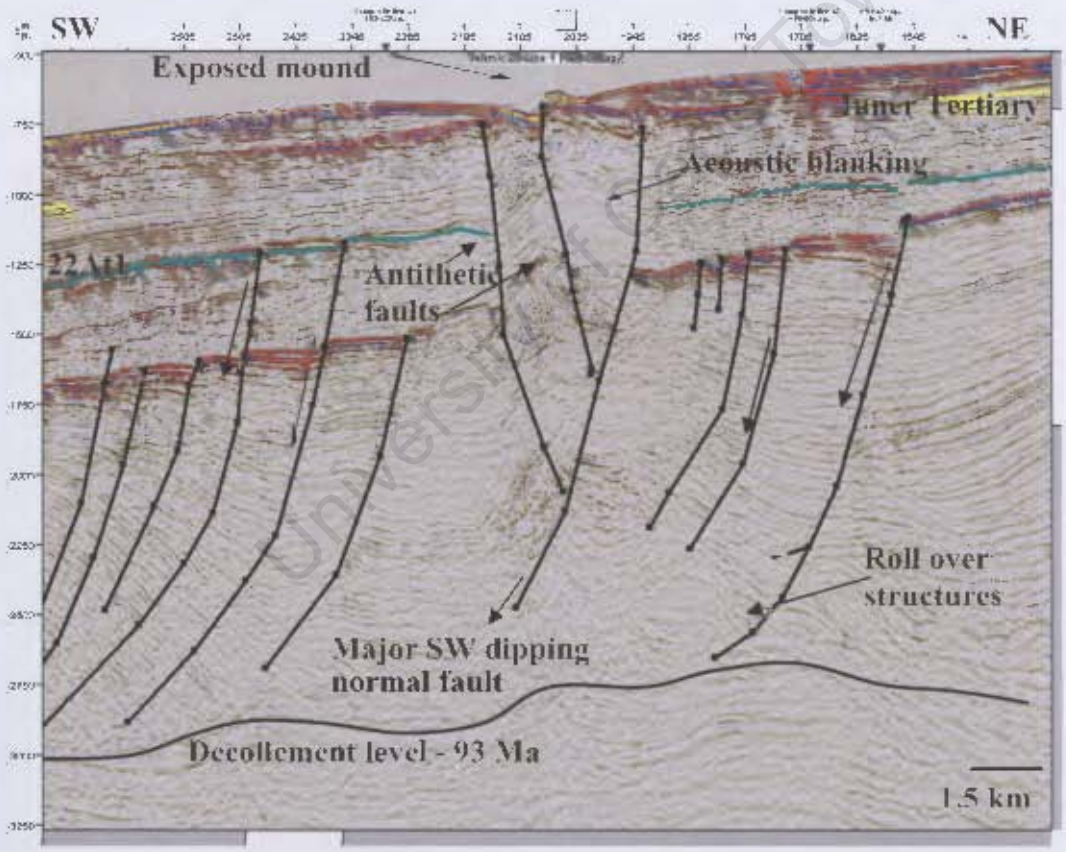

Figure 17: View of a structurally-controlled chimney located above anticline-crestal faulting that terminates in a seafloor mound. The gases migrate up the faults to the exposed mound formed from emission of argillaceous material. Two NE dipping conjugate faults converge at depth within a major SW dipping normal fault (black bold lines). The faults are indicated with arrows. Note that the chimney has antithetic faults and the roll-over structures that merge in the decollement zone (For location, see Figure 9).

3.2.2. Stratigraphically-controlled gas chimneys

Earlier studies in Blocks 3 and 4 (Figure 1) of the Orange Basin revealed the presence of stratigraphically-controlled (sa-c) gas chimneys on the shelf and upper slope, in water depths up to 500m (Kuhlmann et al., 2010). This study shows that in Block 2, the sa-c chimneys are mostly located on the middle and upper shelf in water depths up to 500m (Figure 15a-b). The gaseous hydrocarbons appear to migrate "freely" through the sedimentary column, suggesting that the height of the gas column overcomes the capillary pressure of cap rocks (e.g. Kaluza & Doyle., 1996). The chimneys appear to be mostly related to the presence of stratigraphic onlaps and pinch-outs within the Aptian sequence, displaying no relationship to the surrounding faults or structural elements (Figure 18). It seems that the seal rock is broken at these stratigraphic features that appear to facilitate the upward gas migration. When the gases are expelled at the seafloor, they create pockmarks (between 100-400 m in diameter). Elsewhere they are trapped within the sediments close to the sea floor and are detected as seismic bright spots (Figure 18).

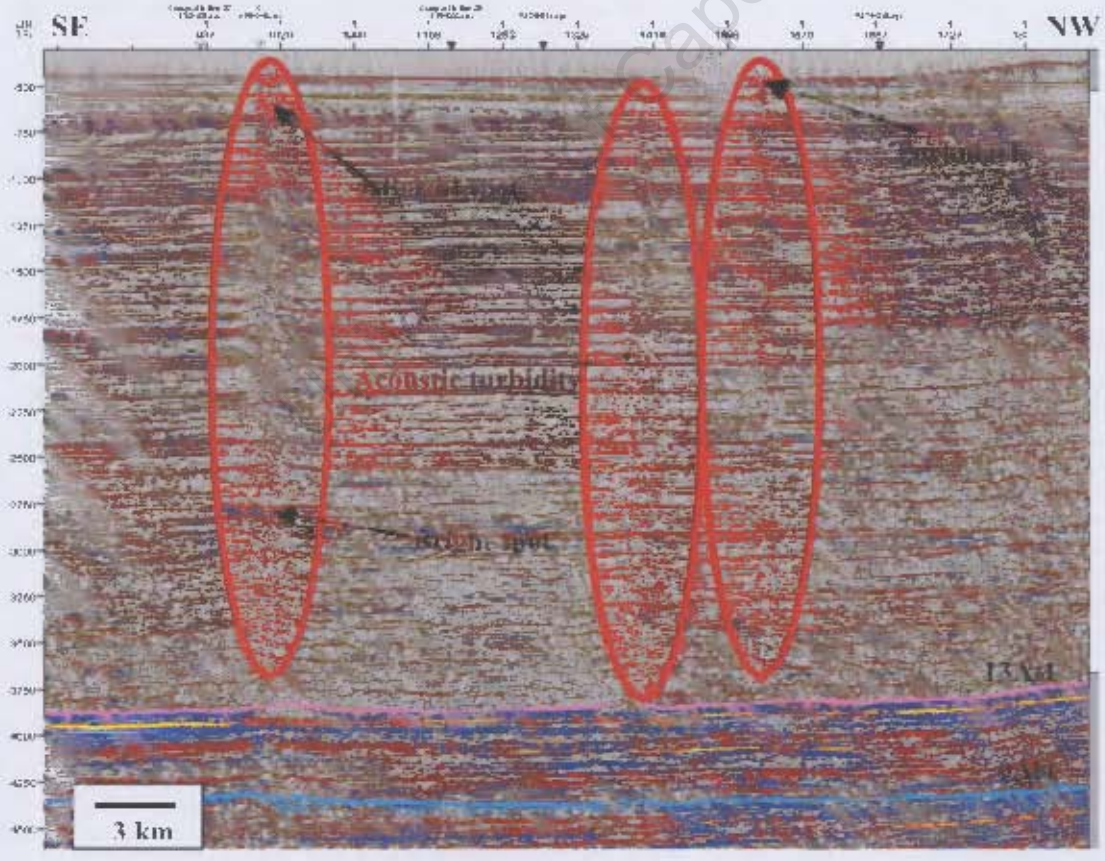

Figure 18: Active stratigraphically-controlled chimneys along the middle margin of the Orange Basin. Note how free gases migrate through the sedimentary column from the Aptian layer (13At1) and the

lack of faulting. The bright spots indicate the presence of hydrocarbons trapped close to the surface. The pockmarks are about 300 m wide (For location, see Figure 9).

3.2.3. "Giant" gas chimneys

An interesting finding is at least three "giant" chimneys located beneath the middle shelf (Figure 15a-b : Appendix 1). Figure 19 shows one of these "giants" with an upper diameter of 7 km. Even though some bright spots indicative of gas presence have been identified flanking these features, there is no evidence of acoustic turbidity or seismic pull-downs within the chimney tube, indicating that there is no present-day active gas leakage, and that the "giant chimneys" are actually inactive or paleo-gas leakage structures. Clear indications of internal gravitational collapse are identified within the chimney, suggesting that this chimney resulted from the collapse of smaller coalescent chimneys. Figure 21a shows a close-up detailed view of near-surface collapsed crater and Figure 20b demonstrates a schematic evolution for these large features.

It is not clear whether these large chimneys are stratigraphically-controlled (Sa-c) or if they are linked to deep faulting because the seismic record does not penetrate deep enough. These chimneys have pseudo-conical shapes, with near surface diameters up to 7.5 km and lower stems of about 2 km. They are sealed within the Miocene section (14 Ma), beneath the "Inner Tertiary" horizon and do not reach the seafloor. The gas leakages probably stopped during the Miocene perhaps when the onset Benguela Current caused the slumping (Weigelt and Ünzelmann-Neben 2004), possibly rapidly burying the vents. Related reduction in the methane leakages from these giant chimneys may have contributed to a sudden global cooling 'jerg' at ca. 12 Ma but more information is needed to verify this (Westerhold et al., 2005 and Ruddiman 2010).

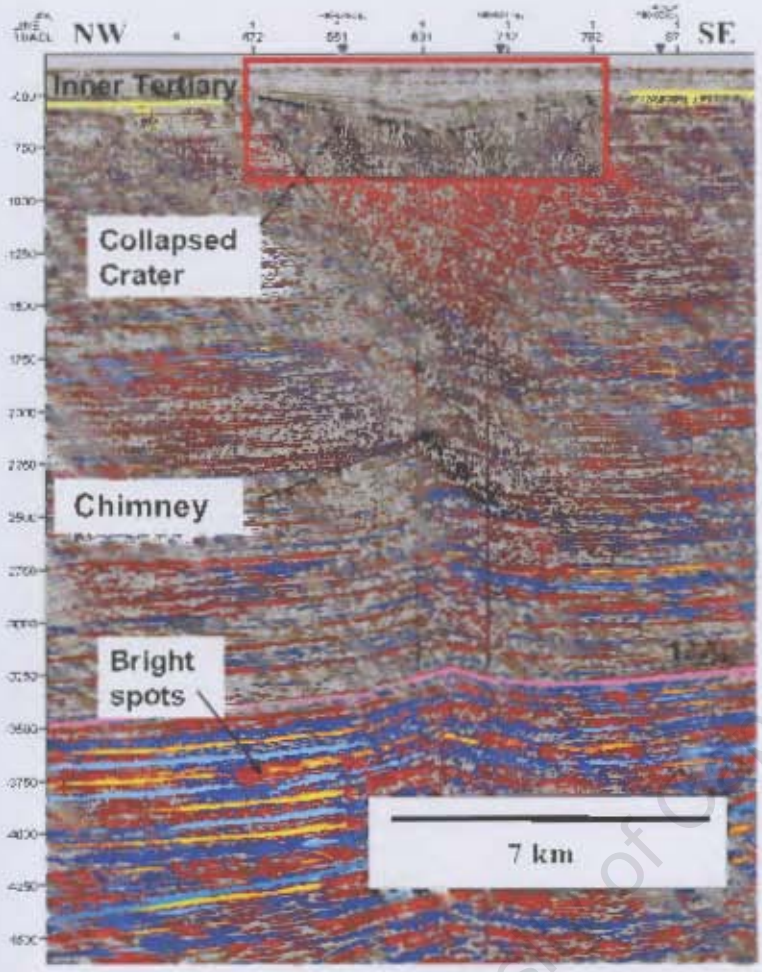

Figure 19: Giant chimney terminating in a collapse crater of more than 7 km in diameter. Note the lateral bright spots in the lower sections of the chimney and the absence of internal seismic "pull-downs". The red square represents the detailed view of near-surface collapsed crater shown in Figure 20. For location, see Figure 9.

a)

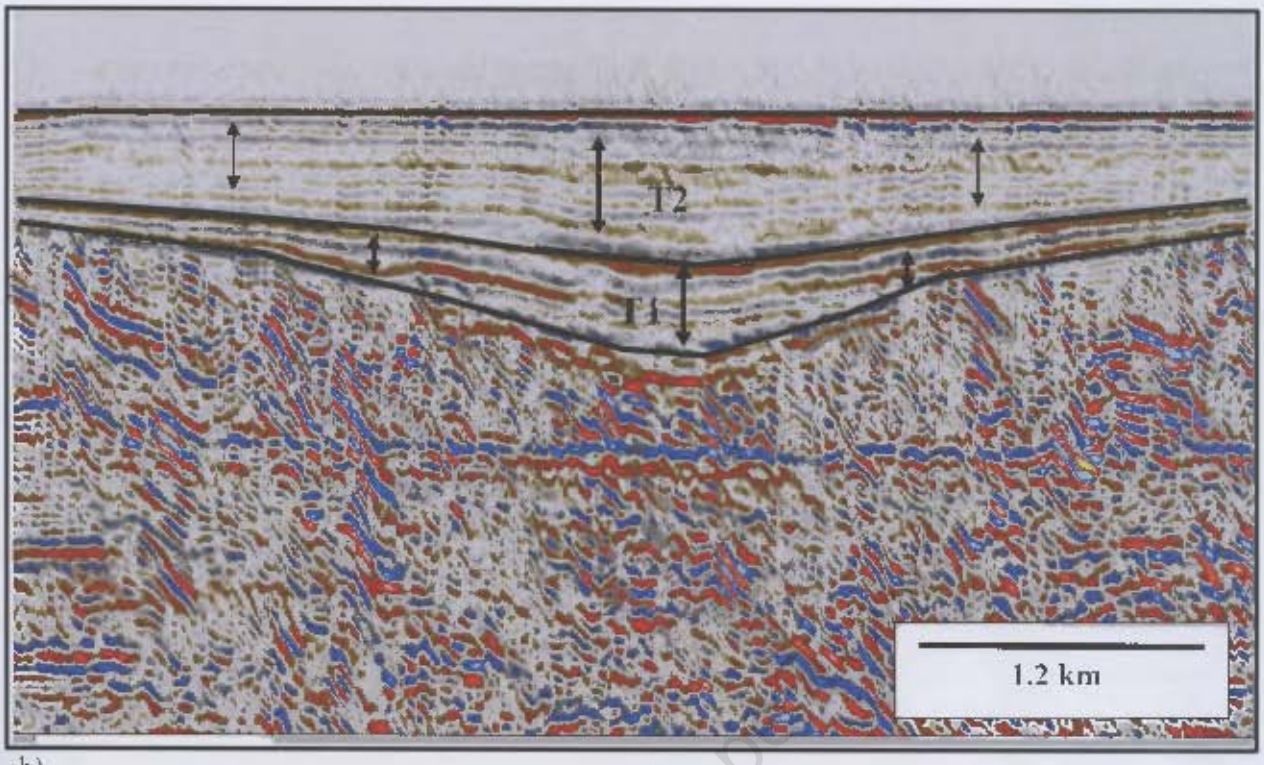

b)

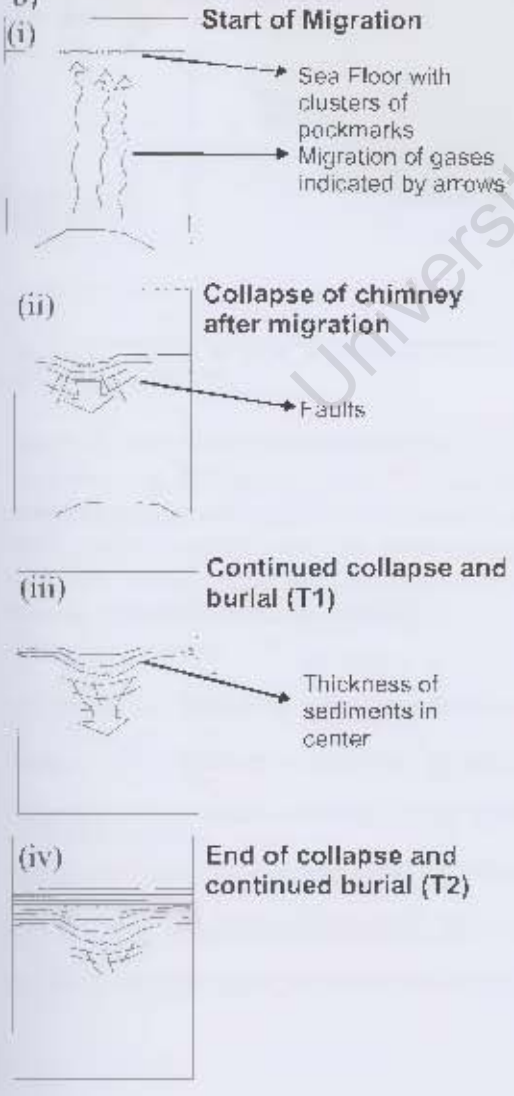

Figure 20: a) Detailed view of a near-surface collapsed crater. b) Schematic interpretation of collapse (i) The cluster of pockmarks are created by the gases leaking to the surfaces. (ii) Gas migration and onset of chimney formation during collapse. (iii) The crater is buried by overlying sediments (T1). The thickness variations of T1 indicate that the sediments were deposited during the chimney collapse. (iv) Deposition of sediments (T2) overlying T1, starting at 14 Ma, marks the end of the collapse. T2 has uniform thickness.

3.3. Basin modelling of composite seismic line

3.3.1 Input

The composite seismic line produced during the first part of the study (Figure 11) was depth converted (Figure 21) to enable 2-D petroleum system modelling. This was done by transforming interpreted TWT horizons to a scale of depth using the checkshots (time-depth pairs) from the boreholes. The depth-converted transect is ~220 km long and ~11 km deep.

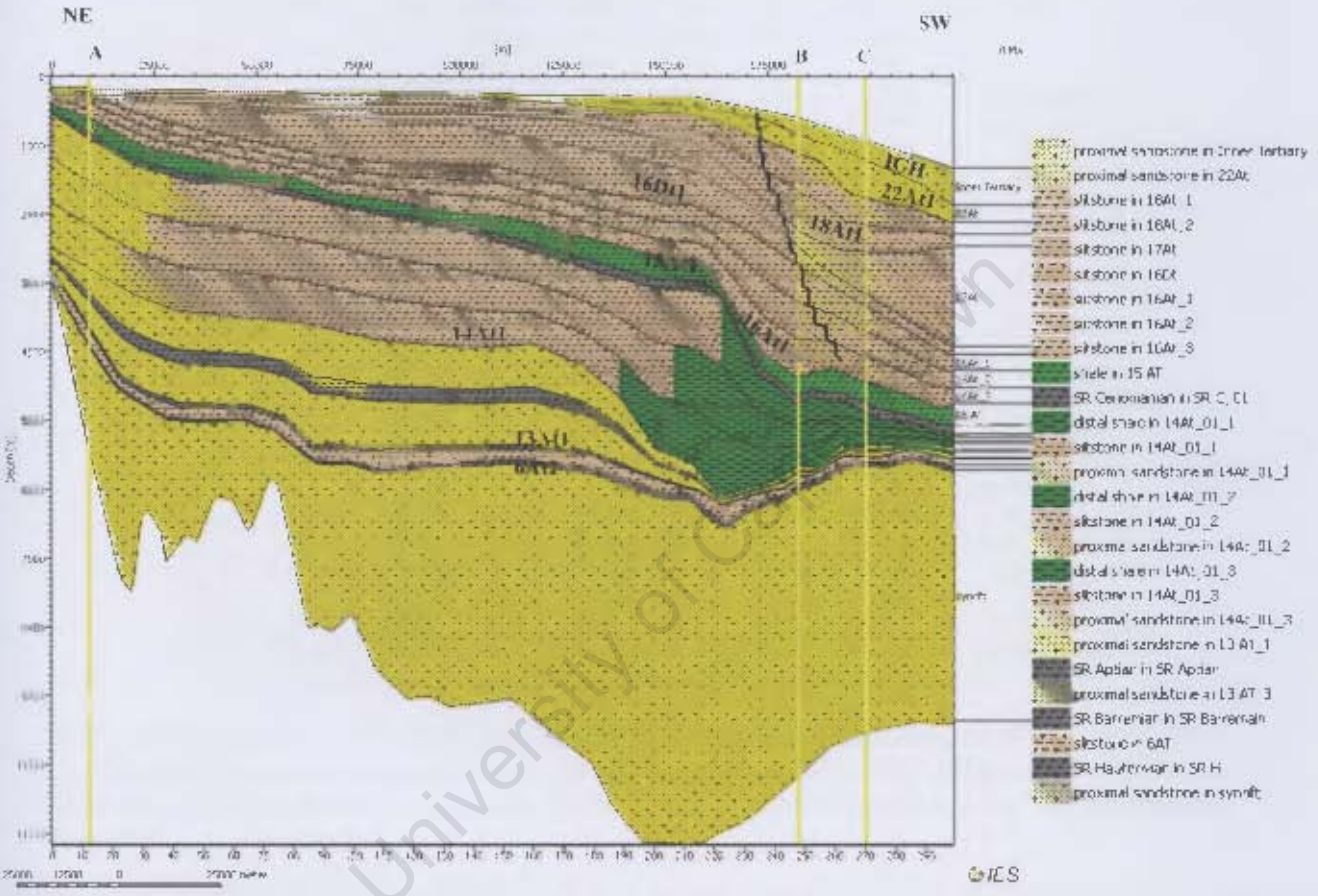

Figure 21: Depth converted model produced by the composite seismic line (see Figure 11) with facies definition (e.g. Kuhlmann et al., 2010) for each unit. Source rocks are shown in grey (see legend). In addition, a SE trending fault (bold black zigzag line) is displayed and the three depth extractions from wells (yellow vertical lines) are shown at the proximal (A), middle (B) and distal locations (C) of the basin at 9,320m, 182,230m, and 198,662 m distances, respectively. Legend names cannot be corrected because the software is not available.

In a first step, horizons were digitized in Petromod using a bitmap of the depth converted transect. The horizons were then gridded using a constant grid spacing of 735 m. In this manner, a first series of events were defined (period of deposition between two horizons) and further refined by including periods of erosion in the age definition table (Table 2). The events were assigned sedimentary facies that include the definition of lithology and, where required, source rock properties (Table 3; Figure 22). Different lithologic properties were

assigned to the individual sequences according to the chronostratigraphic and sequence charts for the Orange Basin (Figure 3). Table 3 shows TOC and HI values of the source rocks, as well as the reaction parameters input values (expressed as kinetics) used for basin modelling. Source rock properties HI and TOC were taken from the literature (Table 4 : Bray et al., 1998; Muntingh 1993; Jungslager 1999; Ben-Avraham et al., 2002; Van der Spuy 2003; Paton et al., 2007 and 2008; Kuhlmann et al., 2010).

	1	2	3	4	5	6	7	8
	Name	Color	Deposition Age from [Ma]	Deposition Age to [Ma]	Erosion Age from [Ma]	Erosion Age to [Ma]	Max. Time Step Duration [Ma]	Facies 1
21	Inner Tertiary		14.0000	0.0000	0.0000	3.0300	10.0000	proximal sandstone
20	22At		55.0000	20.0000	20.0000	14.0000	10.0000	proximal sandstone
19	18At_1		75.2500	75.3000	65.0000	62.0000	10.0030	siltstone
18	18At_2		77.5000	76.2500	62.0000	59.0000	10.0000	siltstone
17	17At		83.0300	77.5000	59.0000	57.0000	10.0000	siltstone
16	16Dt		85.0000	80.3000	57.3000	55.0000	10.0000	siltstone
15	16At_1		86.6670	85.0905	0.0000	3.0300	10.0030	siltstone
14	16At_2		88.3330	86.6670	0.0300	3.0300	10.0000	siltstone
13	16At_3		90.0000	88.3335	0.0000	3.0000	10.0000	siltstone
12	15 AT		92.5500	90.0000	0.0000	3.0000	10.0000	shale
11	SR C_01		93.0000	92.5500	0.0300	3.0000	10.0000	SR Cenomanian
10	14At_01_1		96.3340	93.0010	0.0000	3.0000	10.0030	proximal sandstone
9	14At_01_2		99.6670	96.3340	0.0000	0.0030	10.0000	proximal sandstone
8	14At_01_3		103.0000	99.6670	3.0000	0.0030	10.0030	proximal sandstone
7	13AT_1		105.5436	103.0000	0.0300	3.0000	10.0000	proximal sandstone
6	SR Aptian		105.4414	105.5436	0.0000	3.0000	10.0000	SR Aptian
5	13AT_3		108.9350	108.4414	3.0000	3.0300	10.0000	proximal sandstone
4	SR Barremian		112.0000	108.9350	3.0000	0.0000	10.0000	SR Barremian
3	6At		117.5000	112.0000	0.0000	3.0000	10.0000	siltstone
2	SR H		119.0000	117.5000	3.0000	3.0300	10.0000	SR Hauterivian
1	zpvht		121.0000	119.0000	3.0000	3.0300	10.0000	proximal sandstone

Table 2: Parameters used for modelling, e.g. the deposition age of each horizon (Brown et al., 1995), their erosion ages (Kuhlmann et al., 2010), as well as facies definitions (Kuhlmann et al., 2010) of the 2D model. The ages of each horizon were derived from the chronology table of the Orange Basin (see Figure 2).

	1	2	3	4	5	6	12	13	14
	Name	Petroleum System Elements	Color	Lithology Value	TOC Model	TOC Value [%]	Kinetics	HI Value [mgHC/gTOC]	HI Map [mgHC/gTOC]
1	proximal sandstone	Reservoir Rock		Sandstone (typical)	Uniform	0.00	none	0.00	none
2	SR Hauterivian	Source Rock		Shale (organic rich, typical)	Uniform	10.00	Pepper&Corvi(1995)_T1(C)	600.00	none
3	SR Barremian	Source Rock		Shale (organic rich, typical)	Uniform	3.00	Pepper&Corvi(1995)_T1IIH(DE)	180.00	none
4	SR Cenomanian	Source Rock		Shale (organic rich, typical)	Uniform	5.00	Pepper&Corvi(1995)_T1II(B)	300.00	none
5	siltstone	none		Shale (organic lean, silty)	Uniform	0.00	none	0.00	none
6	shale	none		Shale (typical)	Uniform	0.00	none	0.00	none
7	SR Aptian	Source Rock		Shale (organic rich, typical)	Uniform	3.00	Pepper&Corvi(1995)_T1-5(A)	180.00	none
8	distal shale	none		SHALE	Uniform	0.00	none	0.00	none
9	Silty shale	none		SHALE silt	Uniform	0.00	none	0.00	none

Table 3: Facies definition, kinetics and, HI and TOC values of each individual sequence.

Source rocks	TOC	HI mg HC/g	Thickness	Location	Observation	Previous Studies
Cenomanian - Turonian	Up to 5%	600	100m	PASA well A -K1	Terrestrial origin. wet gas prone More oil prone further offshore T II and III mixed	Ben-Avraham et al 2002 Bray et al 1998, Paton et al 2007 and 2008. Muntingh 1993 . Van der Spuy 2003
Marine Lower Aptian	26% (2%) (5%)	180-200	40m (40-50 m) (140m)	Kudu borehole in Namibian part of basin very proximal AA-1 and K-A2 in Block 2	Gas and oil source Type II	Ben-Avraham et al 2002, Bray et al 1998 . Jungslager 1999, Paton et al 2007 and 2008 Van der Spuy 2003
Transitional Barremian	25%	800	300m	South West of Cape Basin , DSDP 361	Oil to wet gas prone Type II	Ben-Avraham et al 2002, Jungslager 1999, Kuhlmann 2010, Paton et al 2007 and 2008, Van der Spuy 2003,
Syn rift lacustrine sapropelic black shales of Upper Hauterivian age	more than 10%	greater than 600mg	more than 60 (M)	In half graben s. South of Ibhubesi gas field, Soekor A -J1 well	oil prone Type 1	Barton et al 1993, Ben - Avraham et al 2002. Jungslager 1999. Kuhlmann 2010, Muntingh 1993 , Paton et al 2007 & 2008 ,

Table 4: TOC, HI, thickness, location of wells and observations of each source rocks according to different authors.

Kinetic parameters were used to describe the rate of reaction for conversion of kerogen to oil and gas assuming primary and secondary cracking reactions. Reaction parameters in this study were adopted from Pepper and Corvi (1995a, 1995b) and Pepper and Dodd (1995) and were assigned to the four rock source intervals from the oldest to the youngest, of the Hauterivian, Transitional Barremian, lower Aptian and Cenomanian/Turonian age, based on the source rock facies in kerogen Types I, II and III (Table 4).

The boundary conditions define the basic energetic conditions for reconstruction of the temperature and burial history of the study area. These boundary conditions are: PWD (Paleo Water Depth); SWIT (Surface Water Interface Temperature); and HF (Heat Flow) evolution through geologic time. The Petromod software offers an automatic tool to calculate and set the SWIT trend which displays a simplified graph of the sea floor temperature at each time step over the past 360 million years (Figure 23 ; Wygrala 1989).

The heat flow trend can be input manually by graphically editing a trend (Figure 24). The heat flow is based on that published by Paton et al., (2007) and the heat flow scenarios were

modelled following a McKenzie (1978) type lithospheric stretching model. The 'pure shear' Mckenzie model (1978) is a widely used stretching model in explaining the history of rift basin or passive margin subsidence. The model assumes a rapid (essentially instantaneous) fault-related synrift subsidence phase followed by a long-term thermal subsidence phase. Figure 24 shows a finite stretching around 125 Ma (rifting), followed by a slower thermal decay to 75 Ma, terminating with a constant heat flow of 60 mW/m^2 thereafter. Heat flow variability along the modelled section was not deemed significant. In my model, the rifting is initiated about 5 Ma after than the recently proposed rifting at 134-132 Ma suggested by Moulin et al's paper (2010). This difference does not affect the modelling results as the main period of maturation is related to the Cretaceous burial and not to the heat flow peak.

The PWD (Figure 25) evolution is defined assuming a linear interpolation through time, starting from 0 water depth at rift initiation to the present day water depth. This linear interpolation is the most parsimonious assumption in the absence of better data.

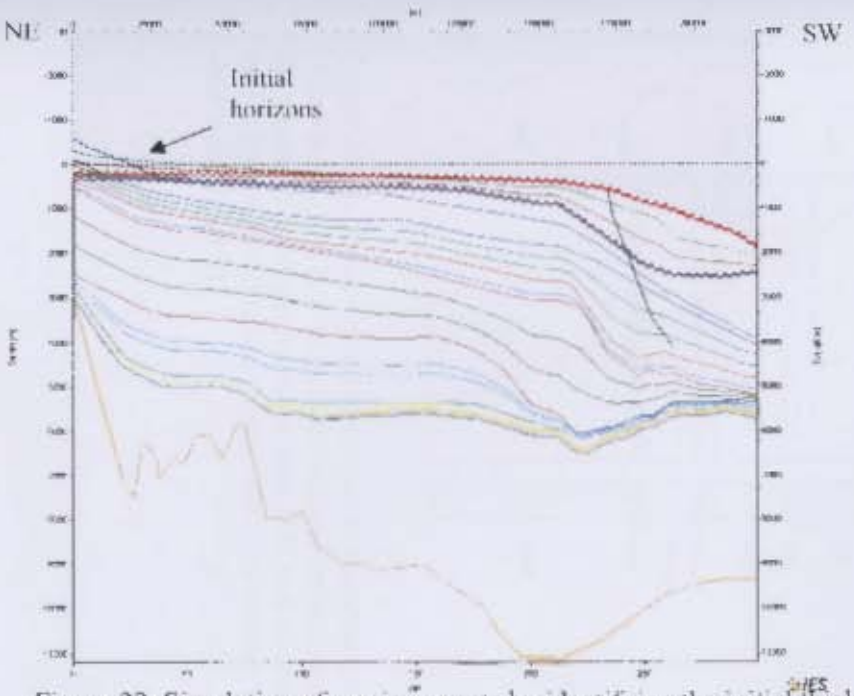

Figure 22: Simulation of erosion events by identifying the initial thickness of horizons before they were eroded, using Petromod (see text). The blue zigzag line marks the unconformity 18At (77.5 Ma) and the red zigzag line marks the Inner Tertiary Horizon (ITH-14Ma horizon, see Figure 2).

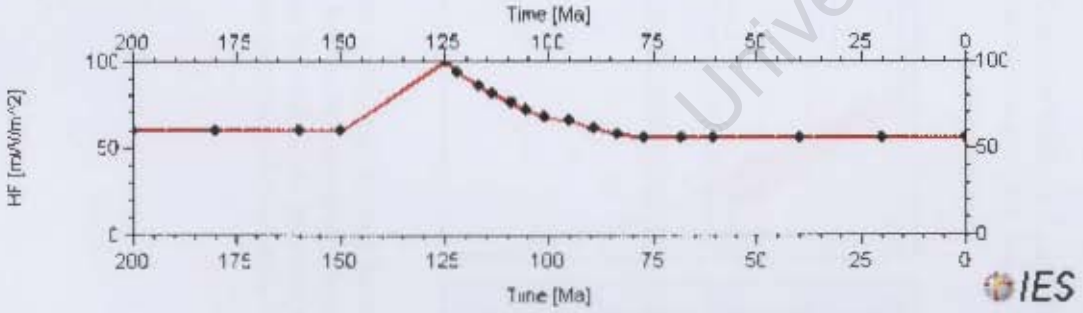

Figure 24: Heat flow model showing rifting at 125 Ma, followed by thermal decay (thermal subsidence) to present (based on McKenzie 1978).

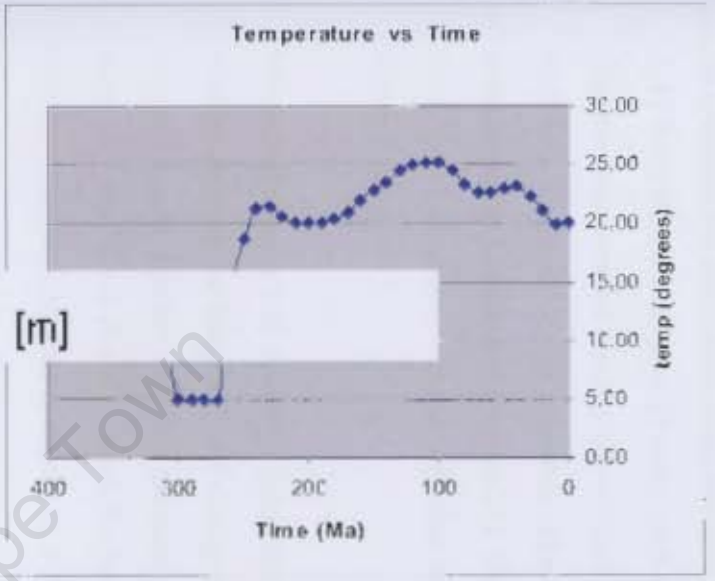

Figure 23: Simplified graph showing calculated variations of sea floor temperatures (Wygrala 1989) between 0 and 360 Ma.

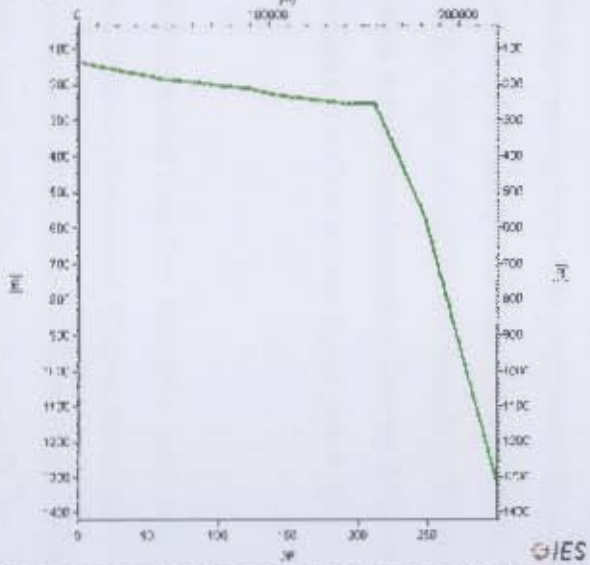

Figure 25: Linear temporal interpolation between rift initiation (sea level=0 ma) to present day. The graph shows the present day water depth vs. the length of the model in meters (side-axis and top-axis respectively).

3.3.2 Thermal model

To calibrate the paleo heat flow, vitrinite reflectance and temperature data for wells K-H1 and A-I1 from Block 3 (Figure 2) were used as calibration points for model predictions. These data are based on the kinetics for vitrinite maturation of Sweeney and Burnham (1990). No well-data for Block 2 was available. The location for depth extraction for thermal calibration was chosen at Location B (Figure 21). This location was chosen because it directly follows the 570 m bathymetry contour line that links through the well locations K-H1 and A-I1 in Block 3 (Figure 1).

Model calibration was achieved using the above determined heat flow history in conjunction with increasing the temporal and stratigraphic resolution of the model. Calibration of the original model was not accurate because the maturity and temperatures reflections plotted for well A-I1 and K-H1 did not match the best fit lines (see Figure 26 for the mismatch). An obvious mismatch is seen at depths of 3000 m to 4500 m.

a) Temperature Graph for Wells AI-1 and K-H1. The theoretical curve is the red line.

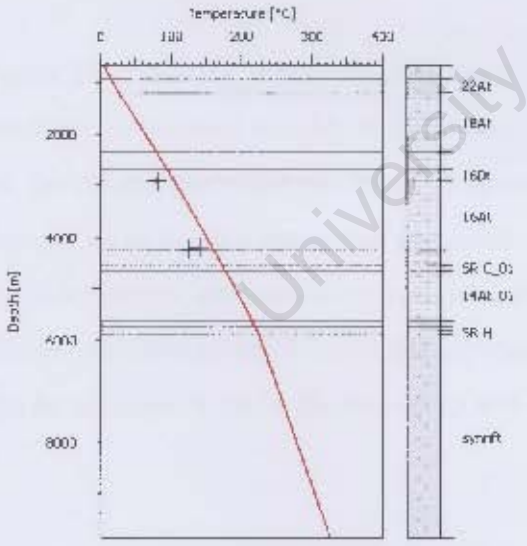

b) Vitrinite Graph for Wells AI-1 and K-H1 The theoretical curve is the black line.

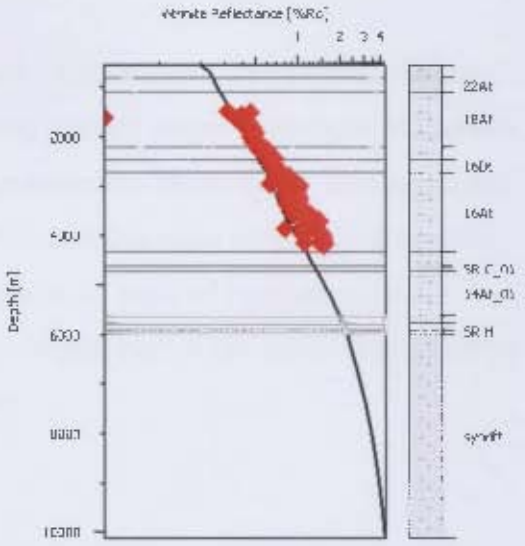

Figure 26 a-b: Predicted and observed (a) temperature and (b) vitrinite reflectance plotted for wells A-I1 and K-H1. The best fit lines for vitrinite reflectance derived from kinetic modelling are shown. Note the mismatch in temperatures for well A-I1 and in vitrinite reflectance for well K-H1 between the best fit line and observed data at depths 3000m to 4500m. The graphs were constructed at location B shown on Figure 21.

Calibration was improved through matching the observed variations of temperature and vitrinite reflectance plotted for well A-I1 and K-H1. Further improvement (see Figure 27) was obtained by additional modifications, i.e. through adding several more stratigraphic subdivisions and improving the facies variability according to the chronostratigraphic chart (Figure 3), and creating a more heterogeneous model of higher resolution (Figure 21).

The results of the seismic analysis combined with 2D basin modelling allows one to address the potential existence of active petroleum systems in the basin. Figure 28 shows the calculated transformation ratio (TR) that the individual source rocks have reached in the studied sections. TR represents the degree of transformation of kerogen to hydrocarbons expressed as a percentage (%). TR depends on the kinetics assigned to the respective source rocks as well as the time/temperature evolution as reconstructed in the basin model. Results reveal a significant lateral variation in the degree of kerogen conversion along the section studied. The entire Hauterivian, Barremian and Aptian source intervals have a TR in excess of 98%, a maturity that indicates almost complete kerogen conversion at these horizons at present time. The youngest source interval of Cenomanian/Turonian age has a TR ranging from 88% in the distal sectors of the basin to 5% in the proximal sectors of the basin. This sequence is essentially immature in the proximal part of the basin.

Figure 29 shows the reconstructed present day maturity across the studied section. Colour shadings correspond roughly to maturities representing general stages of kerogen conversion, i.e. the oil and gas windows. Most of the older source intervals (Hauterivian, Barremian and Aptian) lie in the dry gas to wet gas window. This indicates that most of the kerogens from the older source intervals have been transformed. Otherwise, most of the Cenomanian - Turonian source interval lies in the oil window. The deepest part of the same source interval can be assumed to be in the late-oil to wet-gas region.

a) Vitrinite graph for Well Al-1

b) Temperature graph for Well Al-1

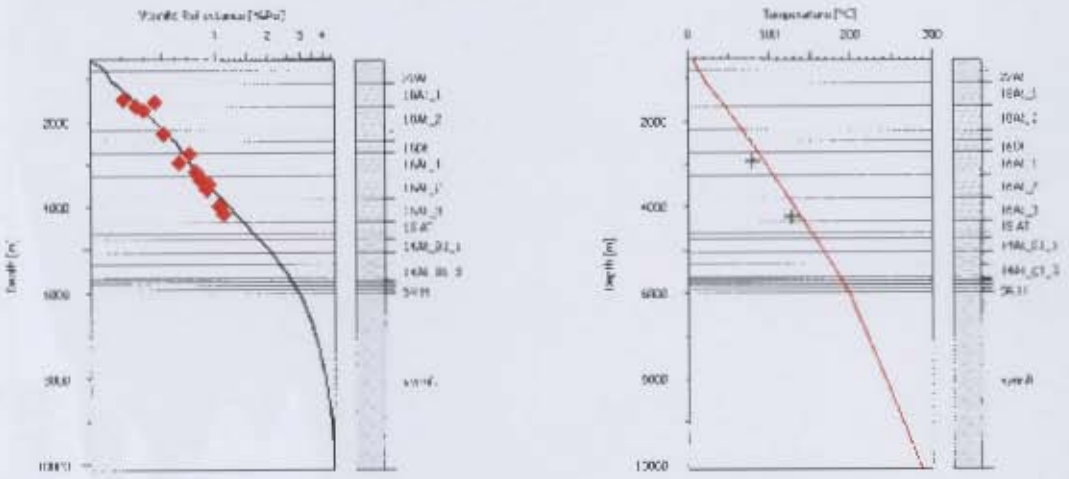

c) Vitrinite graph for Well KH-1

d) Temperature graph for Well KH-1

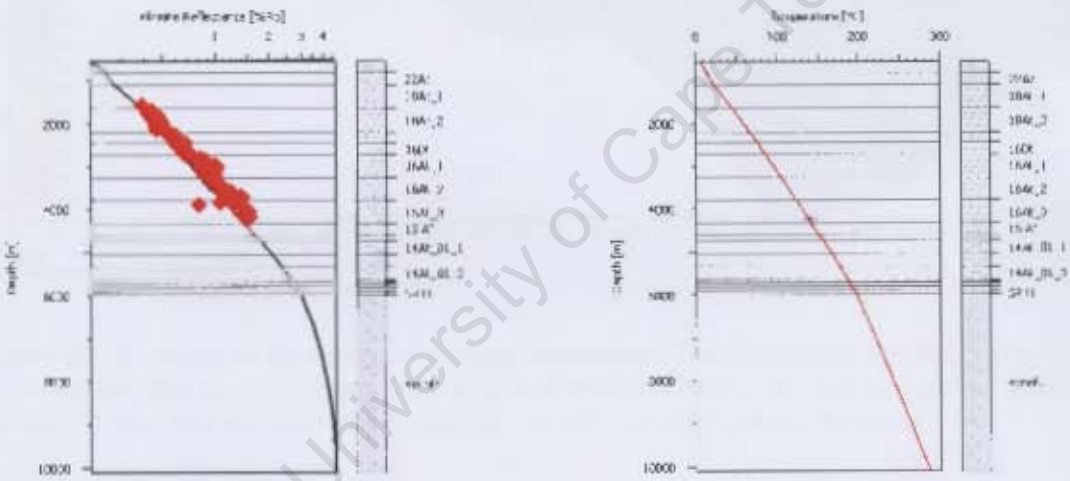

Figure 27: (a-b) Predicted and observed variations of vitrinite reflectance (a, c) and temperature (b, d) plotted for wells A-H and well K-H1 after improvement of the model by adding several boundaries and fitting the facies according to the chronostratigraphic chart. The graphs were constructed at location B shown on Figure 21.

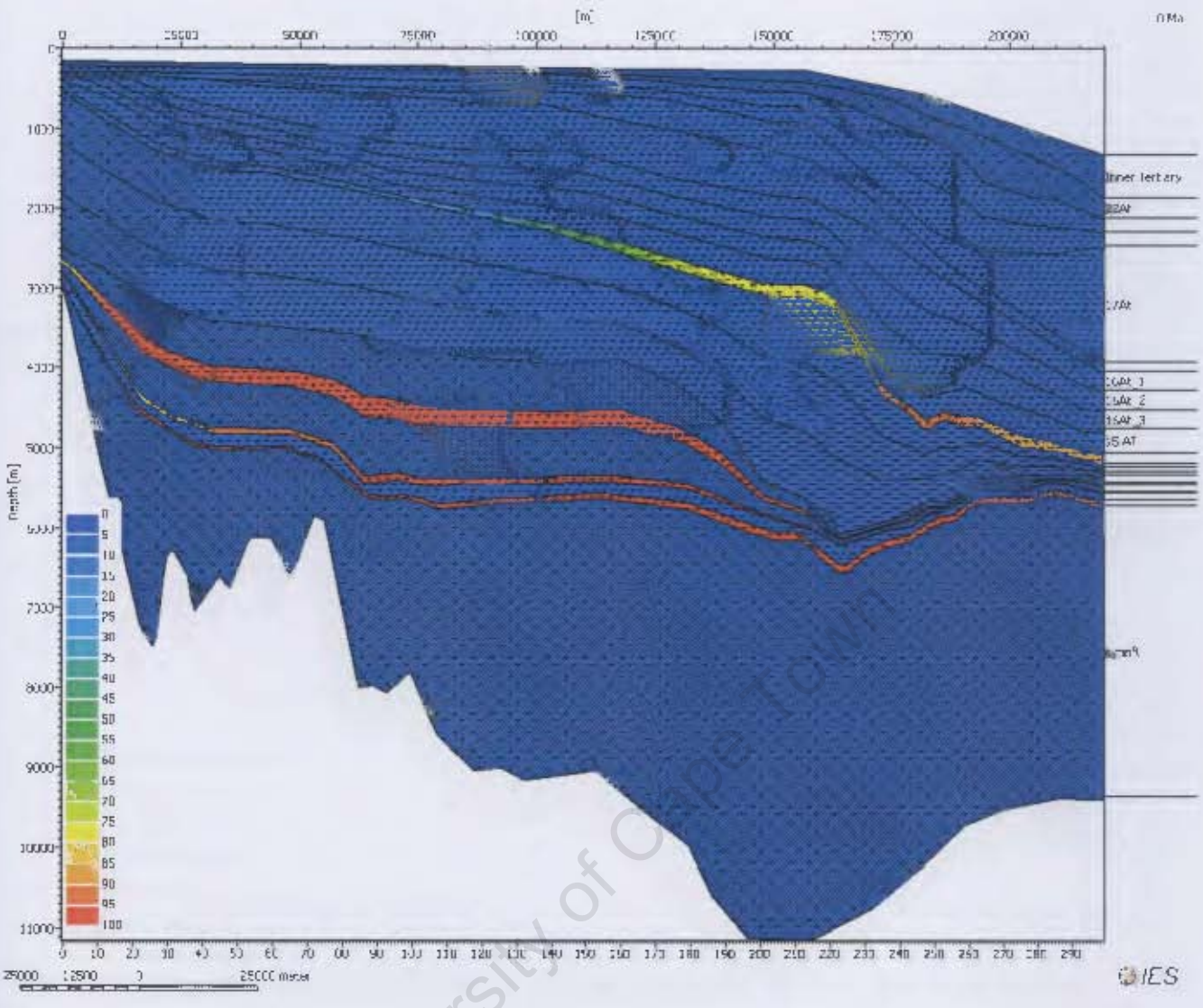

Figure 28: 2D model of the degree of kerogen conversion (Transformation Ratio) in the present day cross-section. The horizontal axis is the length of profile (220 km), the left axis shows the depth of profile (11 km), and the right axis delineates the names of stratigraphic horizons.

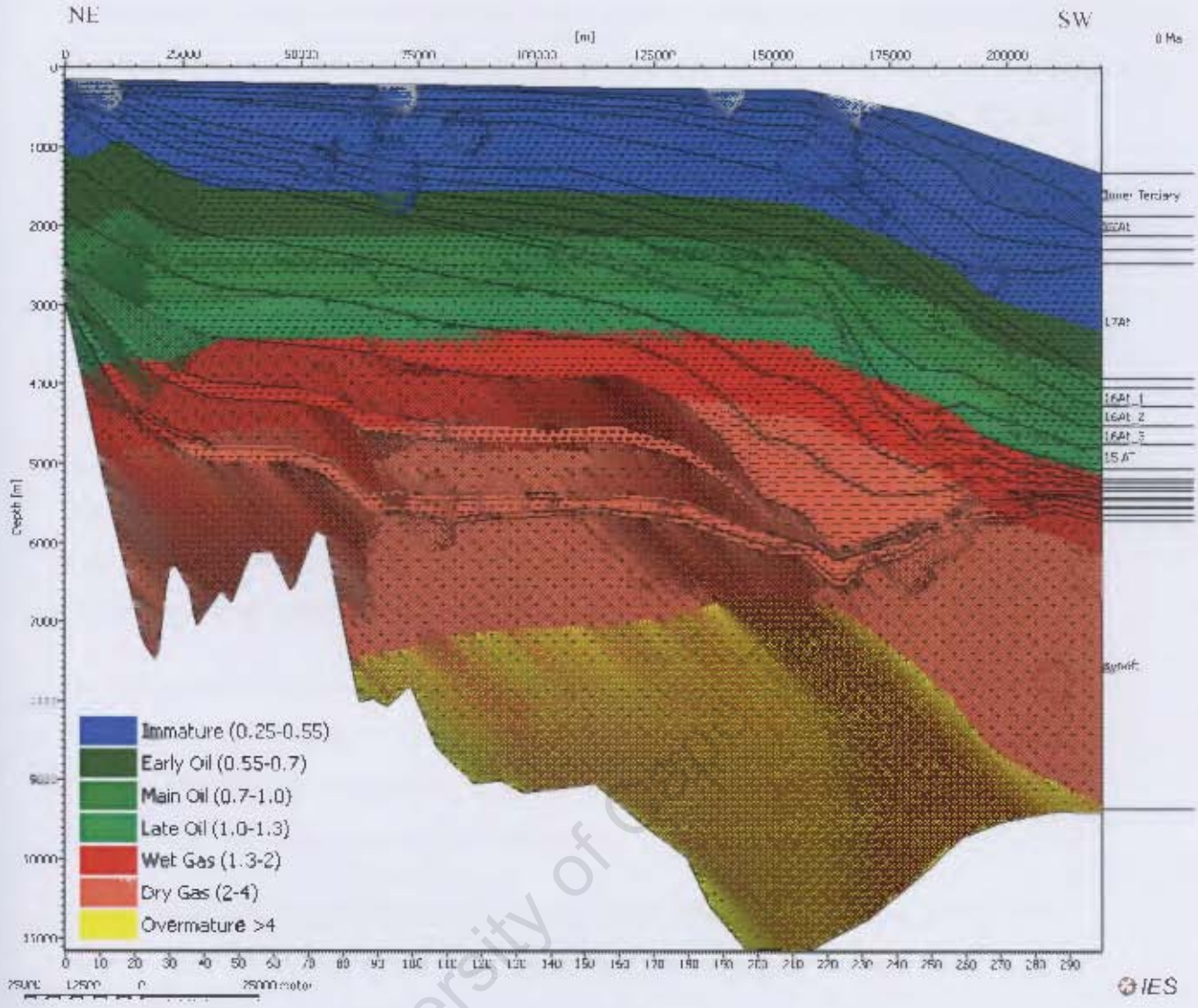

Figure 29: 2D model of the vitrinite values for the present day of study area cross section. The horizontal axis is the length of profile (220 km), the left axis shows the depth of profile (11 km), and the right axis delineates the names of stratigraphic horizons.

The thermal evolution of the basin can be expressed in terms of vitrinite reflectance and transformation ratio, and burial history. The evolution of vitrinite reflectance (i.e. maturity) of all four source rocks (Figure 30) was extracted from the model for locations A, B, and C shown in Figure 21. In the proximal part of the basin (Location A), the Hauterivian source rock has the highest vitrinite reflectance values at around 1.4 % Ro. The Cenomanian/ Turonian source rock is least mature at around 0.4% Ro. All source rocks start to mature in the early Cretaceous and reach maximum maturity in the late Cretaceous.

The middle part of the basin (Location B) has the highest vitrinite reflectance values, reaching up to 3% Ro. All four source rocks mature faster and within a shorter time span than the early Cretaceous at Location A. The Cenomanian/Turonian interval is again the least mature source rock. The distal part of the basin (Location C) is similar to the middle part (Location B), except that it has a lower vitrinite reflectance range reaching up to 2% Ro.

The transformation ratios over time for the four source rocks, at all locations, are displayed in Figure 31. Only at location A is the Cenomanian/Turonian source rock transformation ratio 0. This can also be seen in Figure 28, where the transformation ratio value is relatively low in the proximal basin for the younger source rocks.

Burial time-slices extracted from the 2D basin model allow a visualisation of the burial history, including erosional effects during the basin development. Rates of subsidence are highest during the Cretaceous, and decrease significantly in the Cenozoic. The results at locations A, B and C (Figure 32) show that subsidence was continuous from the Lower Cretaceous to the Upper Cretaceous, at which point maximum burial temperatures were reached. At locations B and C, burial is more or less continuous throughout the Cretaceous, but then slows down or essentially halts, during the early Cenozoic; thereafter burial increases again. These plots are similar to those recorded in the south of the Orange Basin (Paton et al., 2007; Kuhlmann et al., 2010). Paton et al. (2007) mention that at the end of the Cretaceous, aggradation with erosion in middle and inner shelf occurred, followed by deposition (prograding wedge) shifting across the shelf break and significant sediment volumes (Tinker et al., 2008) prograding into the deep basin.

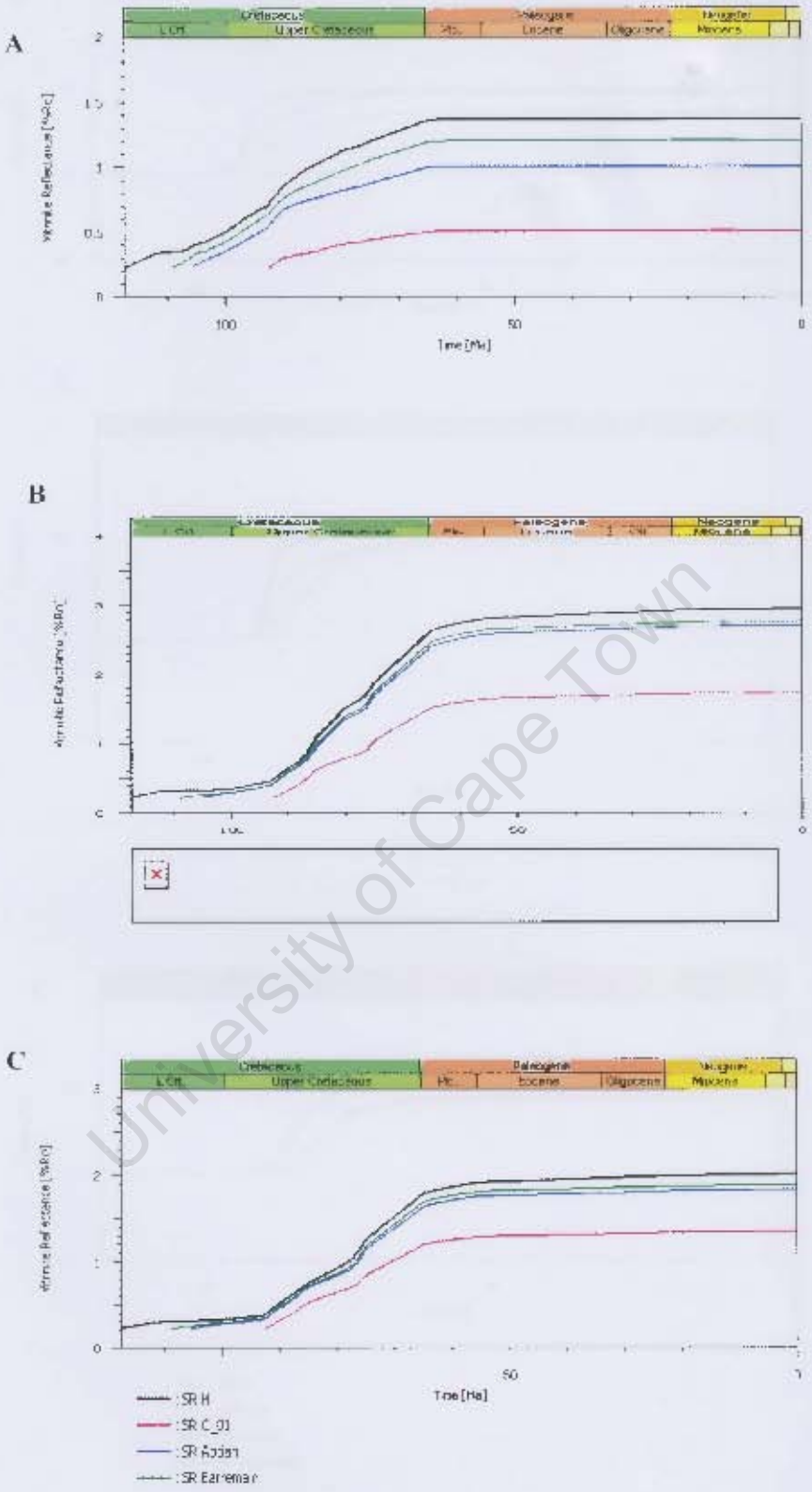

Figure 30: Model of the vitrinite variation over time in all four source rock is at locations A (proximal), B (middle) and C (distal). All four source rocks start to mature in the early Cretaceous, reaching a maximum maturity at the late Cretaceous, after which there is no further maturation. The Cenomanian/Turonian source rocks is the least mature and the Hauterivian source rocks is the most mature.

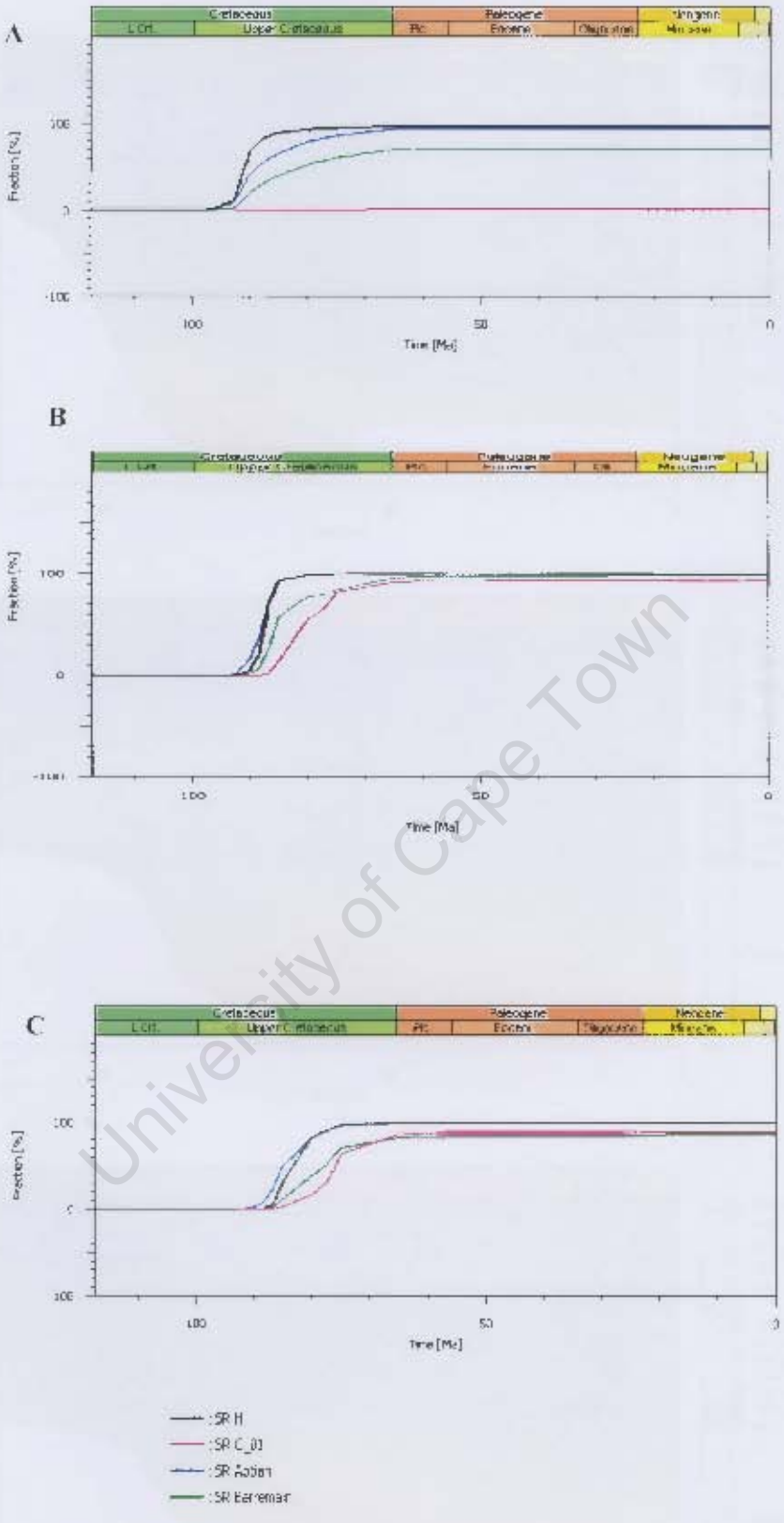

Figure 31: Model of maturation of all four source rocks at locations A, B and C (Figure 21). Note the major step in the Hauterivian source rock (black line), which has the highest transformation ratio (see Figure 28).

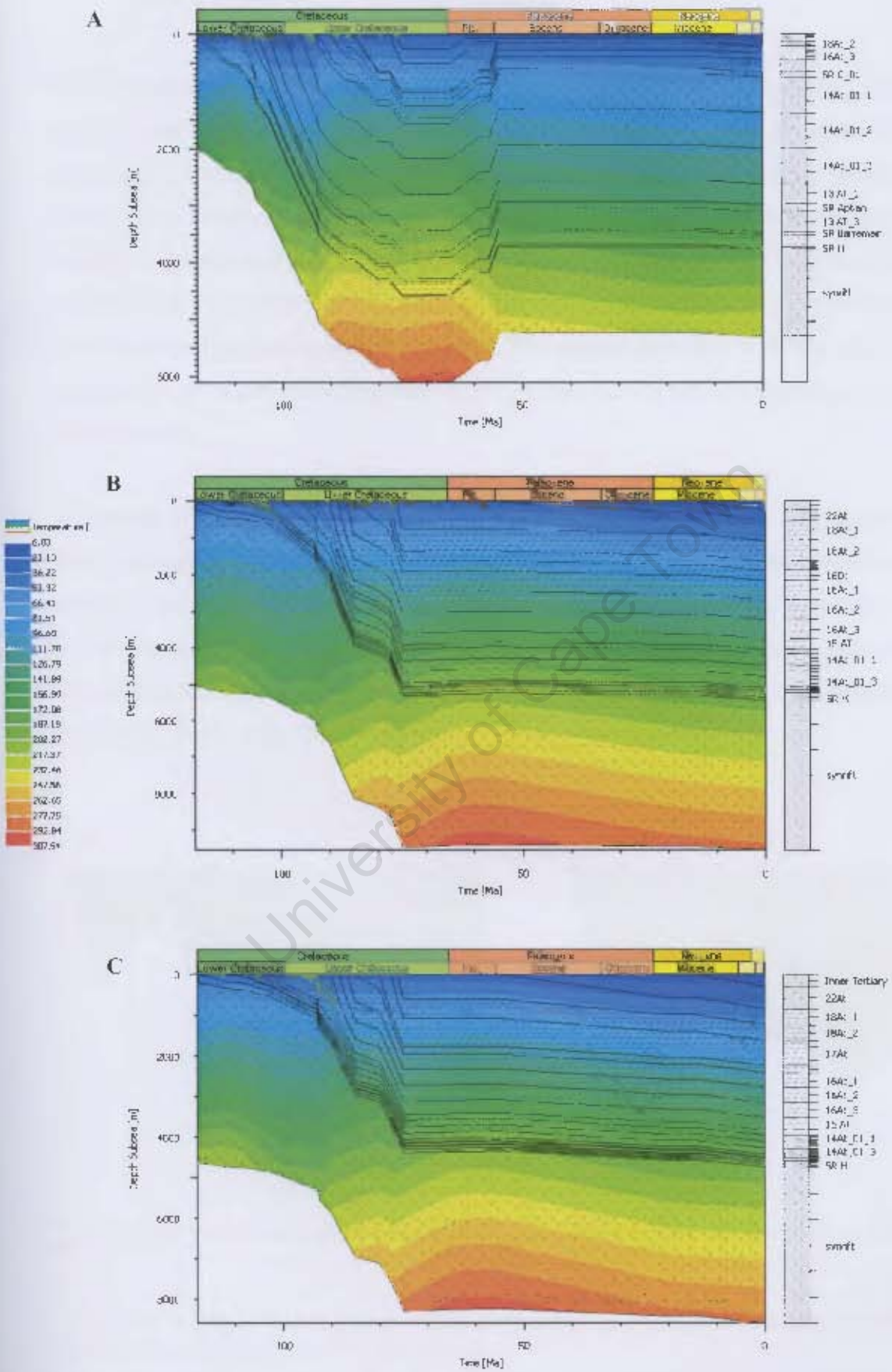

Figure 32: Model of burial histories at location A, B and C (Figure 2) with temperature overlays (see legend, blue=cold, red=warm). The burial history is a simple depth versus time plot in that deposition (and related burial) as well as times of non-deposition, and uplift are regenerated.

3.3.3. Reconstruction of Basin Evolution

The reconstructed basin development during the Cretaceous is shown in Figure 33. Basin development began in the Upper Jurassic and Lower Cretaceous when siliciclastic, lacustrine sediments and volcanic material first filled-up a complex of grabens and half-grabens (Figure 33a). Figure 33b shows the first major seismic Cretaceous Unit 1 that followed was deposited mostly in the proximal side of the basin. The same applies for seismic Cretaceous Unit 2 (Figure 33c). These depositional events explain the high subsidence rate at location A situated in the proximal part of the basin (Figure 32). The depositional style is clearly that of aggradation, as was already suggested by Paton et al. (2007) for the southern part of the Orange Basin.

In contrast to the agradational deposition of the Cretaceous Units 1 and 2, Cretaceous seismic Unit 3 (Figure 33d) displays a progradational tendency, with the thickest portions encountered off the Cretaceous shelf break. Cretaceous Units 4 and 5 also shows the same pattern as Unit 3. The Cenozoic Units 1 and 2 (Figure 33e) also show deposition (prograding Cenozoic wedge) that has shifted across the shelf break, so that significant volumes prograded into the deep basin (Paton et al., 2007).

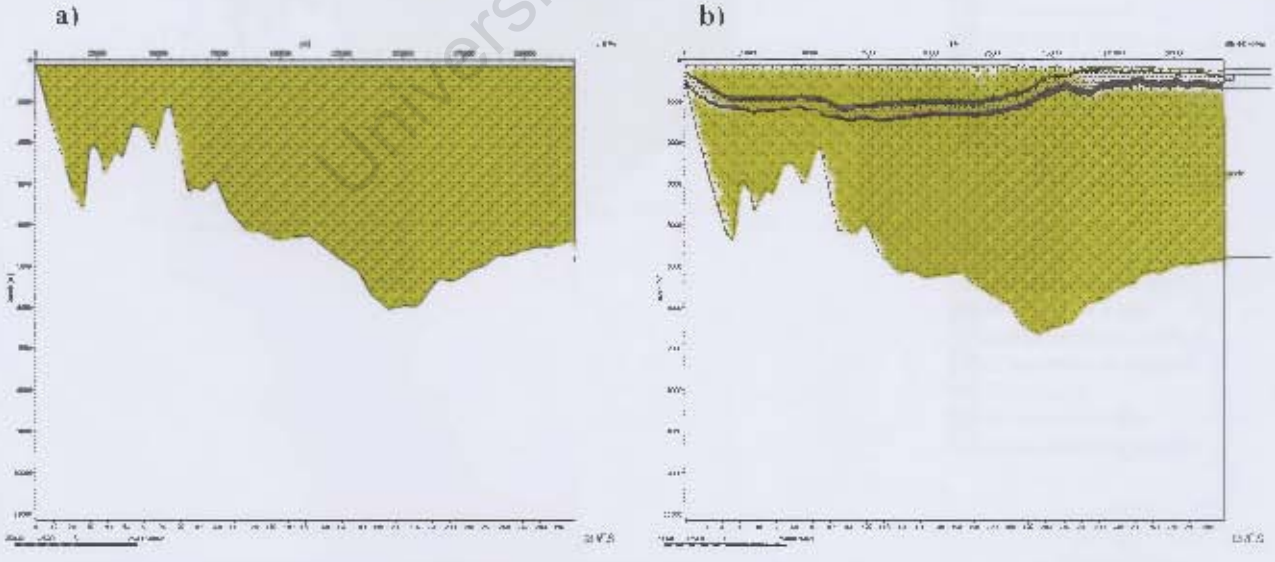

Figure 33 a-e: Graphs showing reconstructed evolution of the basin. a) From synrift to Cretaceous horizon 6At1. b) Deposition of Cretaceous unit 1.

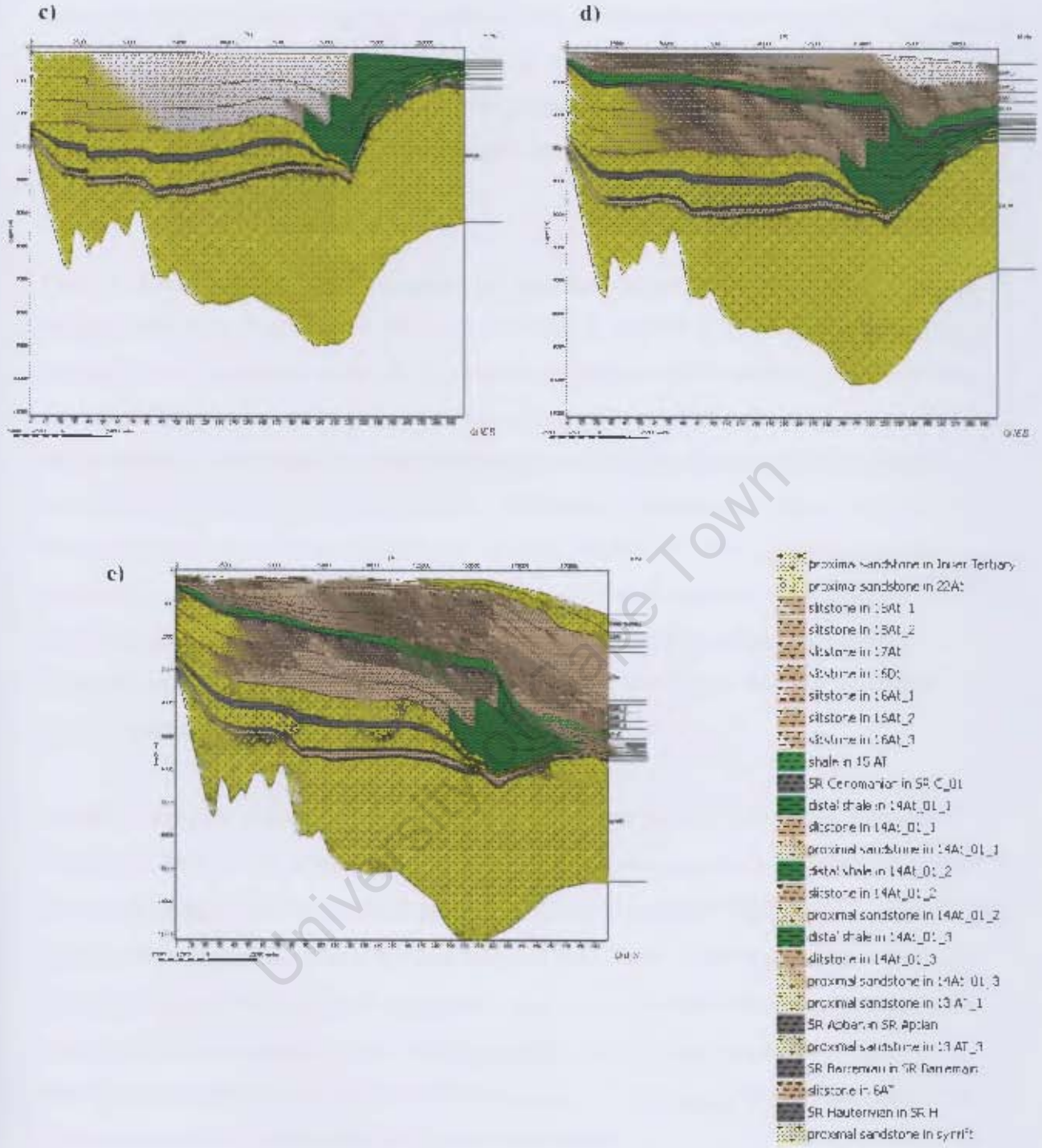

Figure 33 c-e continued: c) Deposition of Cretaceous unit 2. d) Deposition of Cretaceous unit 3. e) Deposition of Cenozoic units. Legend names cannot be corrected because the software is not available.

3.3.4. Fluid Migration model

Petroleum generation and migration modelling was performed in order to attempt to reproduce the observed gas leakage pathways in the basin. Reproduction of observed leakage sites would imply first that the basin-wide migration dynamics are being correctly described. Additionally, it would provide insights on petroleum migration dynamics and the location of the fluid source kitchen areas.

Flow modelling was performed assuming invasion percolation (Carruthers and de Lind van Wijngaarden 2000: Figure 34) as the preferred migration method. This assumes that flow through focused pathways occurs in the model as a function of the capillary entry pressure field in sedimentary systems. In other words, invasion percolation techniques assume that at the timescales of secondary petroleum migration hydrocarbon flow is overwhelmingly controlled by the balance between gravity (or buoyancy) and capillary forces. Viscous forces, which are taken into account in the Darcy equation, (see below) are negligible. Invasion percolation migration occurs only when fluids are generated and enter the secondary migration space. At this point fluids migrate in the sedimentary system as a function of hydrocarbon column height and capillary entry pressure until a final balance is reached. In this process time plays no role.

Another fluid flow modelling technique is based on using the full Darcy flow equation (Schneider 2003). This assumes that fluid-flow velocities are mainly a function of sediment permeability, fluid viscosity and the pressure gradient (Schneider 2003), and thus describe the timing of flow processes. The difference between the two flow techniques is that the Darcy based technique (Schneider 2003) suggests that all movable fluid will continue to move towards the top layer with time even after the fluid injection has stopped (buoyancy controlled, no perfect seal). On the other hand, Invasion Percolation modelling suggests that fluid movement will cease after fluid supply has stopped.

Flow path modelling is an additional fluid flow simulation technique that is based on the buoyancy as the principal driving force in hydrocarbon migration in carrier systems. Fluid flow in such carriers is modelled as a purely geometric problem (Hantschel et al., 2000). It assumes that the entire system is flow conductive and covered by a seal. Despite being a very rapid and high resolution approach, it is only applicable to carriers and is inadequate for the

Figure 34 (a): A migration model showing gas migration at the present day. Hydrocarbon migration is shown as maroon dotted lines and can reproduce the associations observed in the TWT seismic data (b) showing identified gas chimneys. The red block on the migration model (a) represents a section of the composite seismic line (b) chosen for basin modelling. The vertical lines represent the identified gas chimneys.

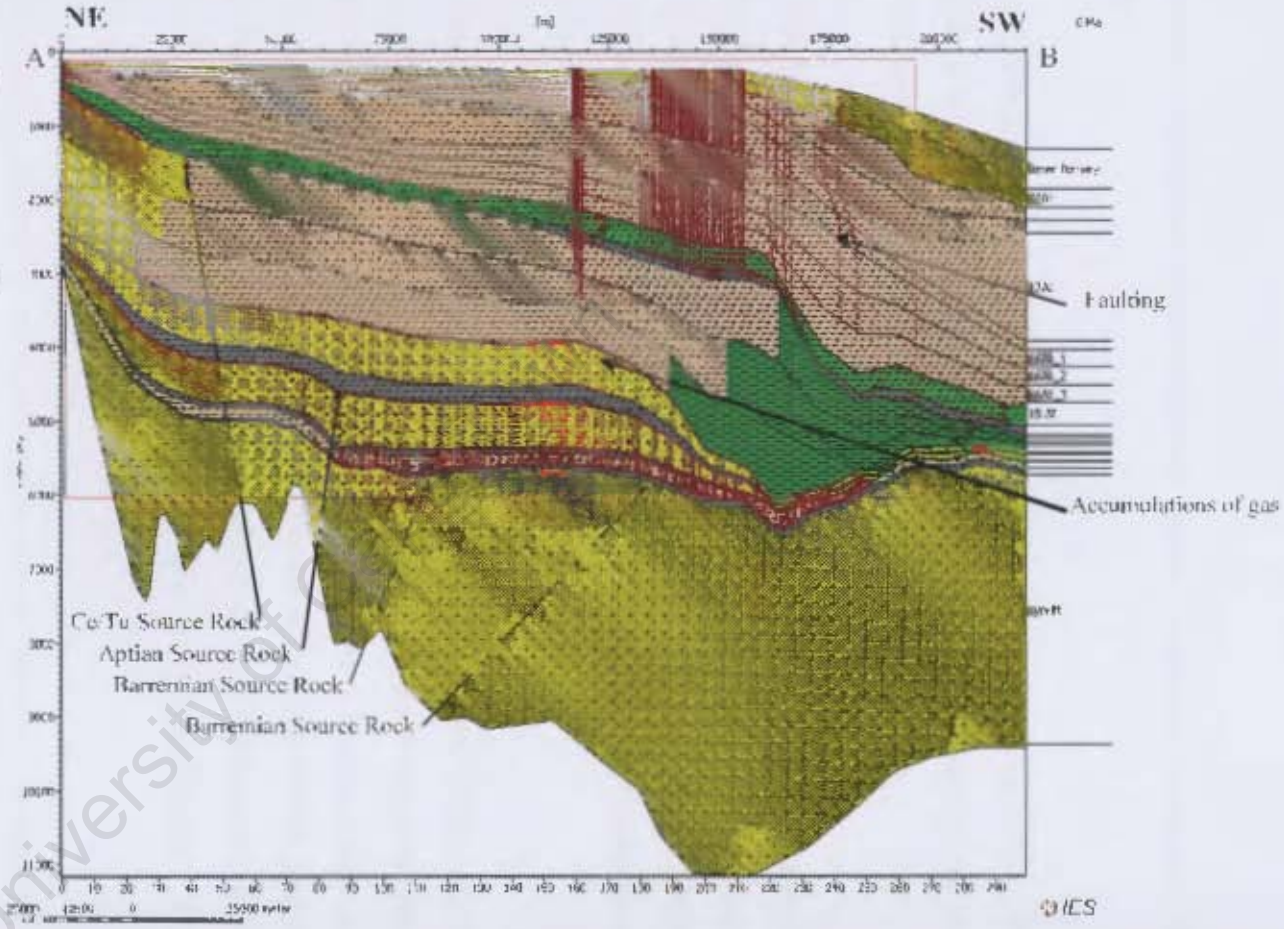

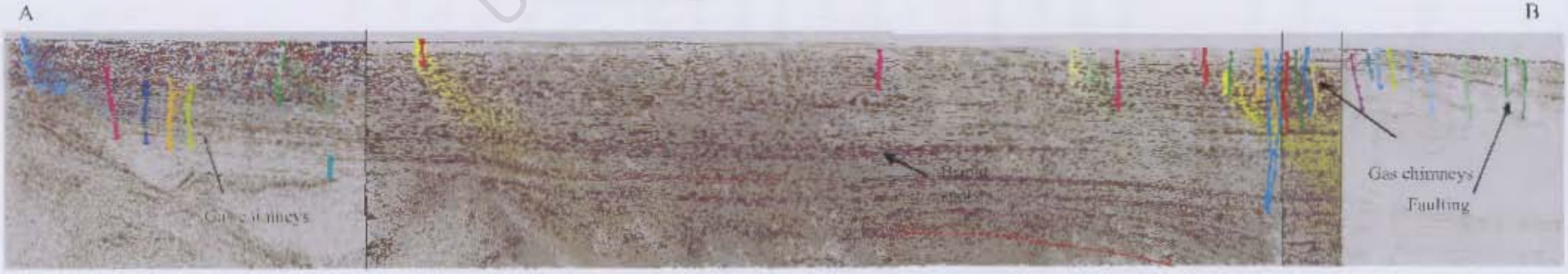

simulation of pervasive flow of fluids through low permeability sequences (Hantschel et al., 2000).

In my present study, invasion percolation was preferred for the modelling of fluid flow because it is more effective in creating a simpler migration model and because of significantly reduced computing time.

The resulting migration model reproduces at least two primary processes responsible for gas leakage across the basin (Figure 34). The first is petroleum migration that occurs in the lower shelf, where there is significant faulting. The second is in the middle and upper shelf, where the leakage is associated with vertical migration of free gas, despite apparent absence of significant faulting.

Hydrocarbons from the older marine source rocks of the Lower Aptian and Barremian age clearly migrate up-dip beneath the seals towards the proximal end of the basin. In the migration model (Figure 34a), the locations of the predicted hydrocarbon accumulations coincide with bright spots already identified in the seismic profiles (Figure 34b). After the gases have migrated to the proximal part of the basin, they subsequently leak to the sea floor in response to a change in the overlying lithologies (e.g. from siltstone to sandstone ; Figure 34a).

Hydrocarbons migrating to the shelf break and to the distal part of the basin are fed by younger source rocks of Cenomanian/Turonian age. No hydrocarbons from the younger source rocks are found to leak from the proximal part of the basin. This is most likely due to the comparatively low maturity of the younger Cenomanian/Turonian source rock in this area (Figure 29). To predict the position of other leakage sites, a 3D modelling approach is required.

3.3.5. Source Rock Kinetics

The Petro Report software (from Petromod) is a useful tool for estimating hydrocarbon generation, cracking and expulsion of the petroleum systems in the Orange Basin. However one mismatch produced through the Petro Report software is that it predicts, in total, more oil than gas leaking from the source rock system (2727 and 681.7 Mtons, respectively). In reality however more gas than oil should be leaking to the sea floor. This disprepancy may be due to the reaction parameters (e.g. Model 1 ; Figure 34) chosen in models that only differentiate between two phases, oil and gas (e.g. Pepper and Corvi, 1995a, 1995b, Pepper and Dodd, 1995). To create a more realistic petroleum flow system model, a second simulation model (Model 2 : Figure 35) was tested by changing the kinetic parameters of Model 1 based on Pepper and Corvi (1995) to compositional kinetic models (Table 5), that are based on the PhaseKinetic technique described by di Primio and Horsfield (2006). The applied compositional kinetics models allow the correct reproduction of hydrocarbon compositional evolution as a function of primary and secondary cracking as well as the correct simulation of hydrocarbon phase behaviour during migration and leakage.

Source rocks	**Kinetics for Model 1 (kerogen-oil and gas)**	**Kinetics for Model 2 (compositional for phase separation)**
SR Cenomanian	Pepper&Corvi(1995)_TII(B)	Botneheia_Svalbard_TII_Crack
SR Aptian	Pepper&Corvi(1995)_TII-S(A)	Botneheia_Svalbard_TII_Crack
SR Barremian	Pepper&Corvi(1995)_TIIIH(DE)	Handil_mahakamDelta_TIII_Crack
SR Hauterivian	Pepper&Corvi(1995)_TI(C)	Toarican_ParisBasin_TI_Crack

Table 5: Kinetic parameters assigned for different kerogen types in the source rocks of Models 1 & 2.

Although, results of migration Model 1 (Figure 34) and Model 2 (Figure 35) both accurately produce the spatial associations of the identified gas chimneys in the TWT seismic sections, the migration paths in Model 2 (Figure 35) are simpler and, unlike Model 1, shows migration of gases in the deeper sectors of the basin from the Cenomanian/Turonian source rocks and in addition, shows ongoing expulsion of hydrocarbons from the Aptian source rocks. These deep-sourced gases migrate from the mature source (kitchen) interval of Cenomanian/ Turonian age with a TR ranging up to 88% in the distal sectors of the basin (Figure 34).

The results show that whilst the thermal histories between Model 1 and 2 are similar, the hydrocarbon mass balance and the resulting migration models differ. Model 1 shows that

more of the products migrate subvertically, towards the surface than sub-horizontally (1962.2 and 967.4 Mtons, respectively). These results also indicate that the fluids are 24 - 25 times more likely to flow out of the Orange Basin than to be preserved within it as calculated from the Petro Report tables. The Petro Report for Model 2 indicates that the fluids also flow subvertically upwards, but only marginally more so than subhorizontially (1519.2 to 1370.9 Mtons, respectively). The fluids are also 24 times more likely to flow out than to be accumulated within the basin. The differences are largely due to the physical properties of the oil and gas phases modelled (i.e. density), which are probably more realistic for the full compositional model.

Figure 36 shows the modelled hydrocarbon fluids outflow from the models as a function of time. As discussed above, the difference between the two models is due to the different kinetic schemes applied and their control on the timing and extent of hydrocarbon generation from the source rocks.

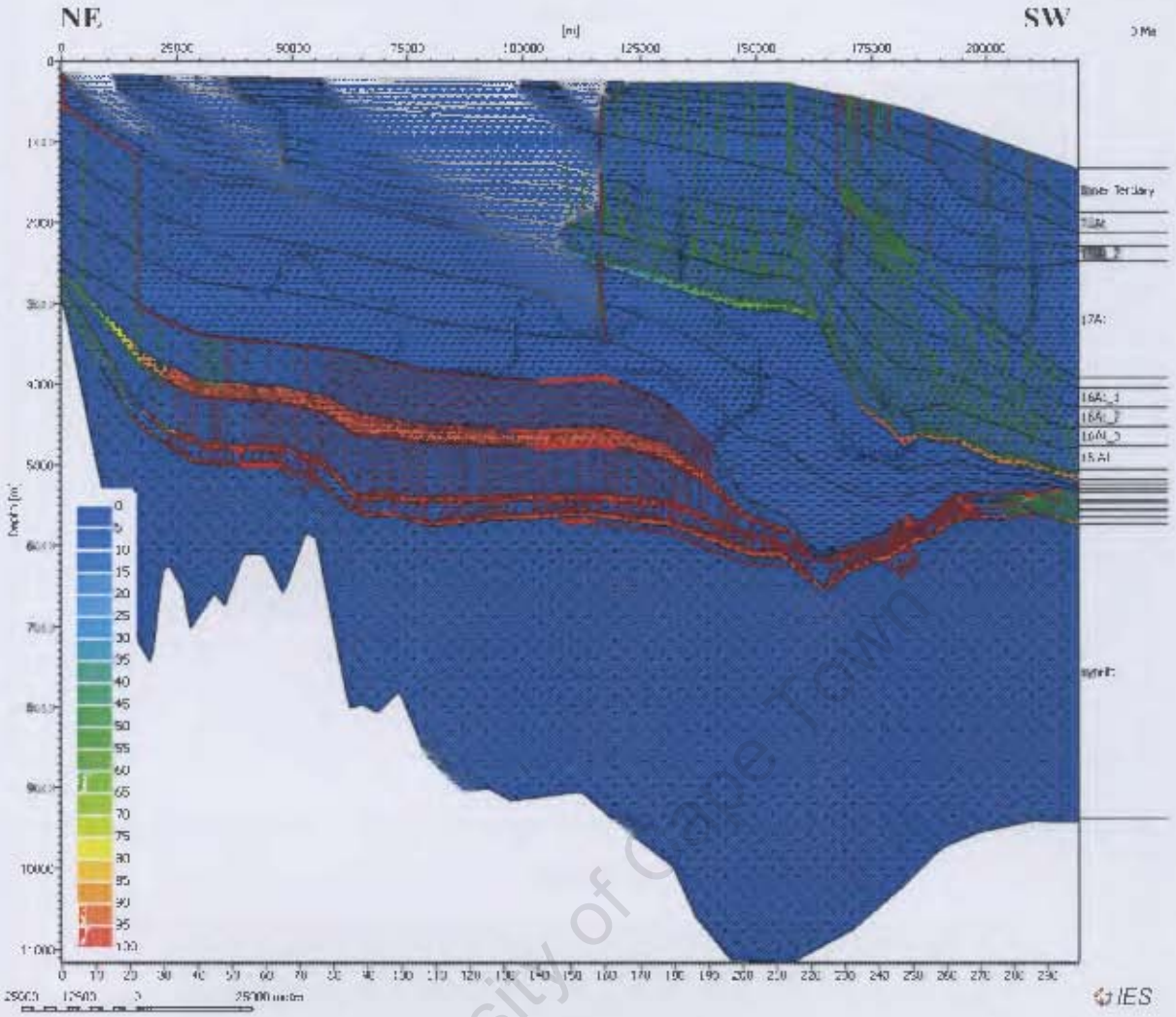

Figure 35: Migration paths and degree of kerogen conversion (Transformation Ratio) for Model 2. The dotted lines show the migration paths (gases=red and liquids=green). The colour ranges in the source rock intervals represent the Transformation Ratios (see legend).

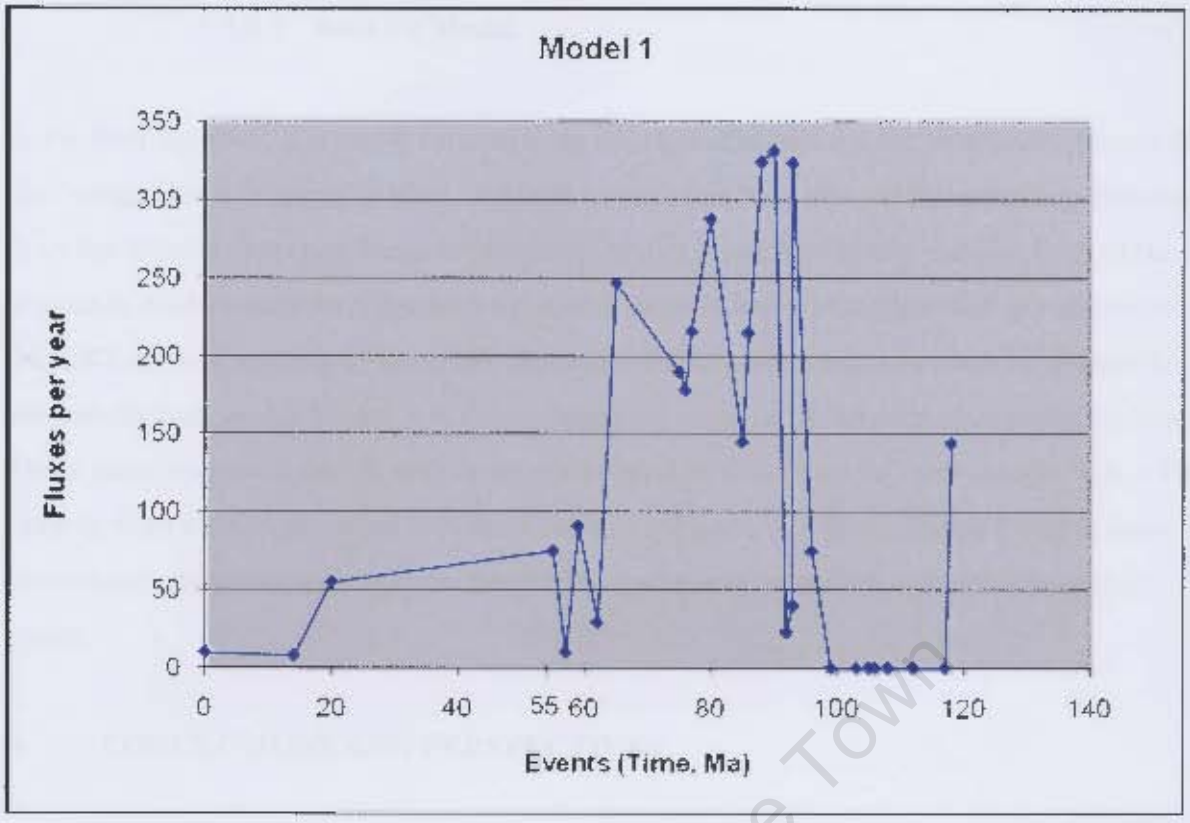

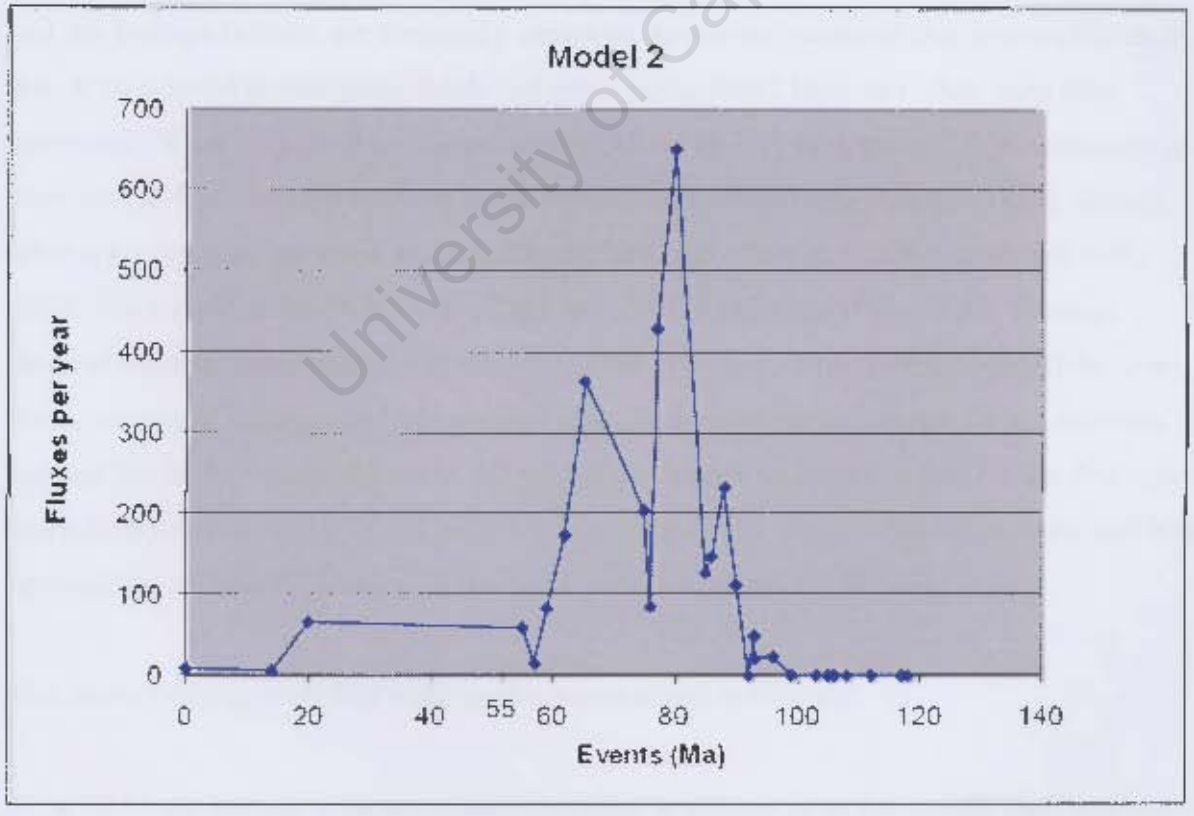

Figure 36: Graphs comparing the expulsion rates of hydrocarbons between Models 1 and 2. Note the more focused outflow of Model 2 centred about 80 Ma.

3.3.5.1 Best Fit Model

In the final analyses, it is worth summarizing which model best fits the petroleum systems of the Orange Basin, bearing in mind, that both models can be improved by increasing data input from the seismic data (e.g. facies constraints). Model 1 and 2 look very similar. Both of the migration models accurately produce the spatial associations of the identified gas chimneys in the TWT seismic sections (Figure 34). However, the migration paths in Model 2 (Figure 35) are simpler and, unlike Model 1, it shows migration of gases in the deep sections of the basin. These gases migrate from the mature source interval of Cenomanian/Turonian age with a TR ranging from 88% in the distal sectors of the basin (Figure 28). Since Model 2 makes more predictions consistent with what is observed in the seismic data, this is the preferred final model.

4. CONCLUSIONS AND PERSPECTIVES

Despite an apparent lack of hydrocarbon accumulations in the Orange Basin, gas chimneys and gas leakage features are frequently observed. Important questions that arise in this study are: Where do the thermogenic fluids and gases come from? How and when were they generated? What controls their migration; and where do they migrate to? Observations of gas chimneys and gas leakage features in the Block 2 area described here significantly expand what is known from previous work in the southern part of the basin (Ben Avraham et al., 2002; Viola et al., 2005; Paton et al., 2007 and 2008; Kuhlmann et al., 2010). Through detailed seismic interpretation and analysis of the evolution of the northern part of the Orange Basin, this work has provided clues about what the controlling factors are for gas mobility leakage out of the basin. Moreover, 2D petroleum modelling has provided, for the first time, more clarity on the timing of gas generation, migration and sequestration dynamics; and it has revealed the maturation history for the west-east transect across the basin.

The major findings from this work can be summarized as follows:

- 113 gas leakage indicators were identified as chimneys on the middle shelf and lower shelf of Block 2. The gas chimneys are classified into two main categories: stratigraphically-controlled and structurally-controlled. The structurally-controlled chimneys are mainly located in the extensional domain and originate along the normal

faults. The stratigraphically-controlled chimneys are linked to the presence of onlaps and pinch-outs within the Aptian sequence. No gas chimneys are observed in the compressive domain, but a giant chimney of a size of more than 7 km in diameter was observed in the middle margin of the Orange Basin.

- The source rocks of Early Cretaceous age have reached generally high levels of conversion, as expressed in the form of high Transformation Ratios (TR), and at the present time are generating gas that migrates laterally to the proximal part of the basin.

- The Late Cretaceous source rocks show only high levels of conversions to hydrocarbon fluids in the deep part of the basin. Migration of generated gas is limited to the shelf break and deeper part of the basin. The migration pathways are apparently linked to the stratigraphic-controlled (sa-c) and structural-controlled (s-c) chimneys mapped in the upper and middle shelves of the basin, respectively. The gas migrates up-dip along the basinward dipping listric faults of the extensional domain that are rooted in a décollement of Upper Cretaceous source rock. Thus, there is an intimate connection between the source rocks and gas leakage at the surface via the identified chimneys.

- The migration models indicate that the total system loses 24 times more thermogenic fluids than it retains. This indicates that low hydrocarbon preservation is a key risk for petroleum exploration.

- Giant chimneys are observed as paleo-escape structures that were covered by sediments at ca. 14 Ma (Miocene), possibly due to rapid burial during slumping caused by the onset of Benguela Current (Weigelt and Ünzelmann-Neben., 2004; Séranne and Anka., 2005). Shut-down of these gas escape structures would have terminated fluid escape. This event if integrated over the entire South African continental margin, may have contributed to the Neogene global cooling, but better quantification is needed to verify this (e.g. Ruddiman 2010).

Between 65 – 90 Ma, expulsion rates of hydrocarbons from the Orange Basin were extremely high, somewhere between 300 to 650 tons per year (Figure 36). This statement provides a bigger picture on the estimation of the basin's global impact of natural gas leakage through

the sediment into the atmosphere. For example, if geological emissions of methane (GEM) in the global methane budget are 50 megatonnes per year as proposed by Etiope (2004), and the expulsion rates from the northern part of the Orange Basin is an average ca. 500 tons per year (Figure 36), then the basin would have been leaking a mere 0.002 % of global GEM to the atmosphere. It still needs to be established if this leakage from the northern part of the Orange Basin is representative of continental margins elsewhere in order to establish their total contribution to the global budget.

In detail, the Transformation Ratio of all source rocks increased at about 90 Ma, and reached a constant plateau at about 70 Ma lasting until the present (Figure 31). Thus, most of the gases were generated and expelled during the Late Cretaceous, 65 – 90 Ma. These high expulsion rates of hydrocarbons are coincident with the high subsidence rates, maximum burial temperatures in the basin (Paton et al., 2007 and Kuhlmann et al., 2010 ; Figures 31 and 32) and with the extensive gravity sliding of the Orange Basin around 80 Ma (de Vera et al., 2010). The expulsion rates dropped close to about 10 to 20 tons per year around 65 Ma, then increased again between 20 and 55 Ma to about 100 tons per year (Figure 36). This increase coincides with the period that deposition had shifted across the shelf break at the end of the Cretaceous, and significant volumes of sediments prograded into the deep basin, leading to burial, maturation of the youngest source rock and gas production under the prograding Cenozoic wedges (Figure 29). It is possible this increase at 55 Ma could have contributed to the PETM around 55 Ma (Zachos et al., 2008: Figure 36), but this needs further work before a clear answer can emerge. Overall, the precise global volume of methane leaking to the seafloor from continental margins is unknown. However, from this work, it appears that methane contributions from the Orange Basin to the atmosphere and its possible effects on paleo-climate evolution was non-linear and can vary substantially through time.

The seismic data and well data from the Orange Basin still contain more valuable information to improve basin models further, e.g. petrophysical properties, hydraulic properties of faults in the extensional domain and the lithofacies that can be all used to resolve stratigraphic units in more detail. Kinetic parameters for hydrocarbon cracking too must meet more stringent requirements (Waples 2000), e.g. (1) Fit the laboratory data on oil cracking and gas formation, (2) Make predictions that are consistent with empirical observations and with chemistry and thermodynamics and (3) be more flexible for use in available software programs.

Clearly challenges remain ahead, particularly because only very few passive margins have been investigated for gas escape structures. However, this work has provided a model of the Orange Basin that enhances understanding on how, where and why the gases in this basin are generated, migrate and leak relative to the structural and stratigraphic elements of the basin. Continuation of this type of work will provide further understanding on the relationship of methane migration and seepage with structural and stratigraphic elements, as well as on the timing and amounts of gas leakage to the hydrosphere and atmosphere from sedimentary basins worldwide. In turn, they may lead to a better understanding of the role of basin fluids to past climate changes.

5. REFERENCES

Abrams, M.A., 1996. Distribution of subsurface hydrocarbon seepage in near surface marine sediments, in D. Schumacher and M.A Abrams, eds., Hydrocarbon migration and its near surface expression. AAPG memoir, 66, 1-14.

Barton, K.R., Muntingh, A., and Noble, R.D.P., 1993. Geophysical and geological studies applied to hydrocarbon exploration on the west coast margin of South Africa. Extended abstract of the Third International Congress of the Brazilian Geophysical Society, Rio de Janerio, Brazil. November 7-11, 1993.

Ben-Avraham, Z., Smith, G., Reshef, M., and Jungslager, E., 2002. Gas Hydrate and mud volcanoes on the southwest African continental margin off South Africa. Geology, 30, 927-930.

Bray, R., Lawrence, S., and Swart, R., 1998. Source rock, Maturity Data indicates potential off Namibia. Oil and Gas Journal, 96, 84-49.

Brendt, C. 2005. Focused fluid flow in passive continental margins. Philosophical Transactions of the Royal Society A, 363, 2855-2871.

Broad, D.S., Jungslager, E.H.A., McLachlan, I.R., and Roux, J., 2006. Offshore Mesozoic Basins. In: M.R. Johnson, Anhaeusser, C.R., Thomas, R.J. (Editor), The Geology of South Africa. Geological Society of South Africa, Johannesburg/Council for Geosciences, Pretoria, 553-571.

Brown, Jr., L. F., Benson, J. M., Brink, G. J., Doherty, S., Jollands, A., Jungslager, E. H., Keenen, A., Muntingh, A., and. van Wyk, N. J. S., 1995. Sequence stratigraphy in offshore South African divergent basins. An atlas on exploration for Cretaceous lowstand traps by Soekor (Pty) Ltd.: AAPG Studies in Geology, 41, 184 pp.

Bunz, S., Mienert, J., Brynw, P and Bergw, K. 2005. Fluid flow impact on slope failure from 3D seismic data: a case study in the Storegga Slide. Basin Research, 17, 109–122.

Carruthers, D.J., and de Lind van Wijngaarden M., 2000. Modelling viscous-dominated fluid transport using modifiedinvasion percolation techniques. Journal of Geochemical Exploration, 69–70, 669–672.

Cole, D., Stewart, S.A., Cartwright, J.A., 2000. Giant irregular pockmark craters in the Palaeogene of the Outer Moray Firth Basin, UK North Sea. Marine and Petroleum Geology, 17, 563-577.

Cranston, R.E., Ginsburg, G.D., Soloviev, V.A., Lorenson, T.D. 1994. Gas venting and hydrate deposits in the Okhotsk Sea. Bulletin of the Geological Society of Denmark, 41, 80–5.

Crutzen, P.J., 1991. Methane's sinks and sources. Nature, 350, 380 – 381.

de Vera, J., Granado, P., and McClay, K., 2010. Structural evolution of the Orange Basin gravity-driven system, offshore Namibia. Marine and Petroleum Geology, 27, 223-237.

de Wit, M.J., 2007. The Kalahari Epeirogeny and climate change: differentiating cause and effect from Core to Space. South African Journal of Geology, 110, 367-392.

de Wit, M.C.J., Marshall, T.R., and Partridge, T.C., 2000. Fluvial Deposits and Drainage Evolution. In: T.C., and Maud, R.R., Oxford (Eds.), The Cenozoic of Southern Africa Partridge, University Press, New York, 55-72.

di Primio, R., Horsfield, B., 2006. From petroleum-type organofacies to hydrocarbon phase prediction. AAPG Bulletin, 90, 1031-1058.

Dickens, G.R., 2003. Rethinking the global carbon cycle with a large, dynamic and microbially mediated gas hydrate capacitor. Earth and Planetary Science Letters, 213, 169-183.

Dimitrov, L.I., 2002. Mud volcanoes; the most important pathway for degassing deeply buried sediments. Earth-Science Reviews, 59, 49-76.

Dingle, R.V., Siesser, W.G, Newton, A.R., 1983. Mesozoic and Tertiary geology of Southern Africa. A.A Balema, Rotterdam, 355pp.

Dingle, R.V, and Hendy, Q.B., 1984. Late Mesozoic and Tertiary sediment supply to the eastern Cape Basin (SE Atlantic) and palaeo-drainage systems in southwestern Africa. Marine Geology, 56, 13–26.

Dingle, R.V., Robson, S.H., 1992. Southwestern African continental rise: structural and sedimentray evolution. In: Poag, W., de Graciansky (Eds.), Geologic evolution of Atlantic Continental Rifts. Van Nostrand Reinhold, New york, pp. 62-75.

Etiope, G., and Klusman, R.W., 2002. Geologic emissions of methane to the atmosphere. Chemosphere, 49, 777–789.

Etiope, G., 2004. New Directions: GEM—Geologic Emissions of Methane, the missing source in the atmospheric methane budget. Atmospheric Environment, 38, 3099–3100.

Etiope, G., Keith, R.L., Ronald, W.K and Boschi, E., 2008. Reappraisal of the fossil methane budget and related emission from geologic sources. Geophysical Research Letters, 35, 1-5.

Foubert, A., Depreiter, D., Beck, T., Maignien, L., Pannemans, B., Frank, N., Blamart, D., and Henriet, J.P., 2008. Carbonate mounds in a mud volcano province off north-west Morocco: Key to processes and controls. Marine Geology, 248, 74–96.

Gay, A., Lopez, M., Cochonat, P., Levaché, D., Sermondadaz, G., and Séranne, M., 2006. Evidences of early to late fluid migration from an upper Miocene turbiditic channel revealed by 3D seismic coupled to geochemical sampling within seafloor pockmarks, Lower Congo Basin. Marine Petroleum Geology, 23, 387–399.

Gerrard, I., and Smith, G. C., 1982. Post-Palaeozoic succession and structure of the south-western African continental margin, in J. S. Watkins and C. L. Drake, eds., Studies in Continental Margin Geology.: AAPG Memoir, 34, 49–74.

Gradstein, F., Ogg, J., and Smith, J., 2004. A Geologic Time Scale. Cammbridge University Press, United Kingdom, 589pp.

Haacke, R. R., Westbrook,G.K., and Hyndman R.D., 2007. Gas hydrate, fluid flow and free gas: Formation of the bottom-simulating reflector. Earth and Planetary Science Letters, 261, 407–420.

Hantschel, T., Kauerauf, A.I., and Wygrala, B., 2000. Finite element analysis and ray tracing modelling of petroleum Migration. Marine and Petroleum Geology, 17, 815-820.

He, T., Spence, G.D., Riedel, M., Hyndman, R.D., and Chapman, N.R., 2007. Fluid flow and origin of a carbonate mound offshore Vancouver Island: Seismic and heat flow constraints. Marine Geology, 239, 83–98.

Heggland, R., 1997. Detection of gas migration from a deep source by the use of exploration 3D seismic data. Marine Geology, 137, 41-47.

Herbin, J.P., Muller, C., Graciansky, P.C. de Jacquin, T., Magniez-Jannin, F. and Unternehr, P., 1987. Cretaceous anoxic event in the South Atlantic. Revista Brasileria de Geociencia, 17, 92-99.

Higgins, J.A and Schrag, D.P., 2006. Beyond methane: Towards a theory for the Palaeocene–Eocene Thermal Maximum. Earth and Planetary Science Letters, 245, 523–537.

Hirsch, K., Scheck-Wenderoth, M., van Wees, J., Kuhlmaan, G. And Paton, D.A., 2009. Tectonic subsidence history and thermal evolution of the Orange Basin. Marine and Petroleum Geology, 1-20.

Hovland, M., and Judd, A.G., 1988. Seabed Pockmarks and Seepages. Graham and Trotman, London, United Kingdom, 293pp.

Hovland, M., and Thomsen, E., 1997. Cold-water corals – are they hydrocarbon seep related? Marine Geology, 137, 159-164.

Judd, A.G., Davies, G., Wilson, J., Holmes, R., Baron, G., and Bryden, I., 1997. Contributions to atmospheric methane by natural seepages on the UK continental shelf. Marine Geology. 137, 165-189.

Judd, A.G., Hovland, M., Dimitrov, L.I., Garcia Gil, S., and Jukes, V., 2002. The geological methane budget at Continental Margins and its influence on climate change. Geofluids, 2, 109-126.

Jungslager, E. H. A., 1999. Petroleum habitats of the Atlantic margin of South Africa, in N. R. Cameron, R.M. Bate, and V. S. Clure, eds., The oil and gas habitats of the South Atlantic: Geological Society (London) Special Publication, 153, 153– 168.

Kaluza, M.J., and E.H. Doyle, 1996. Detecting Fluid Migration in Shallow Sediments: Continental Slope Environment, Gulf of Mexico., in D. Schumacher and M.A Abrams, eds., Hydrocarbon migration and its near surface expression. AAPG memoir, 66, 15-26.

Kennett, J.P., Cannariato, K.G., Hendy, I.L. and Behl, R.J. 2002. Methane Hydrates in

Quaternary Climate Change: The Clathrate Gun Hypothesis. American Geophysical Union, Washington DC, 216 pp.

Kenyon, N.H., Akhmetzhanov, A.M., Wheeler, A.J., van Weering, T.C.E., de Haas, H., and Ivanov, M.K., 2003. Giant carbonate mud mounds in the southern Rockall Trough. Marine Geology, 195, (1-4), 5-30.

King, L.H., and MacLean, B., 1970. Pockmarks on the Scotian Shelf. Geological Society of America Bulletin, 81, 3141–3148.

Kounov, A., Viola, G., de Wit, M., and Andreoli M. A. G., 2009. Denudation along the Atlantic passive margin: new insights from apatite fission-track analysis on the western coast of South Africa.Geological Society, London, Special Publications, 324, 287-306.

Kuhlmann, G., Adams, S., Campher, C., van der Spuy, D., di Primio, R., and Horsfield, B., 2010. Passive margin evolution and its controls on natural gas leakage in the southern Orange Basin, block ¾, offshore South Africa. Marine and Petroleum Geology, 27, 973-992.

Limonov, A.F., van Weering, T.C.E., Kenyon, N.H., Ivamov, M.K., and Meisner, L.B., 1997. Seabed morphology and gas venting in the Black Sea mud volcano area: Observations with the MAK1 deep-two sidescan sonar and bottom profiler. Marine Geology, 137, (1-2), 121-136.

MacDonald, I.R, Buthman, D.B., Sager, W.W., Peccini, M.B., and Guinasso, N.L., 2000. Pulsed oil discharge from a mud volcano. Geology, 28, (10), 907-910.

MacDonald, D., Gomez-Perez, I., Franzese J., Spalleti, L., Lawver, L., Gahagan, L., Dalziel, I., Thomas, C., Trewin, N., Hole, M., and Paton, D., 2003. Mesozoic break-up of SW Gondwana: implications for regional hydrocarbon potential of the southern South Atlantic. Marine and Petroleum Geology, 20, 287-308.

Mazinni, A., Svensen, H., Hovland, M., and Planke, S. 2006. Comparison and implications from strikingly different authigenic carbonates in a Nyegga complex pockmark, G11, Norwegian Sea. Marine Geology, 231, 89–102.

McElwain, J.C., Wagner, P., and Hesselbo, S., 2009. Fossil Plant Relative Abundances Indicate Sudden Loss of Late Triassic Biodiversity in East Greenland. Science, 324, 1554-1556.

McKenzie, D., 1978. Some Remarks on the Development of Sedimentary Basins. Earth and Planetary Science Letters, 40, 25-32.

Milkov, A.V., 2000. Worldwide distribution of submarine mud volcanoes and associated gas hydrates. Marine Geology, 167, 29-42.

Milkov, A.V., 2004. Global estimates of hydrate-bound gas in marine sediments: How much is really out there? Earth Science Reviews, 66, 183-197.

Moulin, M., Aslanian, D., Unternehr, P., 2010. A new starting point for the South and Equatorial Atlantic Ocean Earth. Science Reviews, 98, 1–37.

Muntingh, A. and Brown, Jr. L. F., 1993. Sequence stratigraphy of petroleum plays, postrift Cretaceous rocks (lower Aptian to upper Maastrichtain). Orange Basin, western offshore, South Africa. In P. Weimer and H.W Posamentier (Eds.) Siliciclastic sequence stratigraphy-recent developments and applications. AAPG Memoir, 58, 71-97.

Naeth, J., Di Primio, R., Horsfield, B., Schaefer, R.G., Shannon, P.M., Bailey, W.R., Henriet J.P. and Henriet J.P., 2005. Hydrocarbon seepage and carbonate mound formation: A basin modelling study from the Porcupine Basin (offshore Ireland). Journal of Petroleum Geology, 28, 147-166.

Nurnberg, D., and Muller, R.D., 1991. The tectonic evolution of the South Atlantic from Late Jurassic to present. Tectonophysics, 191, 27–53.

Paton, D.A., di Primio, R., Kuhlmann, G., van der Spuy, D., and Horsfield, B., 2007. Insights into the petroleum system evolution of the southern Orange Basin, South Africa. South African Journal of Geology, 110, 261-274.

Paton, D.A., van der Spuy, D., di Primio, R., and Horsfield, B., 2008. Tectonically induced adjustment of passive-margin accommodation space; influence on the hydrocarbon potential of the Orange Basin, South Africa. AAPG Bulletin, 92, (5), 589-609.

Pepper, A.S. and Corvi, P.J., 1995a. Simple kinetic models of petroleum formation. Part I: oil and gas generation from kerogen. Marine and Petroleum Geology, 12, 291-319.

Pepper, A.S. and Corvi, P.J., 1995b. Simple kinetic models of petroleum formation. Part III: Modelling an open system. Marine and Petroleum Geology, 12, 417-452.

Pepper, A.S. and Dodd, T.A., 1995 Simple kinetic models of petroleum formation. Part II: oil to gas cracking. Marine and Petroleum Geology, 12, 321-340.

Petroleum Agency SA, 2003. South African Exploration Opportunities. South African Agency for Promotion of Petroleum Exploration and Exploitation, Parrow, Cape Town, 28pp.

Pilcher, R., Argent, J., 2007. Mega-pockmarks and linear pockmark trains on the West African continental margin. Marine Geology, 244, 15-32.

Riding, R., 2002. Structure and composition of organic reefs and carbonate mud mounds: concepts and categories. Earth-Science Reviews, 5, 163–231.

Rodrigo, C., Vera, E., and González-Fernández, A., 2009. Seismic analysis and distribution of a bottom-simulating reflector (BSR) in the Chilean margin offshore of Valdivia (40° S). Journal of South American Earth Sciences, 27, (1), 1-10.

Ruddiman, W.F., 2010. A Paleoclimatic Enigma? Science Magazine, 328, 838-839.

Séranne, M., Abeigne, C. -R. Nzé., and Lopez, M. 1999. Oligocene to Holocene sediment drifts and bottom-currents on the slope of Gabon continental margin (West Africa). Consequences for sedimentation and southeast Atlantic upwelling. Sedimentary Geology 128, 179–199.

Séranne, M. and Anka, Z., 2005. South Atlantic continental margins of Africa: A comparison of the tectonic vs climate interplay on the evolution of equatorial west Africa and SW Africa margins. Journal of African Earth Sciences, 24, 283-300.

Sahling, H., Bohrmann, G., Spiess, V., Bialas, J., Breitzke, M., Ivanov, M., Kasten, S., Krastel, S., and Schneider, R., 2008. Pockmarks in the Northern Congo Fan area, SW Africa: Complex seafloor features shaped by fluid flow. Marine Geology, 249, 206-225.

Schneider, F., 2003. Modelling multiphase flow of petroleum at the sedimentary basin scale. Journal of Geochemical Exploration, 78-79, 693-696.

Schroot, B.M.; Klaver, G.T., and Schüttenhelm, R.T.E., 2005. Surface and subsurface expressions of gas seepage to the seabed- examples from the Southern North Sea. Marine and Petroleum Geology, 22, 499-515.

Svensen, H., Jamtveit, B. and Planke, S. 2003. Seep carbonate formation controlled by hydrothermal vent complexes: a case study from the Vøring volcanic basin, the Norwegian Sea. Geo-Marine Letters, 23, 351–358.

Svensen, H., Planke, S., Malthe-Sørenssen, A., Jamtveit, B., Myklebust, R., Rasmussen Eidem, T., and Rey, S.S. 2004. Release of methane from a volcanic basin as a mechanism for initial Eocene global warming. Nature, 429, 542-545.

Sweeney, J.J. and Burnham, A.K., 1990. Evaluation of a Simple Model of Vitrinite Reflectance Based on Chemical Kinetics. American Association of Petroleum Geologists Bulletin, 74, 1559-1570.

Tankard, A.K., and Rogers, J., 1978. Late Cenozoic Palaeoenvironments on west coast of southern Africa. Journal Biogeography, 5, 319-337.

Tinker, T., de Wit, M., and Brown, R., 2008. Linking source and sink: Evaluating the balance between onshore erosion and offshore sediment accumulation since Gondwana break-up, South Africa. Tectonophysics, 455, (1-4), 94-103.

Trumbull, R. B., Reid, D. L., de Beer, C., van Acken, D., and Romer, R.L., 2007. Magmatism and continental breakup at the west margin of southern Africa: A geochemical comparison of dolerite dikes from northwestern Namibia and the Western Cape. South African Journal of Geology, 110, 477-502.

Van de Schootbrugge, B., Payne, J.L., Tomasovych , A., Pross, J., Fiebig, J., Benbrahim, M., Follmi, K.B., and Quan, T.M., 2008. Carbon cycle perturbation and stabilization in the wake of the Triassic-Jurassic boundary mass-extinction event. Geochemistry, Geophysics, Geosystems, 9, 1-16.

Van der Spuy, D., Ziegler, T., and Bowyer, M., 2003. Deepwater 2D data reveal Orange Basin objectives off western South Africa. Oil and Gas Journal, 101, 44– 49.

Van Rensbergen, P., de Batist, MM., Klerkx, J., Hus, R., Poort, J., Vanneste M., Granin, N., Khlystov, O., and Krinitsky, P., 2002. Sublacustrine mud volcanoes and methane seeps caused by dissociation of gas hydrates in Lake Baikal. Geology, 30 (70), 631-634.

Viola, G., Andreoli, M., Ben-Avraham, Z., Stengel, I., and Reshef, M., 2005. Offshore mud volcanoes and onland faulting in southwestern Africa: neotectonic implications and constraints on the regional stress field. Earth and Planetary Science Letters, 231, 147-160.

Waples, D., 2000. The kinetics of in-reservoir oil destruction and gas formation: constraints from experimental and empirical data, and from thermodynamics. Organic Geochemistry, 31, 553-575.

Weigelt, E. and Ünzelmann-Neben, G., 2004. Sediment deposits in the Cape Basin: Indications for shifting ocean currents? AAPG Bulletin, 88, 6, 765-780.

Westerhold, T., Bickert, T., and Röhl, U., 2005. Middle to late Miocene oxygen isotope stratigraphy of ODP site 1085 (SE Atlantic): new constrains on Miocene climate variability and sea-level fluctuations, Palaeogeography, Palaeoclimatology, Palaeoecology, 217, 205-222.

Whiticar, M.J., 1989. A geochemical perspective of natural gas and atmospheric methane. Advances in Organic Geochemistry, 16, 531-547.

Wood, W.T., Gettrust, J.F., Chapman, N.R., Spence, D.D., and Hyndman, R.D., 2002. Decreased stability of methane hydrates in marine sediments owing to phase boundary roughness. Nature, 420, (6916), 656-660.

Wuebbles, D.J., and Hayhoe, K., 2002. Atmospheric methane and global change. Earth-Science Reviews, 57, (3-4), 177-210.

Wygrala, B.P., 1989. Integrated study of an oil field in the southern Po basin, northern Italy. Forschungs zentrum Jülich reports, 2313.

Zachos, J.C., Dickens, G.R and Zeebe, R.E., 2008. An early Cenozoic perspective on greenhouse warming and carbon-cycle dynamics. Nature, 451, 279-283

6. APPENDIX 1: GAS CHIMNEY PROPERTIES

The appendix below represents the properties of each gas chimney mapped in Block 2 (Figure 15a). The gas chimneys were studied to see if they:

- Leak to the surface.
- Have structural, stratigraphic or paleo types.
- Are located at which certain water depths (Bathymetry).
- Have different sizes of pockmocks (Diameter).
- Have different sizes of mounds (Diameter).
- Are sealed within the Tertiary.
- Are gigantic chimney or if they have clusters (Other).
- Show the BSR mentioned in Ben-Avraham et al's paper (2002).

no.	Leak to surface	strat.	struc.	paleo (passive)	Bathymetry TWT	Pockmark size	Mound size	Sealed in Tertiary?	other
1	X		x		more than 500	567	973	T	(BSR?)
2			x		more than 500	clusters	2984	T	gigantic) clusters
3	X		x		more than 500	clusters	305		
4	X		x		more than 500	clusters	3489	T	(gigantic)
5	X		x		more than 500	clusters	2370	T	
6		x			more than 500	135		T	
7		x			more than 500	487		T	
8			x		more than 500		287	T	
9			x		more than 500	89		T	
10	X		x		more than 500	364	699		
11			x		more than 500	459		T	
12	X		x		more than 500		2795	T	(BSR?)
13	X		x		more than 500	clusters	3771	T	Gigantic (BSR?)
14	X		x		more than 500	562	870	T	(BSR?)
15	X		x		more than 500	clusters	2812		
16			x		more than 500	clusters	2138		
17			x		more than 500				
18			x		more than 500				
19			x		more than 500		1115		
20		x		x	more than 500	389			channel source?
21		x		x	more than 500	263			
22	X	x			300-500	200			
23	X	x			300-501	112			(BSR)?
24	X	x			300-500	316			
25	X		x		more than 500		1224		
26		x			300-500		2051	T	gigantic
27	X	x			more than 500		174		
28			x		more than 500	clusters	1481	T	
29			x		more than 500			T	
30	X				400				

31		x			400			T	
32		x			400			T	
33		x			300				
34	x	x			400	514			
35	x	x			300				
36		x			350	515		T	
37	x	x			300				
38		x			300		2386	T	Gigantic
39	x	x			300				
40	x		x		400		1527		Clusters
41	x	x		x	350	700			
42	x	x		x	more than 500	393			
43	x		x		500				
44	x		x		500	299			
45	x		x	x	500	571			
46		x			200			T	
47		x			300			T	
48		x			300		1080	T	
49	x	x			320	684			
50	x	x			400	455			
51		x			400		2465,2	T	double mounds?
52	x	x			300				
53		x			300	9171, 92		T	giagantic pockmark? (same as 54
54		x			300	7231		T	gig pockmark (same as 53)
55		x			350			T	double chimneys?
56		x			350			T	
57		x			350				
58		x			350				
59		x			350				
60		x			400				
61		x			400				
62		x			400				
63		x			400				
64		x			400				
65		x			400				
66		x			350				
67		x			350				
68		x			300				
69	x	x			300				
70	x	x			295				
71	x	x			300				
72	x	x			300				
73	x	x			300				
74		x			300				
75		x			300				
76		x			300				
77		x			300				
78		x			290				
79		x			290				
80		x			290				

81		x			295			T	
82		x			300				
83	X	x			300				
84		x			300				
85		x			300	7554			collapsed structure
86		x			300			T	
87	X	x			300	250			
88	X		x			402	402	T	
89		x			295			T	
90		x			295			T	
91		x			295			T	
92		x			295			T	
93		x			350			T	
94		x			300			T	
95		x			300			T	
96		x			300			T	
97	X	x			300-500				
98	X	x			less than 300				
99		x			600-5000				
100	X	x			less than 300				
101	X	x			less than 300				
102	X	x			less than 300				
103	X	x			less than 300				
104	X	x			less than 300				
105	X	x			less than 300				
106	X	x			less than 300				
107	X			x	1300	1358			
108	X			x	1750	740			
109	X			x	800	514			
110	X			x	1450	520			
111	X			x	2000		2222		
112	X			x	1600	749			
113	X			x	2000	717			

APPENDIX 2: PETRO REPORT

Appendix 2 below represents the Petro Report tables from Petromod for Models 1 and 2. It is a useful tool for estimating hydrocarbon generation, cracking and expulsion of the petroleum systems in the Orange Basin. The data highlighted below are the ones mentioned in this study.

Model 1

	Gas	Oil	Sum
SR C_01	92.7	776.7	869.5
SR Aptian	87.2	318.9	406.1
SR Barremian	49.4	77.2	126.6
SR H	463.1	1610.6	2073.7
Sum Generated	692.4	2783.5	3475.9
SR C_01	7.1	55.7	62.8
SR Aptian	1.5	0.4	2.0
SR Barremian	1.0	0.3	1.3
SR H	1.1	0.1	1.2
Sum Accumulated in Source	10.7	56.5	67.3
SR C_01	85.6	721.1	806.7
SR Aptian	85.7	318.5	404.2
SR Barremian	48.3	76.9	125.3
SR H	462.0	1610.5	2072.5
Sum Expelled	681.7	2727.0	3408.6
Inner Tertiary	0.1	0.5	0.5
22At1	0.1	0.9	0.9
14At1_01_1	0.5	8.3	8.7
14At1_01_2	0.0	0.5	0.5
14At1_01_3	0.0	0.3	0.4
13 AT_1	30.4	0.2	30.6
13 AT_3	44.5	0.1	44.5
synrift	29.0	0.0	29.0
Sum Accumulated in Reservoir	104.6	10.6	115.2
Migration Losses	8.3	150.5	158.7
Sec. Cracking Losses	450.1	655.2	205.1
Inner Tertiary	1.8	4.8	6.7
22At1	10.4	41.0	51.4
18At_1	123.2	327.3	450.5
18At_2	23.5	87.5	110.9
17At1	69.0	97.7	166.7

16Dt1	83.6	109.8	193.4
16At1_1	61.4	11.7	73.1
16At1_2	55.5	19.7	75.2
16At1_3	88.9	49.4	138.3
15 AT	104.3	154.3	258.6
SR C_01	5.6	18.4	24.0
14At1_01_1	141.7	222.1	363.7
14At1_01_2	9.7	40.1	49.8
Sum Outflow Top	778.5	1183.7	1962.2
16Dt	0.3	0.1	0.4
16At1_1	0.9	2.0	2.9
SR C_01	0.2	2.1	2.4
14At1_01_2	0.0	0.2	0.3
13 AT_1	32.0	180.2	212.2
SR Aptian	0.1	0.2	0.3
13 AT_3	185.8	324.0	509.8
6At1	18.9	210.9	229.9
SR H	1.7	1.9	3.6
Synrift	0.5	5.2	5.6
Sum Outflow Side	240.4	726.9	967.4
Sum HC Losses	577.1	2716.3	3293.5

Model 2

	Methane	Ethane	Propane	i-Butane	n-Butane	i-Pentane	n Pentane	C6	PK_P10	PK_P20	PK_P30	PK_P40	PK_P50	PK_P60+	Sum
SR C_01	61.06	19.11	20.45	3.18	13.95	10.48	8.25	34.54	212.76	160.67	77.31	31.83	11.57	5.55	670.71
SR Aptian	40.17	11.62	12.30	1.89	8 45	5.88	5.19	20.53	121.97	92.83	45.04	18.64	6.72	3.12	394.34
SR Barremian	22.70	4.31	5.86	1.95	3.21	2.71	2.08	6.58	44.04	26.22	9.97	3.22	0.89	0.29	134.04
SR II	246.00	63.01	63.06	8 17	42 18	31.70	29.93	88.45	562.53	486.18	270.10	128.22	53.42	30.64	2103.59
Sum Generated	369.93	98.04	101.68	15.18	67.79	50.77	45.45	#####	941.29	765.89	402.43	181.91	72.60	39.60	3302.67
SR C_01	3.72	1.56	1.74	0 27	1.16	1.06	0.62	3 04	19.92	14.51	6 89	2.90	1.13	0.59	59.10
SR Aptian	0.63	0.11	0.12	0.02	0.08	0.05	0.05	0.20	1.06	0.76	0.34	0.13	0.04	0.02	3.60
SR Barremian	0.50	0.06	0.08	0 02	0.04	0.03	0.03	0 09	0.30	0.16	0.06	0.02	0.01	0.00	1.40
SR II	1.74	0.13	0.13	0.02	0 09	0.05	0.05	0.19	0.45	0.27	0.10	0.03	0.01	0.01	3.28
Sum Accumulated in Source	6.58	1.86	2.07	0.33	1.38	1.19	0.76	3.51	21.73	15.69	7 38	3.09	1.19	0.62	67.38
SR C_01	57.34	17.55	18.72	2.91	12 79	9.42	7.63	31.49	192.84	146.16	70.42	28.93	10.44	4.96	611.61
SR Aptian	39.54	11.50	12.18	1.87	8.37	5.83	5.14	20 34	120.91	92.07	44 70	18.51	6.68	3.10	390.73
SR Barremian	22.20	4.25	5.79	1.93	3 17	2.68	2.05	6.50	43.74	26.06	9.91	3.20	0.88	0.29	132.64
SR II	244.26	62.87	62.93	8.15	42.09	31.65	29.87	88.27	562.07	485.91	270 01	128.18	53.41	30.63	2100.31
Sum Expelled	363.34	96.18	99.62	14.86	66 42	49.58	44.69	#####	919.56	750.20	395.04	178.83	71.41	38.98	3235.29
Inner Tertiary	0.02	0.01	0.01	0.00	0.00	0.00	0.00	0.01	0.07	0.06	0.03	0.01	0.00	0.00	0.23
22At	0.02	0.01	0.01	0.00	0.01	0.01	0.01	0.02	0.14	0.10	0.05	0.02	0.01	0.00	0.40
14At1_01_1	0.49	0.15	0.25	0.05	0 23	0.19	0.18	0.67	4.50	3.49	1.32	0.32	0.05	0.02	11.91
14At1_01_2	0.01	0.01	0.01	0.00	0.01	0.01	0.00	0.01	0.10	0.07	0.03	0.01	0.01	0.00	0.28
14At1_01_3	0.01	0.01	0.01	0.00	0 00	0.00	0.00	0.01	0.08	0.06	0.03	0.01	0.00	0.00	0.24
13 AT_1	22.03	1.17	1.23	0.18	0.83	0.61	0.57	1.82	3.67	0.72	0 07	0.01	0.00	0.00	32.92
13 AT_3	29.35	1.50	1.55	0.24	1 01	0.73	0.70	2.12	0.33	0.17	0.05	0.01	0.00	0.00	37.75
synrift	28.80	1.34	1.34	0.17	0.89	0.71	0.64	1 87	0 04	0.00	0.00	0.00	0.00	0.00	35.81
Sum Accumulated in Reservoir	80.74	4.19	4.40	0.64	2 99	2.26	2.11	6.55	8.93	4.67	1.58	0.40	0.08	0.03	119.56
Migration Losses	5.11	2.10	2.46	0.40	1 71	1.50	0.94	4.45	28.98	21.52	10.34	4.36	1.66	0.86	86.38

Sec. Cracking Losses	-336.71	0.09	0.00	0.01	-0.01	-0.37	-0.22	0.25	216.26	144.13	105.56	62.28	29.97	18.05	139.21
Inner Tertiary	1.52	0.19	0.20	0.03	0.14	0.10	0.09	0.32	1.57	1.11	0.54	0.23	0.09	0.05	6.17
22At1	4.39	1.71	1.79	0.28	1.29	0.88	0.73	2.97	18.35	14.30	7.22	3.20	1.27	0.65	58.96
18At_1	92.00	18.69	19.61	2.99	13.34	9.50	8.32	31.69	186.77	138.27	63.27	23.77	7.74	3.38	619.34
18At_2	0.65	0.28	0.30	0.05	0.20	0.18	0.11	0.51	3.37	2.54	1.26	0.55	0.23	0.13	10.36
17At1	0.16	0.07	0.08	0.01	0.06	0.05	0.03	0.15	0.97	0.72	0.35	0.15	0.06	0.04	2.91
16D1	120.57	17.55	18.75	2.71	12.25	9.14	8.37	26.97	167.89	130.50	58.46	18.00	3.35	0.45	584.45
16At1_1	1.64	0.12	0.13	0.02	0.08	0.05	0.06	0.18	0.53	0.21	0.04	0.01	0.00	0.00	3.06
16At1_2	3.08	0.52	0.54	0.08	0.37	0.27	0.22	0.86	4.75	3.39	1.58	0.66	0.26	0.13	16.72
16At1_3	10.48	2.33	2.42	0.36	1.62	1.22	1.11	3.54	22.56	18.47	9.48	4.02	1.40	0.59	79.56
15 At	8.61	1.94	2.02	0.30	1.36	1.03	0.94	2.96	18.91	15.60	8.16	3.56	1.30	0.59	67.27
14At1 01_1	12.27	2.74	2.58	0.37	1.58	1.18	1.05	3.02	18.20	14.54	7.68	3.39	1.25	0.58	70.41
Sum Outflow Ton	245.38	46.15	47.93	7.21	32.19	23.60	21.01	73.19	443.87	339.59	158.03	57.54	16.94	6.59	1529.21
16At1_3	0.60	0.13	0.19	0.03	0.16	0.13	0.10	0.45	3.05	2.40	0.91	0.21	0.03	0.01	8.41
SR C_01	0.12	0.05	0.06	0.01	0.04	0.04	0.02	0.10	0.67	0.50	0.25	0.12	0.04	0.02	2.02
13 AT_1	17.19	5.37	5.40	0.70	3.61	2.92	2.57	7.69	50.94	44.26	24.91	12.12	5.25	3.18	186.11
SR Aptian	0.03	0.01	0.01	0.00	0.01	0.00	0.00	0.01	0.09	0.06	0.03	0.01	0.00	0.00	0.27
13 AT_3	332.83	31.94	33.07	5.09	21.63	15.89	15.12	45.33	297.69	240.84	63.48	26.81	10.60	5.77	956.05
6At1	17.34	5.88	5.88	0.73	3.91	3.47	2.87	8.28	56.46	49.88	28.60	14.30	6.51	4.29	208.39
SR H	0.28	0.11	0.11	0.01	0.07	0.05	0.05	0.15	0.98	0.86	0.49	0.24	0.10	0.06	3.57
Synrift	0.43	0.17	0.17	0.02	0.12	0.09	0.08	0.24	1.65	1.48	0.87	0.44	0.20	0.12	6.09
Sum Outflow Side	368.82	43.65	44.84	6.60	29.55	22.59	20.85	67.25	321.52	240.28	119.53	54.25	22.75	13.46	1370.93
Sum HC Losses	282.60	91.99	95.27	14.27	63.43	47.32	42.58	#####	910.63	745.53	393.46	178.43	71.33	38.95	3115.73